1-1-2017

Ln(ii)-Containing Cryptates: Synthesis And Properties

Akhila Nuwan Wijerathne Kuda-Wedagedara
Wayne State University,

LN^{II}-CONTAINING CRYPTATES: SYNTHESIS AND PROPERTIES

by

AKHILA N. W. KUDA-WEDAGEDARA

DISSERTATION

Submitted to the Graduate School

of Wayne State University,

Detroit, Michigan

in partial fulfillment of the requirements

for the degree of

DOCTOR OF PHILOSOPHY

2016

MAJOR: CHEMISTRY

Approved by:

_____

Advisor Date

_____

_____

_____

DEDICATION

To my beloved parents, wife, and son

ACKNOWLEDGEMENTS

First I would like to thank my advisor, Dr. Matthew J. Allen for all the support and advice given to me throughout last five years. I am thankful to my committee members, Dr. Stanislav Groysman, Dr. Zhongwu Guo, and Dr. Meser Ali for their valuable time and suggestions. I take this opportunity to thank past and present Allen lab members for all the fun, chemistry discussions, and hard questions. I also thank all the present and past chemistry graduate students especially Brock and Verani lab members. I specially thank Dr. Federico Rabuffetti for valuable discussions on lanthanide luminescence and helping me with luminescence measurements and Dr. Brock for understanding our difficult times and her guidance. I also thank Melissa, Debbie, Nestor, science store staff, business office staff for helping me figure out lot of other issues that I encountered in the chemistry department and all my Sri Lankan friends and friends in Wayne State for being around me whenever needed.

My special thank goes to my mum and two brothers Loku and Tutu for being there with me in every step of my life to share success and failures. There are no enough words in this world to thank my mum for her valuable life lessons and the courage she showed at the most difficult time of our lives.

Finally I would like to thank the three most amazing people in my life, my wife Asha for her love, my son Devnija, and son on the way for giving me a purpose to live and reminding me that there is a beautiful place called home.

TABLE OF CONTENTS

LIST OF TABLES

LIST OF FIGURES

LIST OF SCHEMES

CHAPTER 1: PROPERTIES OF Ln^{II}-CONTAINING COMPLEXES

Parts of this chapter was adapted with permission from Kuda-Wedagedara, A. N. W.; Allen, M. J. *Analyst* **2014,** *139*, 4401–4410. Reproduced by permission of the Royal Society of Chemistry.

Introduction

This chapter describes the redox, photochemical, and magnetic properties of Ln^{II}-containing complexes and the influence of coordination environment on these properties. These properties change with the changes in coordination environment, making these ions desirable in potential applications including optoelectronics, sensors, contrast agents in MRI, and luminescence imaging.[1-4] Many reports discuss the influence of coordination environment on the chemical properties of Ln^{II}-containing complexes, but the influence of a wide range of coordination environments on the redox, photochemical, and magnetic properties of Ln^{II}-containing complexes has not been fully investigated. Especially in the solution-phase, reports of changes in redox, photochemical, and magnetic properties with respect to a wide range of coordination environments are rare.[5-10] Furthermore, the complexes of Ln^{II} ions are unstable under ambient conditions and when dissolved in commonly used solvents due to their highly negative reduction potentials (**Figure 1.1**), making research in this area challenging.[5] The rest of this chapter and this thesis describes the three most stable divalent lanthanide ions (Sm^{II}, Eu^{II}, and Yb^{II}). This chapter also provides context to the subsequent chapters.

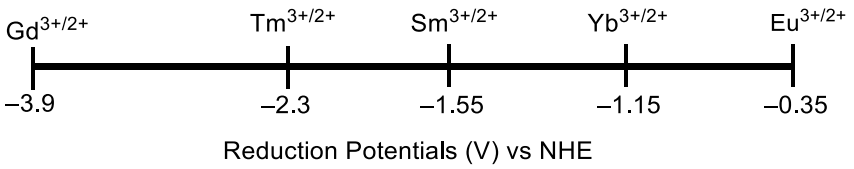

Figure 1.1. Reduction potentials of several Ln ions vs normal hydrogen electrode (NHE)[5]

1.1 Ln^{II}-Containing Reducing Agents

Although divalent lanthanides are unstable under ambient conditions, their unique redox and photochemical properties have been a focus in many research areas including reducing

agents, catalysis, sensors, and contrast agents in imaging.[8-11] All lanthanides except Pm have been reported in their (+2) state,[5] and the most stable ones are Sm^{II}, Eu^{II}, and Yb^{II}. Of the three most stable Ln^{II} ions, Sm^{II} is the most potent reducing agent, making it a useful reagent in the reduction of functional groups and in reductive coupling reactions.[10,12-16] One of the first reported Sm^{II}-based reducing agent is known as the Kagan reagent (SmI_2) that was reported by Kagan and co-workers in 1977. The Kagan reagent is known to reduce aromatic and aliphatic aldehydes and ketones and alkyl and aryl iodides (**Scheme 1.1**). Inanaga and co-workers later developed Sm^{II}-based reagent with the addition of hexamethylphosphoramide (HMPA) to make SmI_2 more powerful reducing agent than Kagan's reagent.[13,15,16] Because of the strong coordinating nature of HMPA, the reduction potential becomes more negative for SmI_2-HMPA (–1.75 V vs SCE) compared to SmI_2 (–1.5 V vs NHE).[11] SmI_2-HMPA has been reported to reduce wide range of functional groups including alkyl chlorides (in addition to the bromides and iodides), esters, and carboxylic acids (**Scheme 1.1**) that are not reducible with SmI_2.[13,15,16] Due to the toxic nature (known carcinogen) of HMPA,[11] alternative Sm^{II}-based reagents became available.[11] Kudo and co-workers found that Sm^{II} in the presence of alkali base in THF was powerful enough to reduce esters (**Scheme 1.1**).[15] The chemistry of Sm^{II}-based reductions was further developed largely by the research groups of Proctor and Flowers.[17-20] Other examples of alternative reagents developed in the area of Sm^{II}-based reductions were SmI_2-Et_3N-H_2O and light stimulated SmI_2.[21,22] SmI_2-Et_3N-H_2O was first reported by Hilmersson and co-workers to reduce ketones, imines, α, β unsaturated esters to corresponding alcohols (**Scheme 1.1**) with excellent selectivity over other Sm^{II}-based reagents.[21] The SmI_2-Et_3N-H_2O system was also reported to reduce esters, alkyl and aryl halides, and nitriles (**Scheme 1.1**).[14,22] Light stimulated SmI_2 reductions (**Scheme 1.1**) were reported by Hoz and co-workers and Hirao and co-workers.[23,24] Hoz and co-workers used 600 nm light (2.02 eV) to excite SmI_2 that is expected to be a higher boost in reduction

potential than the reduction potential increase attained by adding HMPA to SmI_2 (0.72 V more negative reduction potential than SmI_2). They also reported that adding methanol helped facilitate the protonation of the short lived radical anion by transferring protons unimolecularly.[23] A radical anion is formed when the inner sphere electron transferred from Sm^{II} to organic substrate. Hirao and co-workers reported photo-induced reduction of alkyl and aryl halides using SmI_2.[24] When they irradiated a reaction mixture with light at wavelengths shorter than 420 nm or longer than 700 nm, no reaction products were observed, but irradiation between 560 and 800 nm lead to the reduction of alky halides to alkanes.[24]

Scheme 1.1 Ln^{II}-based reducing agents used in functional group transformations (a)–(g)

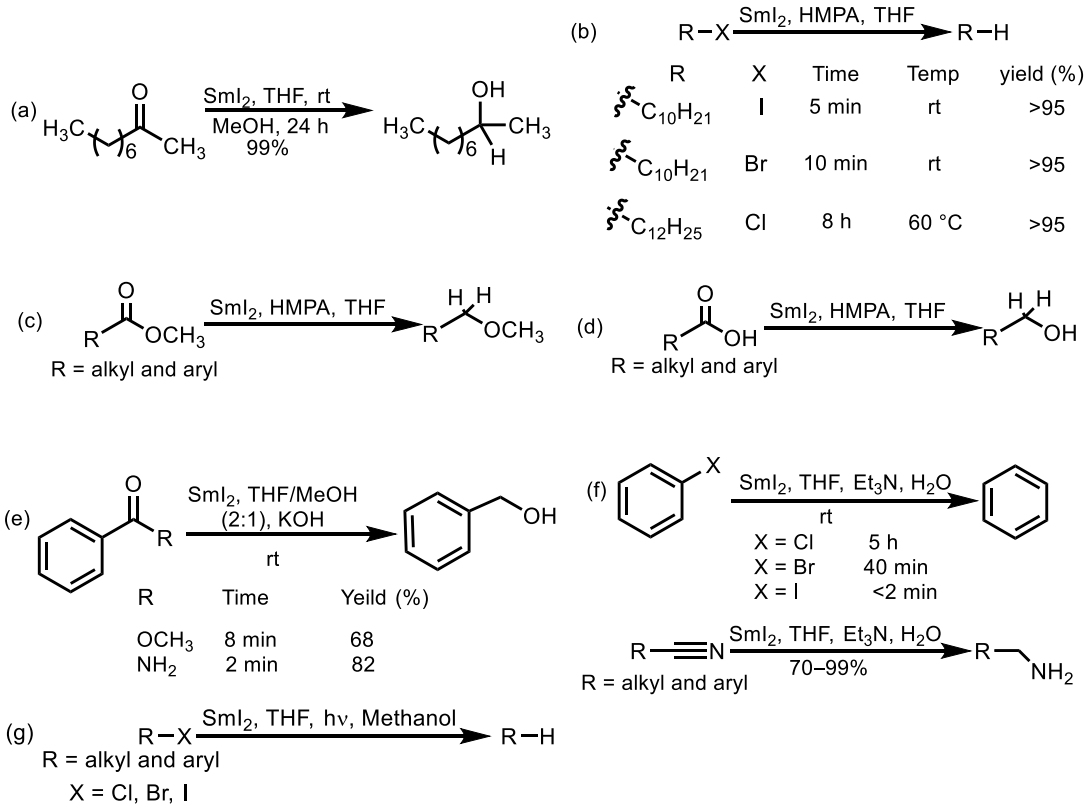

One of the limitations of Sm^{II}-based reagents is that they are stoichiometric reducing agents making them unfavorable in large scale synthetic applications. To address this limitation, attempts to make Sm^{II}-based reagents catalytic were reported.[25-28] The main strategies for

regenerating Sm^{II} ions include electrochemical and chemical methods.[25-28] In the electrochemical methods, Sm^0 metal electrode was used as the working electrode that is dipped in a solution containing a substrate. At a high enough oxidation potential Sm^{II} is produced and the reaction between the substrate and Sm^{II} salt is taken place.[25-28] Mellah and co-workers first reported the use of the Sm^0 metal electrode to generate Sm^{II}.[25,26] These redox reactions with the sacrificial electrode allowed them to use sub-stoichiometric amounts of Sm^{II} (10 mol %), ($E^{\circ}_{Mg(2+)/Mg}$ = –2.37 V and $E°_{Sm(2+)/Sm}$ = –2.41 V).[25] The chemical methods involve the use of a sacrificial reductant that reduces Sm^{III} that is a product of the reaction. The use of Mg^0, Zn^0(Hg), and mischmetal as sacrificial reductants have been reported.[27,28] Endo and co-workers reported the pinnacle coupling with Sm^{II} ions (0.1 equiv) in the presence of excess Mg^0 and chlorotrimethylsilane (0.5 equiv),[27] and Lucci and co-workers also reported SmI_2-Mg^0 system for Reformatsky-type reactions.[29] In these coupling reactions, Mg^0 serves as a sacrificial reductant to generate Sm^{II} ions from Sm^{III} formed during the reaction. Corey and co-workers used Zn^0(Hg) as a sacrificial reductant for regenerating the Sm^{II} ions (10 mol %) from Sm^{III} formed during the conversion reactions of ketones to γ-lactones, the deoxygenation of oxiranes to olefins, and radical π-cyclizations.[28] Much of the research is still underway in this area to improve the catalytic efficiencies regarding Sm^{II}-based reductions.[30] The other two ions Eu^{II} and Yb^{II} also have been reported as catalysts for polymerization reactions that go through reduction pathways.[31] Although Yb^{II} and Eu^{II} are not considered desirable in reduction chemistry because of their lower reduction potentials than Sm^{II}, several reports of polymerization reactions that are catalyzed by Yb^{II}- and Eu^{II}-containing complexes are available.[31-33]

Huang and co-workers reported Eu^{II}-containing complex (**Figure 1.2**) that catalyzes the methyl methacrylate (MMA) polymerization through a migration insertion mechanism.[31] The mechanism involves homolysis of a Eu–N bond leading to the elimination of $(Me_3Si)_2N$ radical

to initiate the reaction. Apart from the redox activity of Ln^{II} ions, the luminescence properties of these ions are also a major research area for Ln^{II}-containing compounds.

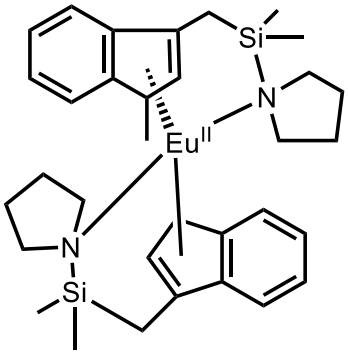

Figure 1.2. The structure of Eu^{II}-containing MMA polymerization catalyst

1.2 Ln^{II}-Containing Luminescent Agents

Absorption and emission spectra of Ln^{II} ions, in contrast to Ln^{III} ions that display narrow absorptions and emissions and large stokes shifts due to Lapporte forbidden f–f transitions, display broad and intense absorptions in the UV to visible range (**Figure 1.3**)[34] and emissions in the visible to near IR regions in the electromagnetic spectrum because of the Lapporte allowed f–d transitions.[34] Materials containing Ln^{II} ions have been investigated in optoelectronics and lighting materials.[35] In addition to the intense absorption and emission bands of Ln^{II} ions, the wavelength at which Ln^{II} ions emit can also be tuned by the coordinating environment leading to emissions at different wavelengths in the visible to near IR region making them desirable for optoelectronic and optical imaging applications. Not only do Ln^{II} ions emit at different wavelengths, but mixing different Ln^{II} ions can result in different colored emissions including white light.[36] White-light-emitting materials have a huge demand in applications of light emitting diodes (LED) because of the energy saving ability of LEDs relative to the commonly used fluorescent lamps.

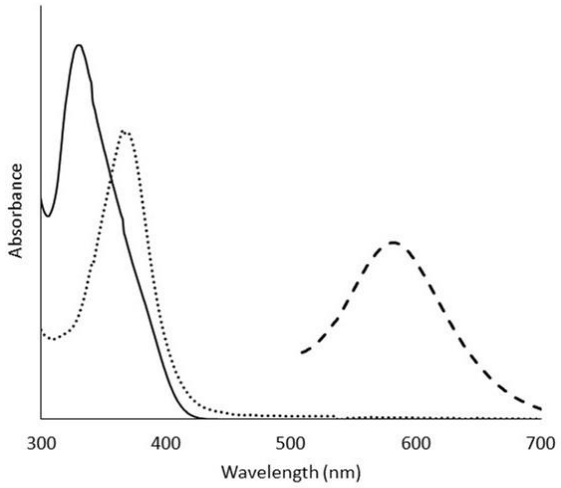

Figure 1.3. Absorption spectra measured (only the lowest energy transitions are displayed) for EuI_2 (——), YbI_2 (• •), and SmI_2 (— —) in dry methanol under Ar.

Ryback and co-workers reported a series of yellow-emitting Eu^{II}-containing metal organic frameworks (MOFs) synthesized with different ratios of BaH_2, Eu^{II}, and imidazole to yield a series of $Ba_{1-x}Eu_xIm_2$ (**Figure 1.3**) that emit in the yellow region of the visible spectrum with quantum yields of 28–32%.[36] These yellow-light-emitting materials are important because when mixed with blue-light-emitting materials, white light can be produced. Blue emission is relatively common with Eu^{II} ions; whereas green, yellow, and red emissions are quite rare.[36] Several reports of green- and red-emitting Eu^{II}-containing materials are also available.[37] Kunkel and co-workers reported a series of red-emitting Eu^{II}-containing materials synthesized with CaH_2, SrH_2, and BaH_2 (**Figure 1.4**).[38] These materials displayed broad emissions from red to near IR region (600–1100 nm) of the electromagnetic spectrum.

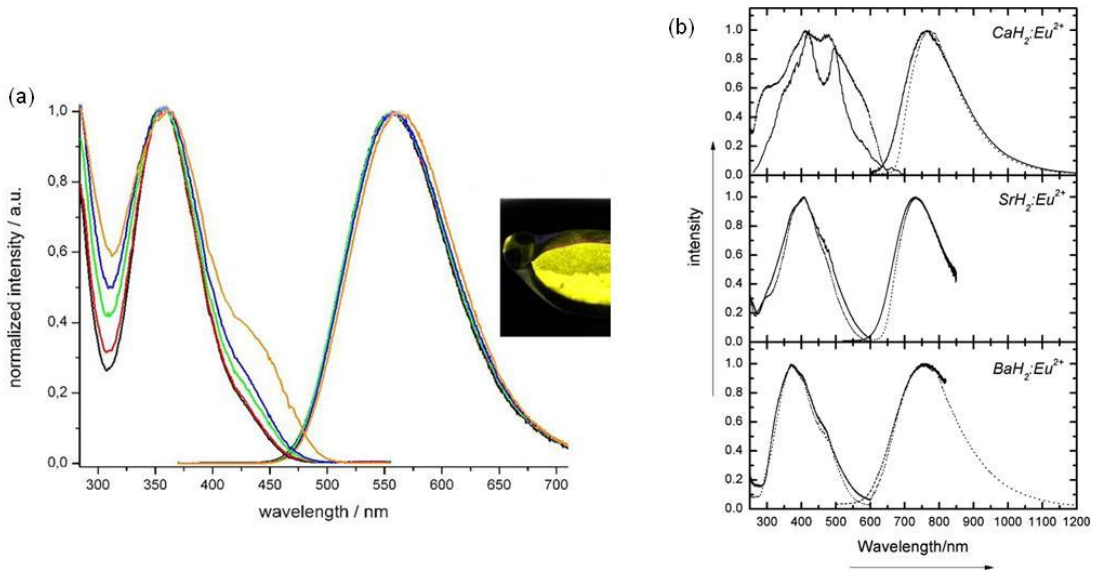

Figure 1.4. Excitation and emission spectra of Eu^{II}-containing materials (a) $^3{}_\infty[Ba_{1-x}Eu_xIm_2]$ where x = 0.01 (—), x = 0.02 (—), x = 0.05 (—), x = 0.1 (—), and x = 0.2 (—) and the image displays the yellow luminescence of this material in an NMR tube upon excitation with blue light [36] Reprinted with permission from (Rybak, J.-C.; Hailmann, M.; Matthes, P. R.; Zurawski, A.; Nitsch, J.; Steffen, A.; Heck, J. G.; Feldmann, C.; Götzendörfer, S.; Meinhardt, J.; Sextl, G.; Kohlmann, H.; Sedlmaier, S. J.; Schnick, W.; Müller-Buschbaum, K. J. Am. Chem. Soc. **2013,** 135, 6896). Copyright (2015*) American Chemical Society* and (b) MH_2: Eu^{2+} where M = Ca, Sr, and Ba.[38] Reprinted with permission from (Kunkel, N; Kohlmann, H.; Sayede, A.; Springborg, M.; *Inorg. Chem.* **2011,** *50,* 5873). Copyright (2015*) American Chemical Society.*

The luminescence of Eu^{II} in the solid state is heavily investigated area, but reports on Yb^{II} luminescence also available.[39] Hintzen and co-workers reported a Yb^{II}-containing $CaAlSiN_3$ material that emits in the red region (λ_{em} = 529 nm) upon excitation in the range between 280 and 580 nm. The large red shift observed with the emission spectrum of Yb^{II} is due to the strong field ligand environment that consist of nitrogen donors compared to the Yb^{II} in Ca-α-SiAlON and $SrSi_2O_2N_2$ that are green- and yellow-emitting, respectively.[40] These oxonitrides shift the Yb^{II} emission to a lesser extent than in the case of $CaAlSiN_3$, because oxonitrides impose lower ligand field strength than nitrides.

Solution-phase luminescence applications with Ln^{II} ions are limited due to reactivity toward water and also the ability of solvent molecules to quench the luminescence of Ln^{II}-containing complexes.[41,42] **Table 1.1** compiles several examples (both solid- and solution-phase)

of reported Ln^{II}-containing luminescent materials with their emission ranges and quantum yields. Although the shift in emission of Eu^{II} is reported in the solid phase, in solution phase, particularly in aqueous solution, shifts to lower energies have not been reported. The maximum quantum yield reported for aqueous divalent lanthanides is 1% for a blue emitting Eu^{II}-containing complex that was reported by Sabatini and co-workers with the cryptand **1.7** (**Figure 1.5**).[42] Adachi and co-workers reported a series of Eu^{II}-containing complexes synthesized with crown ethers and cryptands **1.1**–**1.7** (**Figure 1.5**) where they observed emission in the blue region of the visible spectrum upon excitation with the UV light, and they reported the solution-phase emissions and quantum yields for these complexes (**Table 1.1**).[41] Flowers and co-workers reported luminescence of Sm^{II}-containing complexes synthesized with crown ethers **1.1** and **1.2** in acetonitrile (**Figure 1.5**).[43] They observed enhanced luminescence in the red region of the visible spectrum for **1.1**-Sm^{II} and **1.2**-Sm^{II} compared to SmI_2 (**Table 1.1**).[43] The main reason for the low quantum yields measured in solution is quenching by directly coordinated solvent molecules.[43] These factors limit the potential uses of Ln^{II} luminescence in aqueous based applications including contrast agents for optical imaging where emissions at longer wavelengths are favored (λ >600 nm).

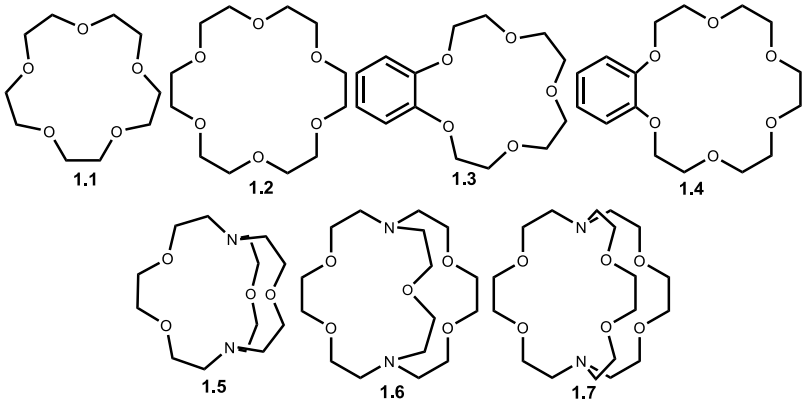

Figure 1.5. Several crown ethers and cryptands used to synthesize luminescent Ln^{II}-containing complexes in solution-phase

Table 1.1. Examples of Ln^{II}-containing luminescent compounds measured at ambient temperature

Compound	Emission Range (nm)	Quantum Yield (%)	Ref.
$^3{}_\infty[Ba_{1-x}Eu_xIm_2]$ (x = 0.01, 0.02,0.05, 0.1, 0.2)	450–750	28–32[a]	36
MH_2:Eu^{II}	600–1100	–	39
Yb^{II}-$CaAlSiN_3$	550–750	–	40
Yb^{II}-Ca-α-SiAlON	400–600	–	40
Yb^{II}-$SrSi_2O_2N_2$	450–650	–	40
1.7-Eu^{II}	450–650	1[b]	42
1.1-Eu^{II}	400–500	28[c]	41
1.2-Eu^{II}	400–500	9.4[c]	41
1.3-Eu^{II}	400–500	1.5[c]	41
1.4-Eu^{II}	400–500	0.2[c]	41
1.5-Eu^{II}	400–500	0.05[c]	41
1.6-Eu^{II}	400–500	1.4[c]	41
1.7-Eu^{II}	400–500	9.3[c]	41
SmI_2	600–900	0.0	43
1.1-Sm^{II}	450–750	0.3[d]	43
1.2-Sm^{II}	550–750	0.0004[d]	43

[a] in solid-phase, [b] in water, [c] in methanol, [d] in acetonitrile

The shifts observed in emission wavelengths of Ln^{II} ions in different coordinating environments can be explained with a schematic energy level diagram (**Figure 1.6**), where excited state energies of the Ln^{II}-containing complexes are compared to the solvated Ln^{II} ion. The red shift observed in the cases of Eu^{II} and Yb^{II} in the solid-phase is due to the strong field ligand environments compared to the Ln^{II} salts and solvated Ln^{II} ions. In the above examples,

Ln^{II} salts are either chlorides or iodides and the solvents are water, methanol, or acetonitrile. These halide anions and the solvents can be considered as either weak or intermediate field ligands;[44] therefore, the splitting energy ($\Delta E_a°$) of the $4f^{n-1}5d^1$ excited level is expected to be lower compared to a strong field ligand ($\Delta E_c°$). Because of the increase in splitting energy with strong field ligands, the energy gap between the ground state and the lowest excited state becomes smaller (ΔE_c) compared to the halide salts or the solvated ions. This decrease in energy results in a redshift in the emission spectrum. In the same manner, the complexation of Ln^{II} with a weaker field ligand compared to the halide salts or the solvated ions, the splitting energy becomes smaller ($\Delta E_b°$) leading to an increase in the energy gap between ground and lowest excited state (ΔE_b). This increase in the energy gap leads to a blue shift in the emission wavelength.

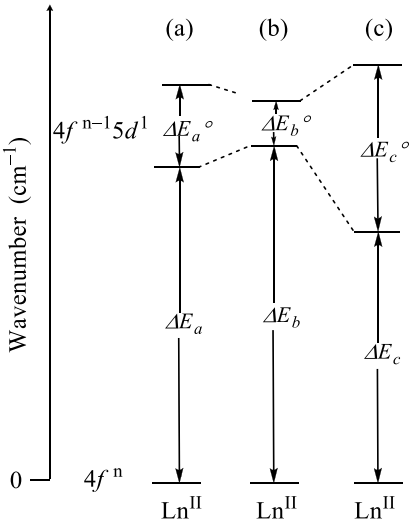

Figure 1.6. Schematic energy level diagram for a Ln^{II} ion in different coordinating environments (a) Ln^{II} ion in the presence of an intermediate ligand field environment, (b) Ln^{II} ion in the presence of an weak ligand field environment, and (c) Ln^{II} ion in the presence of a strong ligand field environment

Ln^{II}-containing compounds are not only displaying unique luminescence properties, but the magnetic properties of Ln^{II}-containing compounds include properties relevant to MRI contrast agents.

1.3 Magnetic Properties of Divalent Lanthanides

Although the magnetic properties of Ln^{II} ions are not as thoroughly investigated as compared to Ln^{III} ions, there are reports that discuss magnetic properties and magnetic interactions of Ln^{II}-containing complexes.[45,46] This area is mostly dominated by the Ln^{II} ions with high magnetic moments including Dy^{II} and Tm^{II}, whereas Sm^{II} and Yb^{II} display only small magnetic moments.[45] Eu^{II} on other hand has 7 unpaired electrons and displays high magnetic moment (7.65 μ_B);[45] therefore, magnetically, the Eu^{II} ion is unique relative to Sm^{II} and Yb^{II} ions. Magnetic interactions between Eu^{II} ions in 2,2'-bipyrimidine coordination polymers were reported by Ephritikhine and co-workers.[46] They synthesized three Eu^{II}-containing 2,2'-bipyrimidine coordination polymers with **1.8**, **1.9**, and **1.10** (**Figure 1.7**). Polymer **1.8**-Eu^{II} displayed weak anti-ferromagnetic coupling, and polymers **1.9**-Eu^{II} and **1.10**-Eu^{II} displayed weak ferromagnetic coupling between Eu^{II} centers.[46]

Recently, Evans and co-workers reported the magnetic properties of the whole Ln^{II} series (except Pm^{II}).[45] These Ln^{II}-containing (Ln^{II} = La, Ce, Pr, Nd, Gd, Tb, Dy, Ho, Er, and Lu) complexes were synthesized with tetramethylsilylcyclopentanyl ligands that were previously reported to have ground state configurations of $4f^{n-1}5d^1$; therefore, Sm^{II}, Eu^{II}, and Tm^{II} ground state configurations of $4f^n$ were suggested under the same conditions.[5] The magnetic moments reported for Dy^{II} and Ho^{II} (11.35 and 11.41μ_B, respectively) are the highest values reported for single metal ions at room temperature. Magnetic properties related to potential MRI contrast agents of Eu^{II}-containing complexes are also an important area of study.

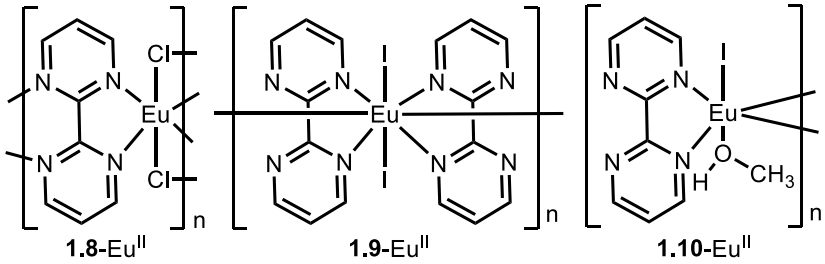

Figure 1.7. Structures of coordination polymers of Eu^{II}-containing 2,2'-bipyrimidine polymers

1.3.1 Eu^{II}-Containing Cryptates as T_1-Shortening Agents for Ultra-High Field Strengths

Magnetic resonance imaging (MRI) is a non-invasive technique that can map the relaxation rates of water protons in a magnetic field to generate images. Common clinical magnetic field strengths are 1.5 and 3 T, but higher field strength systems are being acquired each year. Over forty clinical and preclinical 7 T MRI scanners are available in the United States, and many higher field strength scanners (≥7 T) are used in preclinical research.[47-50]

Magnetic fields at or above 7 T are classified as ultra-high field strengths, and the use of 7 T magnets for clinical MRI has been reported,[51-55] and there is a strong urge to use ultra-high field MRI scanners because of the advantages that can be gained with ultra-high field strengths relative to lower field strengths, including high signal-to-noise ratios, high spatial resolution, short acquisition times, and the ability to use low sensitivity nuclei other than ^{1}H (including ^{19}F, ^{13}C, ^{23}Na, and ^{31}P).[48-50] These advantages are demonstrated by the increased amount of information that can be gained from MR images at ultra-high field strengths compared to lower field strengths (**Figure 1.8**).

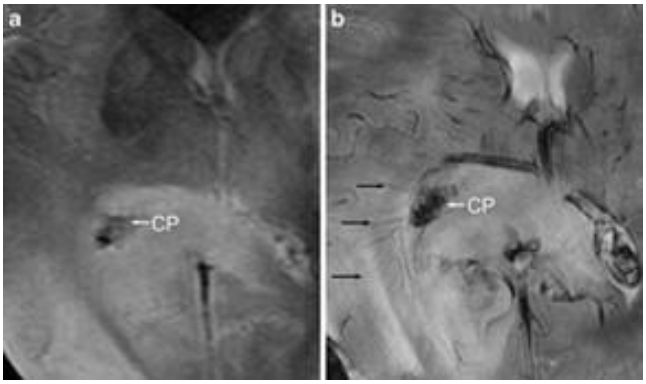

Figure 1.8. MR images of an axial slice of a human brain (a) at 1.5 T and (b) 7 T. The image acquired at 7 T enables visualization of blood vessels and choroid plexus (CP) that is not observable at 1.5 T.

Obtaining high quality MR images (high contrast-to-noise ratios) is critical in diagnosing diseases, but increases in magnetic field strength alone are not always sufficient to obtain images with high contrast-to-noise ratios. High contrast-to-noise ratios often can be achieved using paramagnetic metal complexes called contrast agents.[56-58] For example, Gd^{III}-containing complexes of ligands **1.11–1.16** shown in **Figure 1.9** are clinically approved contrast agents that are used to improve contrast-to-noise ratios in MR images. [59-61] These agents are useful enough that approximately half of clinical MRI scans use contrast agents.[62] Contrast agents influence both longitudinal ($1/T_1$) and transverse ($1/T_2$) relaxation rates, and clinically approved contrast agents can be categorized into two types of agents: agents with T_1/T_2 ratios close to one (T_1-shortening agents) and agents with T_1/T_2 ratios ≥ 6 (T_2-shortening agents).[63,64] Both types of contrast agents contain paramagnetic metal ions that increase the relaxation rates ($1/T_1$ and $1/T_2$) of the protons of the surrounding molecules, but current clinical contrast agents are less effective at ultra-high magnetic fields than at lower fields (**Table 1.2**, care should be taken to only compare values reported at the same temperature).[2,65,66]

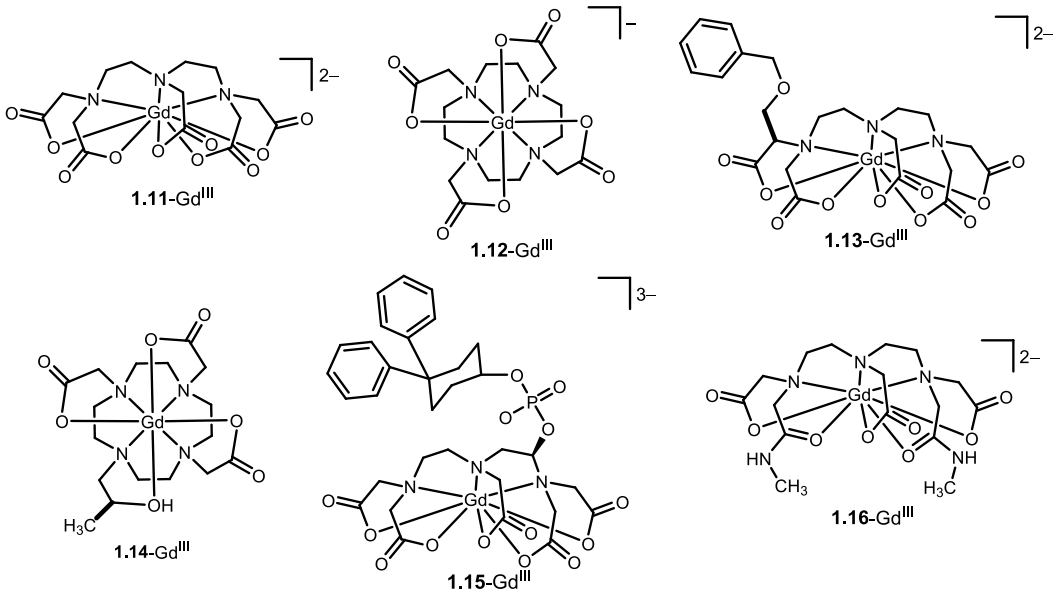

Figure 1.9. Structures of clinically available Gd^{III}-containing MRI contrast agents

Table 1.2. Relaxivities (mM^{-1} s^{-1}) per-Gd of T_1-shortening contrast agents at 37 ºC and 1.5, 3, and 7 T in blood.[67,68]

Complex	1.5 T	3.0 T	7.0 T
1.11-Gd^{III}	4.3	3.6	3.4
1.12-Gd^{III}	4.2	3.6	3.4
1.13-Gd^{III}	6.7	5.8	4.8
1.14-Gd^{III}	4.4	3.5	3.3
1.15-Gd^{III}	19	11.3	5.4
1.16-Gd^{III}	4.6	3.9	3.7

Because of the decrease in relaxivity with increasing field strength, a great deal of research has focused on modifying Gd^{III}-based agents to increase relaxivity at ultra-high field strengths. Additionally, other types of contrast agents have been studied to meet the need of efficient contrast agents at ultra-high fields. These other types of contrast agents include (1) modified Gd^{III}-based agents; (2) Eu^{II}-containing cryptates as T_1-shortening agents; (3) ^{19}F-MRI agents; (4) chemical exchange saturation transfer (CEST) agents; and (5) nanoparticle-based

agents. One of the focuses of the research in this thesis was to study Eu^{II}-containing complexes as potential T_1-shortening contrast agents at ultra-high field strengths.

Eu^{II}-containing cryptates have been explored as an alternate to Gd^{III}-containing contrast agents. Eu^{II} is isoelectronic with Gd^{III}, and the molecular parameters that influence the relaxivity of Gd^{III} influence Eu^{II} in similar fashion.[69] However, the larger radius (117 pm for Eu^{II} vs 93.8 pm for Gd^{III})[70] and lower charge of Eu^{II} allow the ion to have faster water-exchange rates than Gd^{III}.[71] Further, Eu^{II}-containing cryptates have two coordinated water molecules because Eu^{II} is large enough to have a coordination number of ten.[71]

Allen and co-workers reported a series of Eu^{II}-containing cryptates of **1.17**, **1.18**, and **1.7** (**Figure 1.10**) that are more efficient contrast agents than complex **1.12**-Gd^{III} (3.7 mM^{-1} s^{-1} at 7 T and 19 °C) at ultra-high field strengths (**Table 1.2**).[69] The higher relaxivities of Eu^{II}-containing cryptates relative to **1.12**-Gd^{III} at ultra-high fields are due to the ability to accommodate two water molecules in the inner sphere, the increase in water-exchange rates, and changes in rotational correlation rates compared to **1.12**-Gd^{III}.[8,69] The differences in relaxivities among different cryptates arise mainly from the changes in the rotational correlation rates that are proportional to molecular weight differences.[69] Eu^{II}-containing cryptates that display higher relaxivities than Gd^{III}-based contrast agents at ultra-high field strengths are potential alternatives to Gd^{III}-based contrast agents in T_1-weighted imaging. One of the current limitations of Eu^{II}-containing complexes is their tendency to oxidize to Eu^{III} in the presence of air. While some work has been done to overcome this effect,[8,72] further investigations are required to understand the in vivo outcomes of the oxidized products.

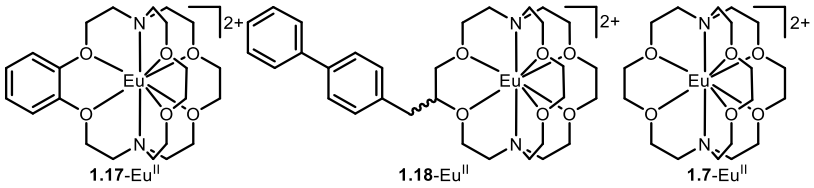

Figure 1.10. Eu^{II}-containing cryptates of **1.17**, **1.18**, and **1.7** (coordinated water molecules and counter ions are not shown for clarity).

Research Design

The redox, luminescence, and magnetic properties of Ln^{II}-containing compounds have displayed great promise in the fields of functional group reductions, catalysis, optoelectronics, optical imaging, and magnetic resonance imaging. These properties of Ln^{II}-containing compounds arise from the unique nature of the electronic properties of the Ln^{II} ions. These electronic properties including electron configurations (ground and excited state), spin-orbit coupling, and orbital overlap in metal-ligand bonding displayed by Ln^{II}-containing complexes.[79] These unique properties led many researchers to question the simple ionic model that is used to explain the chemical bonding and spectroscopic properties of Ln^{II}-containing complexes. The ionic model describes the 4f electrons as completely shielded from the environment and the interactions of these electrons in the ground state with the coordinating ligands are minimal. Evans and co-workers recently reported electron configuration of Ln^{II}-containing complex synthesized with cyclopentadienyl-type ligands, but this phenomena has not been reported with other types of ligands. For example, Sr^{II} (125 pm) and Eu^{II} (125 pm) although similar in charge and size display vastly different chemical properties such as spectroscopic properties, coordination geometries with ligands, response in chemical properties with changes in ligands, and thermodynamic stabilities.

To uncover chemistry behind the complexes of Ln^{II} ions, and also to expand the current knowledge on the redox, photochemical, and electronic properties of Ln^{II}-containing complexes, this thesis describes the synthesis of a series of ligands with different structural variations

including different coordinating atoms (strong Lewis bases and weak Lewis bases) and different substitutions on side chains (aliphatic, aromatic, and substituted aromatic groups) that enable an understanding how the different ligand environments influence the properties of Ln^{II} ions including photochemical, redox, and electronic properties.

In Chapter 2, a study of the structural and photochemical properties of a bright yellow emitting Eu^{II}-containing cryptate are described. Solid- and solution-phase characterizations are described to probe the coordination environment of Eu^{II}. Absorption and emission spectra and quantum yield determinations describe the photochemical properties of this new complex. This study provides the foundation for tunability of luminescence properties of Eu^{II} in aqueous media suggesting potential applications in optical imaging.

Chapter 3 described a study of the influence of the cryptand-type ligands on the Eu^{II} ion with X-ray crystal structures, NMR spectroscopy, and elemental analysis. Photochemical properties were studied with UV–vis absorption and fluorescence spectroscopy and the redox properties were evaluated using cyclic voltametry. The results of this chapter and Chapter 2 could be used to understand the influence of coordination environment on the physicochemical properties of Eu^{II} ion that is useful in MRI contrast agents, luminescent materials, and chemical reductions.

Chapter 4 describes a series of cryptates synthesized from the same series of cryptands used in Chapter 3 with YbI_2 to study trends in photochemical and redox properties and electronic structures. Structural characterizations were done with X-ray crystal structures, NMR spectroscopy, and elemental analysis. Photochemical properties were studied with UV–vis absorption and fluorescence spectroscopy and the redox properties were evaluated using cyclic voltammetry. Results of these experiments aid in the understanding the nature and the influence of coordination environment on the properties of metal complexes. The study described in this

chapter together with studies described in Chapters 2 and 3 enable to understand the influence of metal-ligand interactions in Ln^{II}-containing cryptates. This understanding could be used to optimize properties of Ln^{II}-containing reducing agents, luminescent agents, magnetic materials, and catalysts.

Chapter 5 summarized the major findings of the research projects described in the Chapters 2, 3, and 4 with set of conclusions. This chapter also described several directions to which the results of these research projects can be used and study further to gain in depth understanding of the chemical properties of these metal-ligand systems.

For the rest of this thesis, numbers to indicate ligands and number-metal ions for metal complexes will be used.

CHAPTER 2: AQUEOUS EU^{II}-CONTAINING COMPLEX WITH BRIGHT YELLOW LUMINESCENCE

Parts of this chapter have been adapted with permission from Kuda-Wedagedara, A. N. W.; Wang, C.; Martin, P. D.; Allen, M. J. *J. Am. Chem. Soc.* **2015,** *137,* 4960–4963. Reproduced by permission of the American Chemical Society.

2.1 Introduction

Luminescent materials with high quantum yields are important for imaging applications and optoelectronic materials,[73-79] and the luminescence properties of Eu^{II}-containing materials make them desirable choices for use in these applications.[36,80-82] Although the emission of Eu^{II} in the solid state is relatively strong (quantum yields of 25–92%),[36,82-85] in aqueous solutions, weak emissions (quantum yields of ~0.1%) are observed due to quenching of the excited state of Eu^{II} by OH oscillators.[42,86,87] This quenching limits the usefulness of Eu^{II}-based luminescence in aqueous systems.[87] Additionally, materials that emit yellow light are desirable in the lighting and imaging fields.[36] Reported Eu^{II}-containing complexes in aqueous media absorb in the UV and emit in the blue region (380–530 nm) of the electromagnetic spectrum.[87] These complexes mainly include crown ethers and cryptand-based ligands, and the quantum yields of these complexes are low (≤0.1%).[87] This chapter describes a Eu^{II}-containing cryptate synthesized with the cryptand **2.1** and $EuCl_2$, that displays bright yellow emission (500–700 nm) in aqueous solution (**Figure 2.1**). Chloride salt of Eu^{II} was used due to solubility in aqueous media and being able to compare to other Eu^{II}-containing complexes reported in aqueous media.[87]

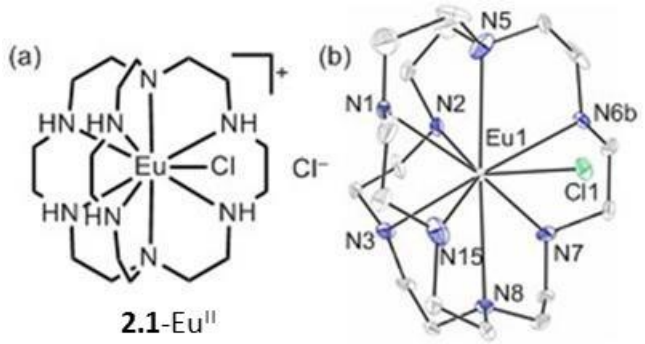

2.1-Eu^{II}

Figure 2.1. (a) Eu^{II}-containing aza-222 cryptate **2.1**-Eu^{II} and (b) the crystal structure of **2.1**-Eu^{II}. Thermal ellipsoids are drawn at 50% probability. Hydrogen atoms, the non-coordinated Cl^- counter ion, and a molecule of methanol are not shown in the structure for clarity. R-factor = 0.0543. Resolution = 0.54 Å.

2.2 Experimental Procedures

Commercially available chemicals were of reagent-grade purity or better and were used without further purification unless otherwise noted. Water was purified using a PURELAB Ultra Mk2 water purification system (ELGA). Azacryptand-1,4,7,10,13,16,21,24-octaazabicyclo[8.8.8]hexacosane (**2.1**) was prepared by following a published procedure.[88,89]

Samples of **2.1**-Eu^{II} were prepared in a wet (water allowed but no molecular oxygen) glovebox under an Ar atmosphere. Quantum yield standards (fluorescein and coumarin-153) were crystallized three times from ethanol, and their purity was checked using a high-performance liquid chromatography (HPLC) system (Shimadzu) equipped with an analytical pinnacle column (Restek International, Pinnacle DB Cyano, 5 μm, 250 mm × 4.6 mm). Analytical HPLC used a binary gradient method (pump A: water; pump B: acetonitrile; flow rate: 1 mL/min). Fluorescein eluted at 19.7 min using 0% B for 4 min, 0→25% B over 2 min, 25% B for 4 min, 25→50% B over 2 min, 50% B for 6 min, then 50→75% B over 2 min. Coumarin-153 eluted at 14.8 min using 0% B for 4 min, 0→75% B over 4 min, then 75% B for 8 min. Fluorescein and coumarin-153 were detected with a photodiode array detector by monitoring absorbance at 474 and 429 nm, respectively.

UV–vis absorbance was measured using a Shimadzu UVmini-1240 spectrophotometer. Emissions, decay rates, and integrated emissions were recorded using a HORIBA Jobin Yvon Fluoromax-4 spectrofluorometer. Variable-temperature ^{17}O-NMR measurements were performed using a Varian-500S (9.4 T) spectrometer for sample **2.1**-Eu^{II} and **2.1**-Sr^{II} (5.0 mM, 700 μL) at pH 12.0 in 0.5% ^{17}O-enriched water (Cambridge Isotope Laboratories, Inc.) at 15, 20, 30, 40, 50, 60, and 70 °C following a published procedure.[90] Job plots were obtained by measuring the integrated emission (λ_{ex} = 415 nm and λ_{em} = 580 nm) using a HORIBA Jobin Yvon Fluoromax-4 spectrofluorometer for different mole fractions (0.1–0.9) of Eu^{II} relative to **2.1**-Eu^{II} prepared by mixing $EuCl_2$ with **2.1** at ratios of 1:9, 2:8, 3:7, 4:6, 5:5, 6:4, 7:3, 8:2, and 9:1.

Emission intensity (λ_{ex} = 415 nm) vs pH studies were performed by preparing 5 samples of **2.1**-Eu^{II} (1.0 mM, 3.0 mL) at different pH values (8.0, 9.5, 10.0, 11.3, and 12.0) by adjusting the pH of solutions of **2.1**-Eu^{II} with KOH (0.05 M) or HCl (0.05 M). Emission spectra are acquired on a HORIBA Jobin Yvon Fluoromax-4 spectrofluorometer.

Decay rates were calculated from decay curves measured at 580 nm emission (λ_{ex} = 415 nm) with excitation and emission slit widths of 3 nm, initial delay of 0.01 ms, maximum delay of 0.2 ms, and an increment of 0.0025 ms. Samples of **2.1**-Eu^{II} at pH 12.0 and 9.5 were prepared by dissolving **2.1**-Eu^{II} (8.8 mg) in water (2.0 mL) and adjusting the pH with aqueous solutions of KOH (0.05 M) or aqueous solutions of HCl (0.05 M). Samples of **2.1**-Eu^{II} for decay-rate analysis were prepared by withdrawing a 100 μL from the stock solutions and diluting to 3.0 mL with aqueous solutions of KOH (pH 12.0 and 9.5). The pH values were measured using Hanna checker portable pH meter at ambient temperature, and the solutions were transferred to air-tight quartz cuvettes under an Ar atmosphere.

Molar conductivity was calculated from three independently prepared solutions of **2.1**-Eu^{II} (1.0 mM, 15.0 mL) measured at pH 10.0 under an Ar atmosphere and ambient temperature

using an Omega CDH 280 portable conductivity meter that was calibrated with aqueous KCl (0.01 M, 1.413 mS/cm). Results are reported as mean ± standard error.

Elemental analysis (C, H, and N) determinations were performed by Midwest Microlab (Indianapolis). Cyclic voltametry was performed using a Pine Wavenow USB potentiostat in an electrochemical cell under an Ar atmosphere with a Ag/AgCl reference electrode, a glassy carbon working electrode, and a Pt wire auxiliary electrode. A solution (pH 9.7) of complex **2.1-**Eu^{II} (2.0 mM) and Et_4NClO_4 (0.1 M) in water (5.0 mL) was used for the analysis, and the potential was 0.14 V ± 0.05 V, which is the mean ± standard error of the measurements of three independently prepared samples. Inductively coupled plasma mass spectroscopy (ICP–MS) analyses were used to determine all solution concentrations and were performed with an Agilent 7700x inductively coupled plasma mass spectrometer at the Lumigen Instrument Center in the Department of Chemistry at Wayne State University. Standards of Eu were prepared by diluting commercially available standards (Eu_2O_3 in aqueous nitric acid, 5%, 1000 ppm, Alfa Aesar) with aqueous nitric acid (2%). High-resolution electrospray ionization mass spectrometry (HRESIMS) was performed using an electrospray time-of-flight high-resolution Waters Micromass LCT Premier XE mass spectrometer.

Eu^{II}-azacryptand-1,4,7,10,13,16,21,24-octaazabicyclo[8.8.8]hexacosane (2.1-Eu^{II}): To a solution of azacryptand-1,4,7,10,13,16,21,24-octaazabicyclo[8.8.8]hexacosane **2.1** (103 mg, 0.278 mmol) and $EuCl_2$ (51.7 mg, 0.232 mmol) in methanol (3.0 mL) was added water (200 µL), and the resulting solution was stirred for 2 h under an Ar atmosphere. After 2 h, the yellow-orange solution was filtered using a 0.2 micron filter (Millex-LG hydrophilic), and into the filtrate was diffused tetrahydrofuran vapor over 3 days until yellow-green needle-like crystals formed at the bottom of the vial. The crystals were washed with diethyl ether (3 × 2 mL) and ground with a mortar and pestle prior to drying under vacuum to obtain 89.0 mg (65%) of **2.1-**

Eu^{II} as a green powder (**Scheme 2.1)**. Anal. Calcd for $C_{18}H_{42}N_8EuCl_2 \cdot H_2O$: C, 35.36; H, 7.25; N, 18.33. Found: C, 35.13; H, 7.15; N, 17.99. All values are given as percentages. Crystals for X-ray analysis were removed prior to grinding.

Scheme 2.1. Synthesis of **2.1**-Eu^{II} and **2.1**-Sr^{II}

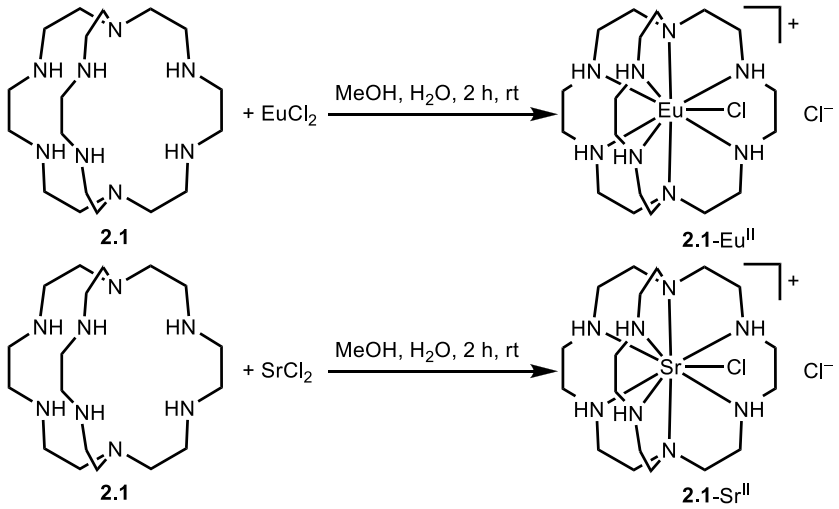

Sr^{II}-azacryptand-1,4,7,10,13,16,21,24-octaazabicyclo[8.8.8]hexacosane (2.1-Sr^{II}): To a solution of azacryptand **2.1** (52.0 mg, 0.140 mmol) and $SrCl_2 \cdot (H_2O)_6$ (37.4 mg, 0.140 mmol) in methanol (3.0 mL) was added water (200 µL), and the resulting solution was stirred for 2 h under an Ar atmosphere. After 2 h, the colorless solution was filtered using a 0.2 micron filter (Millex-LG hydrophilic), and the solvent was removed under reduced pressure to yield a white powder that was washed with diethyl ether (3 × 2 mL) and dried under vacuum to obtain 30.0 mg (47%) of **2.1**-**Sr^{II}** as a white powder (**Scheme 2.1**). HRESIMS (*m/z*): $[M + Cl]^+$ calcd for $C_{18}H_{42}N_8SrCl$, 493.2277; found 493.2289, Anal. Calcd for $C_{18}H_{42}N_8SrCl_2.H_2O$: C, 39.51; H, 8.11; N, 20.48. Found: C, 38.92; H, 7.78; N, 19.85. All values are given as percentages.

Calculation of Quantum Yield

Coumarin-153 was used as the quantum yield standard of which the relative quantum yield (0.58 ± 0.02) was measured against fluorescein (0.79) at λ_{ex} = 415 nm following a

published procedure,[91,92] using a HORIBA Jobin Yvon Fluoromax-4 spectrofluorometer with excitation and emission slit widths of 0.5 nm. After calibrating coumarin-153 against fluorescein, a series of concentrations of complex **2.1**-Eu^{II} (0.042, 0.085, 0.12, and 0.16 mM at pH 12.0) were prepared by diluting stock solutions of **2.1**-Eu^{II} (5.0 mM at pH 12.0) with aqueous solutions of KOH (0.01 M). These solutions were filtered using 0.2 micron filters and were used to calculate the quantum yields by plotting integrated emission (450–700 nm) vs absorption for coumarin-153 and **2.1**-Eu^{II} at pH 12.0. The gradients of the plots (**Figure 2.2**) were used to calculate the quantum yield using **eq 1**, where Φ_u and Φ_s are the quantum yields of sample **2.1**-Eu^{II} and coumarin-153 (0.58), respectively; $Grad_u$ and $Grad_s$ are the gradients of the plots of **2.1**-Eu^{II} (3.7×10^9) and coumarin-153 (8.0×10^9), respectively; and η_u and η_s are the refractive indices of the aqueous KOH (1.334 at pH 12.0) solution and ethanol (1.3611), respectively.[93,94]

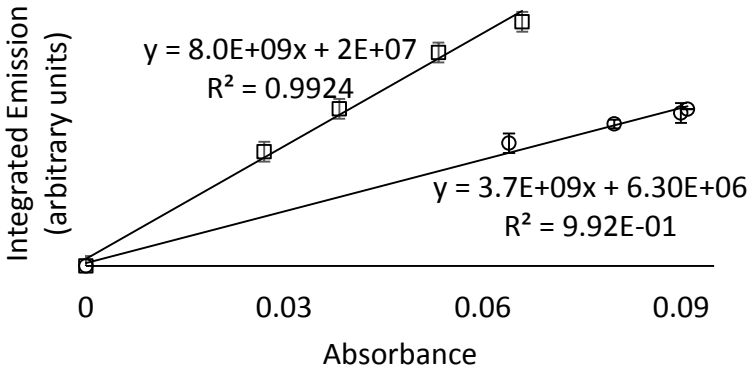

Figure 2.2. Integrated emission vs absorbance curves for coumarin-153 (□) in ethanol and complex **2.1**-Eu^{II} at pH 12.0 (○). Error bars represent the standard error of the mean of three independently prepared samples.

eq1.....$\Phi_u = \Phi_s \left(\frac{Grad_u}{Grad_s}\right)\left(\frac{{\eta_u}^2}{{\eta_s}^2}\right)$

Crystallographic Data

Single X-ray crystal structure analysis was performed on a Bruker APEX-II Kappa geometry diffractometer with Mo radiation and a graphite monochromator using a Bruker charge

coupled device based diffractometer equipped with an Oxford Cryostream low-temperature apparatus. The data was measured at a temperature of 100 K. The structure was solved by the direct method using the SHELXS-97 program that is part of APEX II2 and refined by the least squares method, SHELXL 2012 incorporated into ShelXle.[95] Single crystals of **2.1**-Eu^{II} contained one cation of **2.1**-Eu^{II}, one chloride counter ion, and one molecule of methanol in the asymmetric unit. The structure was solved with a resolution of 0.57 Å in space group P3c1. All non-hydrogen atoms were refined anisotropically and details are listed in **Table 2.1**.

Response to Red Alert: Plat 413 involves a solvent H atom from a methanol. The error in the calculated position of the methanol H atoms may be larger than the accuracy of the structure. However, the methanol has no relevant contribution to the conclusions in this chapter. Both SHFSU01 and PLAT080 are due to disorder, possibly due to racemic twinning (Flack x parameter = 0.446), in the structure which places disordered atoms so close to one another that individual electron density positions cannot be seen. This type of disorder cannot be properly modeled. Additionally, this disorder yields a relatively large, flat potential energy minimum between adjacent positions such that each refinement cycle shifts atoms back and forth between the adjacent atomic positions. The positions are close enough to one another to be indistinguishable, but will never reach the minimum set by SHELX regardless of the number of cycles of refinement because the atoms oscillate between their broad minima.

Table 2.1. Crystal data for complex **2.1**-Eu^{II}

Chemical formula	$C_{18}H_{40}Cl_2EuN_8O$	
Formula weight	607.44	
Temperature	100(2) K	
Wavelength	0.71073 Å	
Crystal system	trigonal	
Space group	P 3 c 1	
Unit cell dimensions	a = 16.4389(6) Å	α = 90°
	b = 16.4389(6) Å	β = 90°
	c = 16.3399(8) Å	γ = 120°
Volume	3824.1(3) $Å^3$	
Z	6	
Density (calculated)	1.583 g/cm^3	
Absorption coefficient	2.695 mm^{-1}	
F(000)	1854	

2.3 Results and Discussion

In the pursuit of oxidatively stable Eu^{II}-containing complexes for use as contrast agents for magnetic resonance imaging,[6,8,69,90,96] Eu^{II}-containing aza-222 cryptate, **2.1**-Eu^{II} (**Figure 2.1**), was synthesized with the thought that the nitrogen donors and cavity size would be a good match for Eu^{II}, resulting in an oxidatively stable complex. Complex **2.1**-Eu^{II} has a high oxidative stability (0.13 ± 0.05 V vs Ag/AgCl), and interestingly, aqueous solutions of **2.1**-Eu^{II} were yellow and highly luminescent (**Figure 2.3**).

To characterize the luminescence properties of **2.1**-Eu^{II}, excitation and emission spectra in aqueous medium (**Figure 2.3**) were acquired. The excitation of **2.1**-Eu^{II} occurs at 380–520 nm (λ_{ex}^{max} = 415 nm) resulting in a broad yellow emission (500–700 nm, λ_{em}^{max} = 580 nm). The broad excitation and emission spectra are likely due to Laporte allowed f–d transitions between ground ($4f^7$) and excited ($4f^65d^1$) states. The redshift observed from blue emitting Eu^{II}-containing complexes to a yellow emitting complex **2.1**-Eu^{II} is most probably aroused from the strong field

effect of the amine-rich macrocycle compared to blue emitting Eu^{II}-containing crown ethers and cryptand complexes.[97] As a result of the strong ligand field effect, energy of the lowest 5d state decreases leading to a redshift in emission wavelength. Similar shifts in excitation and emission spectra have been observed for Eu^{II} in the solid state,[36] but not in aqueous solutions. Further, besides not displaying yellow emission in aqueous media, Eu^{II} containing complexes are usually weak emitters at ambient temperature because of quenching from inner sphere OH oscillators.[98-103] However, despite being in an aqueous solution, complex **2.1**-Eu^{II} that is stable under ambient light under Ar for days displays bright yellow luminescence. To quantify the luminescence of **2.1**-Eu^{II}, its quantum yield (26%) was measured. This value is, to the best of my knowledge, the highest quantum yield reported for a Eu^{II}-containing complex in aqueous media.

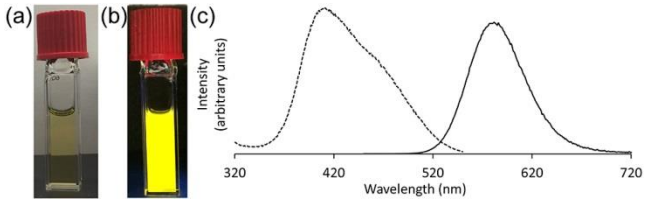

Figure 2.3. Pictures of **2.1**-Eu^{II} (5.0 mM) in 4 mL cuvettes in a pH 12.0 solution of KOH (a) in ambient light and (b) under a hand held UV lamp (254–400 nm). (c) Excitation (---) and emission (—) spectra of **2.1**-Eu^{II} (0.50 mM) in a pH 12.0 solution of KOH.

To explore the influence of pH on luminescence, emission spectra at pH 12.0, 11.3, 10.0, 9.5, and 8.0 (**Figure 2.4**) were acquired. Luminescence intensity decreased with decreasing pH. Further, the yellow emission disappeared near completely at pH 8. The observed decrease in intensity with decreasing pH is likely due to protonation of the metal-bound secondary amines ($pK_a \approx 13–14$)[104] of the ligand giving rise to NH oscillators that quench the luminescence of Eu^{II}. NH oscillators were suspected to quench the excited state of complex **2.1**-Eu^{II} for two reasons: (1) NH oscillators quench the excited state energies of Eu^{III}, and Eu^{III} and yellow-emitting Eu^{II}-containing complexes have similar excited state energies;[36,79-81,42,86,87,98,103] and (2) similar oscillators to NH (OH and BH) quench the excited state energy of both Eu^{II} and Eu^{III},[36,79-

[81,42,86,87,98,103] Furthermore, protonation of too many of the amines of the ligand could also facilitate demetalation, which would lead to a decrease in emission intensity.

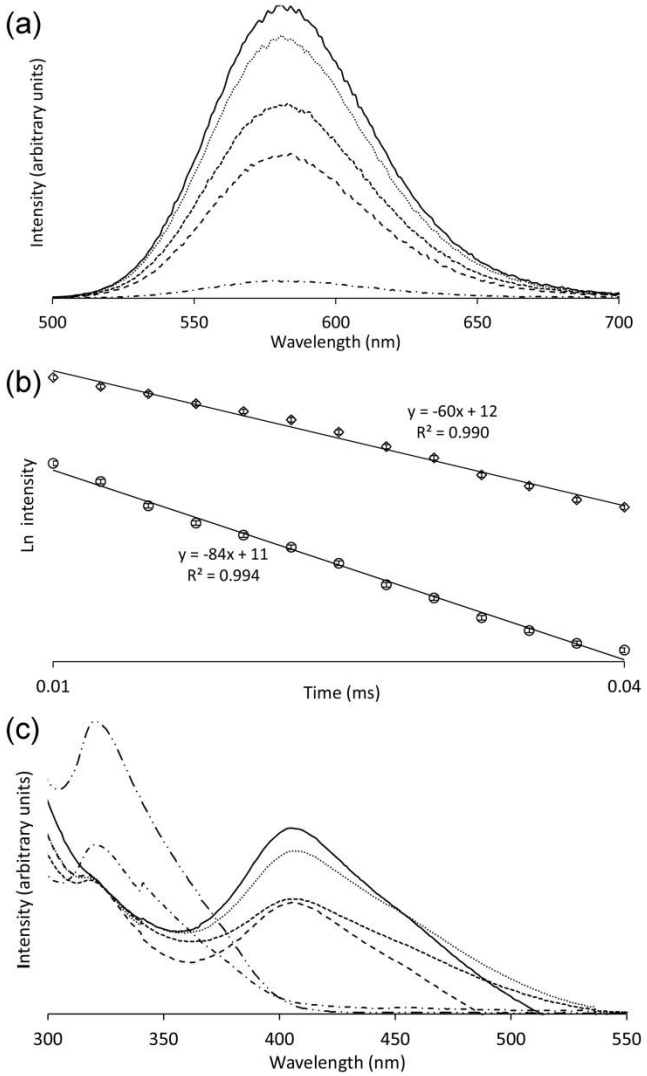

Figure 2.4. (a) Emission spectra (λ_{ex} = 415 nm) of **2.1**-Eu^{II} at pH 12.0 (—), 11.3 (··), 10.0 (--), 9.5 (– –), and 8.0 (– · –); (b) Plots of the natural log of luminescence intensity vs time at pH 12.0 in H_2O (◊), and at pH 9.5 in H_2O (○) (λ_{em} = 580 nm, λ_{ex} = 415 nm). Lines are the linear best fit, and the decay rates were derived as the slopes of the lines; (c) absorption spectra of **2.1**-Eu^{II} at pH 12.0 (—), 11.3 (··), 10.0 (--), 9.5 (– –), and 8.0 (– · –) and $EuCl_2$ (— ·· —) at pH 8.0. Error bars indicate the standard error of the mean of three independently prepared samples.

To test for the presence of NH oscillators, luminescence-decay rate data were acquired at pH 9.5 and 12.0 in H_2O (**Figure 2.4**). The gradients of the plots of Ln intensity vs time yielded the decay-rates. The decay-rates obtained from the plots are 60 and 84 ms^{-1} at pH 12.0 and 9.5, respectively. These results suggest that more amines are protonated at pH 9.5 than at 12.0

because more NH oscillators would increase decay rate. To test for the demetalation of Eu^{II} at lower pH values, the absorption spectra of **2.1**-Eu^{II} was acquired at pH 12.0, 11.3, 10.0, 9.5, and 8.0 (**Figure 2.4**). As pH was decreased, the intensity of the peak at 415 nm decreased, while a peak at 320 nm increased in intensity. The new peak at 320 nm aligned with the peak from uncomplexed $EuCl_2$ suggesting the occurrence of demetalation at lower pH values. Based on these data, the decrease in emission intensity of **2.1**-Eu^{II} with decreasing pH is likely a combination of quenching from protonated amines and demetalation.

To relate the luminescence behavior of **2.1**-Eu^{II} to its structure, the coordination environment of **2.1**-Eu^{II} were studied in the solid state and in solution. The crystal structure of **2.1**-Eu^{II} shows that Eu^{II} is coordinated to all eight nitrogens of the ligand and to a chloride ion in a distorted staggered hula-hoop geometry (**Figure 2.1**).[105] The feet of the structure comprise N2 and N3, and the remaining nitrogen atoms compose the hoop. There is also a non-coordinated chloride counter ion and a molecule of methanol in the unit cell (not shown for clarity). Importantly, the crystal structure shows no inner sphere solvent molecules; therefore, if the solid-state structure is indicative of solution behavior, then the bright luminescence of **2.1**-Eu^{II} is likely a result of the absence of inner-sphere, solvent-based OH oscillators. If protonated, the NH oscillators of the ligand are capable of quenching the excited state of Eu^{II}, and the geometry around the secondary amines coordinated to Eu^{II} and combustion analysis of **2.1**-Eu^{II} suggest that the amines are protonated in the solid state; however, the solution measurements (**Figure 2.4**) suggests that these NH oscillators are not as prevalent at high pH values relative to lower pH values. Consequently, NH oscillators appear to not be contributing as much to the quenching of the excited state of Eu^{II} at high pH values (~12) relative to lower pH values. At intermediate pH values (11.3–9.5) quenching from NH oscillators seem to be dominant as the free Eu^{II} peak at 320 nm is low intense, but at lower pH values (~8) demetalation seems to be the major reason to

observe a decrease in emission intensity of **2.1**-Eu^{II} as can be seen from the high intense free Eu^{II} emission.

To determine the relationship between the solid- and solution-phase behaviors of **2.1**-Eu^{II}, we characterized the coordination environment of **2.1**-Eu^{II} in aqueous media using the continuous variation method (Job plot), variable-temperature ^{17}O-NMR spectroscopy, and conductivity measurements.

A Job plot was used to determine the stoichiometry of binding between Eu^{II} and the ligand using the integrated emission at 580 nm (λ_{ex} = 415 nm) to determine if the metal-to-ligand ratio in solution matched the solid state structure. This technique can be used to determine metal-to-ligand ratios in solution by examining a property of the complex as a function of the mole fraction of metal.[106] Maximum complex formation occurred at a stoichiometry of 1:1 between $EuCl_2$ and aza-222 cryptand, **2.1** (**Figure 2.5**). This result demonstrates consistency between the solid and solution structure of **2.1**-Eu^{II}. Despite this consistency, the Job plot analysis is inconclusive with respect to coordinated solvent molecules in solution.

Variable-temperature ^{17}O-NMR spectroscopy was used to test for the presence of coordinated water in **2.1**-Eu^{II} in solution. This technique can be used to determine the number of exchangeable water molecules coordinated to a paramagnetic metal ion using the difference in line widths of ^{17}O peak of a paramagnetic metal complex and that of a similar diamagnetic metal complex.[90] the differences in line widths of **2.1**-Eu^{II} and its diamagnetic Sr^{II}-containing aza-222 cryptate analog (Sr^{II} and Eu^{II} have similar charge densities)[80] were measured at seven temperatures between 250 and 310 K (**Figure 2.5**). The calculated R_{2P} (difference in linewidths × π) did not show an exponential correlation with temperature; therefore, either there are no exchangeable water molecules coordinated to the Eu^{II} center or coordinated water molecules are exchanging rapidly ($\geq 2 \times 10^{11}$ s^{-1}).[107,108] While ^{17}O-NMR spectroscopy data support a lack of

coordinated H_2O molecules in solution, the results of the experiment are inconclusive, and another technique was needed to probe the coordination environment of Eu^{II} in solution.

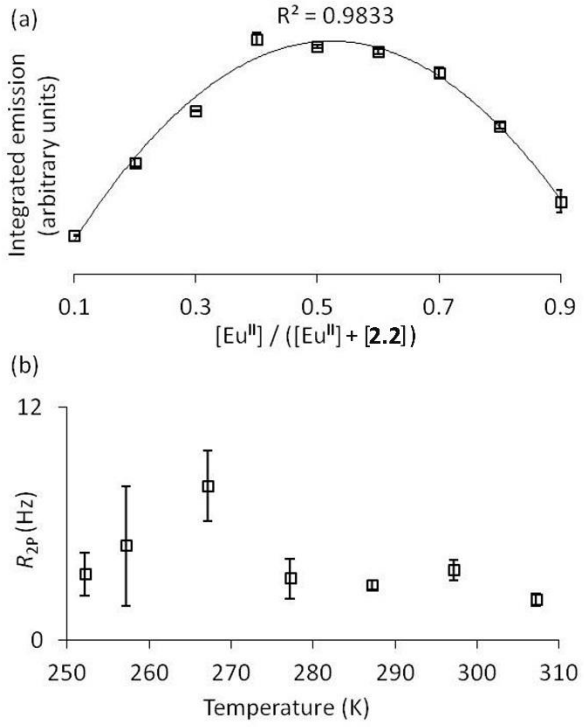

Figure 2.5. (a) Job plot for **2.1**-Eu^{II}. Data were fitted using a polynomial function. (b) Variable-temperature ^{17}O-NMR data for **2.1**-Eu^{II} at pH 12.0. Error bars represent the standard error of the mean from three independently prepared samples for both (a) and (b).

Molar conductivity was determined to investigate the coordination of chloride ion in solution. For **2.1**-Eu^{II}, molar conductivity was calculated at pH 10.0 (pH was not adjusted to 12.0 with KOH to avoid adding more ions) from the measured conductivity of **2.1**-Eu^{II} (137 ± 2 S mol^{-1} cm^2). The molar conductivity is within the range of 1:1 ion dissociation in water (96–150 S mol^{-1} cm^2 for 1:1 dissociation).[109] These data suggest that the chloride ion is likely coordinated to the metal center even in an aqueous basic solution because to achieve a 1:1 ion dissociation, only one cation and one anion can be present. A possible explanation for this observation is based on hard–soft acid–base theory,[110,111] which predicts that the relatively soft Eu^{II} ion in **2.1**-Eu^{II} is better matched to chloride relative to oxygen donors. The results of the conductivity

measurements together with the other solution-phase studies indicate that the structure in solution is similar to the solid-phase structure.

2.4 Conclusions

In conclusion, a Eu^{II}-containing complex was synthesized that displays bright yellow emission in aqueous media with a quantum yield of 26%. Solid-state and solution-phase characterization indicate 1:1 metal-to-ligand coordination and the absence of directly coordinated OH oscillators. These results demonstrate a new Eu^{II}-containing luminescent probe in aqueous medium with high quantum yield that has the potential to be used in aqueous-based luminescence applications.

CHAPTER 3: INFLUENCE OF COORDINATION ENVIRONMENT ON THE PHYSICOCHEMICAL PROPERTIES OF EU^{II}-CONTAINING CRYPTATES

3.1 Introduction

This chapter describes synthesis of a series of four cryptates that was used to study the influence of ligand structure on the physicochemical properties of Eu^{II}-containing cryptates. Eu^{II}-containing cryptates have potential applications in luminescent materials and contrast agent for magnetic resonance imaging.[6,42,69,71,86,90,96,112-114] This study enables the understanding of how changes in cryptand structure influence physicochemical properties including structural, photochemical, and redox properties of Eu^{II}-containing cryptates. To study the physicochemical properties of Eu^{II}-containing cryptates, a series of Eu^{II}-containing cryptates (**Figure 3.1**) was synthesized and characterized with elemental analysis, X-ray crystallography, absorption and emission spectroscopies, cyclic voltametry, and conductivity measurements.

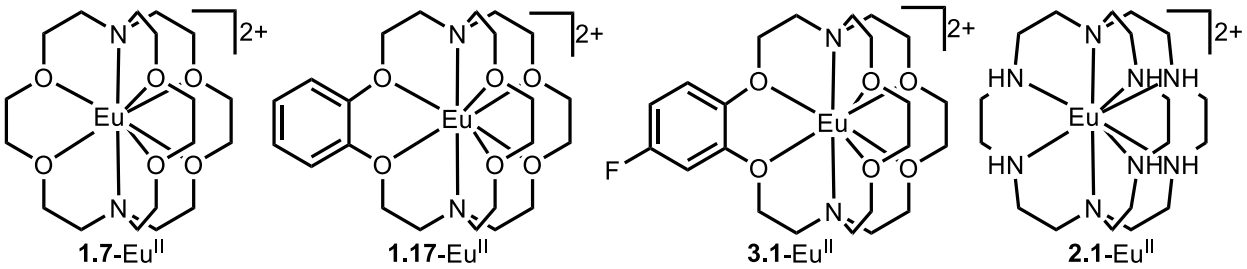

Figure 3.1. Eu^{II}-containing cryptates used in this study

The rationale behind the ligand selection was to choose a series of cryptands with coordinating atoms that are relatively strong or weak in Lewis basicity (ethers and amines) and metalated these cryptands with EuI_2 where iodide salt of Eu^{II} was chosen to increase the solubility in organic solvents. Physicochemical properties of these Eu^{II}-containing cryptates were measured in solution and compared to other Eu^{II}-containing cryptates. [6,42,69,71,86,90,96,112-114] Furthermore, the structures described in this chapter focus on characterization techniques that are

not previously described for these complexes to provide an understanding of the properties of these potentially useful metal complexes.

3.2 Experimental Procedure

Commercially available chemicals were of reagent-grade purity or better and were used without further purification unless otherwise noted. Water was purified using a PURELAB Ultra Mk2 water purification system (ELGA). 4,7,13,16,21,24-Hexaoxa-1,10-diazabicyclo[8.8.8]hexacosane and 5,6-benzo-4,7,13,16,21,24-hexaoxa-1,10-diazabicyclo[8.8.8]hexacos-5-ene (**1.7** and **1.17**) were purchased from Sigma-Aldrich and used without further purification. 4-Fluoro-5,6-benzo-4,7,13,16,21,24-hexaoxa-1,10-diazabicyclo[8.8.8]hexacos-5-ene and azacryptand-1,4,7,10,13,16,21,24-octaazabicyclo[8.8.8]hexacosane (**3.1** and **2.1**) were prepared by following published procedures.[88,89,114] Commercially available anhydrous methanol was used after degassing for 1 h under vaccum. Tetrahydrofuran (THF) was dried using a solvent purification system (VAC, 2 columns of alumina), and the solvent was dispensed into a dry flask and degassed under reduced pressure.

Metalated complexes were synthesized in an oxygen- and moisture-free glovebox under an Ar atmosphere. UV–vis absorbences were measured using a Shimadzu UVmini-1240. Molar extinction coefficients were determined from the absorption spectra at different concentrations of metal complexes between 250 and 600 nm. Excitation and emission spectra were recorded using a HORIBA Jobin Yvon Fluoromax-4 spectrofluorometer. Molar conductivity was calculated from three independently prepared solutions of metal complexes (1.0 mM) in methanol under an Ar atmosphere and ambient temperature using an Omega CDH 280 portable conductivity meter that was calibrated with aqueous KCl (0.01 M, 1.413 mS cm^{-1}). Results are reported as mean ± standard error. Cyclic voltametry was performed using a Pine Wavenow USB potentiostat in an

electrochemical cell under an Ar atmosphere with a $Ag/AgNO_3$ reference electrode, a glassy carbon working electrode, and a Pt wire auxiliary electrode scan rates were set at 100 mV s^{-1}. Solutions of complexes (2.0 mM) and Et_4NClO_4 (0.1 M) in methanol (3.0 mL) were used for the analyses. Potentials are reported as potential ± standard error of the mean of three independently prepared samples.

Synthesis of 1.7-Eu^{II}, 1.17-Eu^{II}, 3.1-Eu^{II}, and 2.1-Eu^{II}: To separate solutions of cryptands **1.7**, **1.17**, **3.1**, and **2.1 (**0.075 mmol) in THF (1.5 mL) were added solutions of EuI_2 (0.075 mmol) in THF (1.5 mL), and the resulting precipitates were washed with THF (3 × 1 mL) under an Ar atmosphere. Solvent was removed under reduced pressure to yield the metal complexes. **1.17-Eu^{II}:** 65.0 mg (83%) of a white powder. Anal. Calcd for $C_{18}H_{36}N_2O_6EuI_2$: C, 27.64; H, 4.64; N, 3.58. Found: C, 27.94; H, 5.06; N, 3.78; **1.17-Eu^{II}**: 66.0 mg (80%) of a white powder. Anal. Calcd for $C_{22}H_{36}N_2O_6EuI_2$: C, 32.03; H, 4.68; N, 3.25. Found: C, 32.11; H, 4.63; N, 3.43; **3.1-Eu^{II}**: 70.0 mg (82%) of a white powder. Anal. Calcd for $C_{22}H_{35}N_2O_6FEuI_2$: C, 31.15; H, 4.16; N, 3.30. Found: C, 31.56; H, 4.15; N, 3.22; **2.1-Eu^{II}**: 69.0 mg (89%) of a white powder. Anal. Calcd for $C_{18}H_{42}N_8EuI_2$: C, 28.23; H, 5.74; N, 13.86. Found: C, 28.85; H, 5.93; N, 14.61. All values are given as percentages. Precipitated solids (~20 mg) were used to grow crystals using slow evaporation from methanol/THF 1:4 (1 mL) to result in crystalline powders of **3.1**-Eu^{II} and **2.1**-Eu^{II} that were used for X-ray analysis.

Absorption and emission spectra, elemental analysis (C, H, N) determination, Inductively coupled plasma mass spectroscopy (ICP-MS) and X-ray crystal structure analysis were performed as described in Chapter 2.

3.3 Results and Discussion

Solid-Phase Characterization. Crystal structures of **3.1**-Eu^{II} and **2.1**-Eu^{II} (**Figure 3.2**) were obtained. Crystal structures provide evidence of influence of the ligand environment on the

structural properties of complexes, and these structural properties are often useful to explain the properties measured in solution. The Eu^{II}-containing complexes **3.1**-Eu^{II} and **2.1**-Eu^{II} are nine-coordinate eclipsed and staggered hula-hoop geometries, respectively, and these geometries are similar to the geometries of **3.1**-Eu^{II} and **2.1**-Eu^{II} reported with the chloride counter ion.[113,114] The Eu^{II}–O and Eu^{II}–N bond lengths reported with iodide (**Table 3.1**) are in similar ranges with the reported Eu^{II}–O and Eu^{II}–N bond lengths of **3.1**-Eu^{II} (2.643–2.762 and 2.811–2.827 Å, respectively) and Eu^{II}–N (tertiary) bond lengths of **2.1**-Eu^{II} (2.846–2.921 Å) complexes with chloride counter ions.[113] The bond length of Eu–I in **3.1**-Eu^{II} is 0.391 Å shorter than that of **2.1**-Eu^{II}. The longer Eu–I bond length observed with **2.1**-Eu^{II} indicates a weaker interaction with the Eu^{II} ion than in **3.1**-Eu^{II}. Both Eu^{II}-containing complexes **2.1**-Eu^{II} and **3.1**-Eu^{II} are 9-coordinate, but the longer bond lengths observed between Eu and the tertiary amines (Eu–N3 and Eu–N6) of **2.1**-Eu^{II} compared to **3**.**1**-Eu^{II} (Eu–N1 and Eu–N2) are likely due to the structural strains caused by the six N–H bonds of the secondary amines.

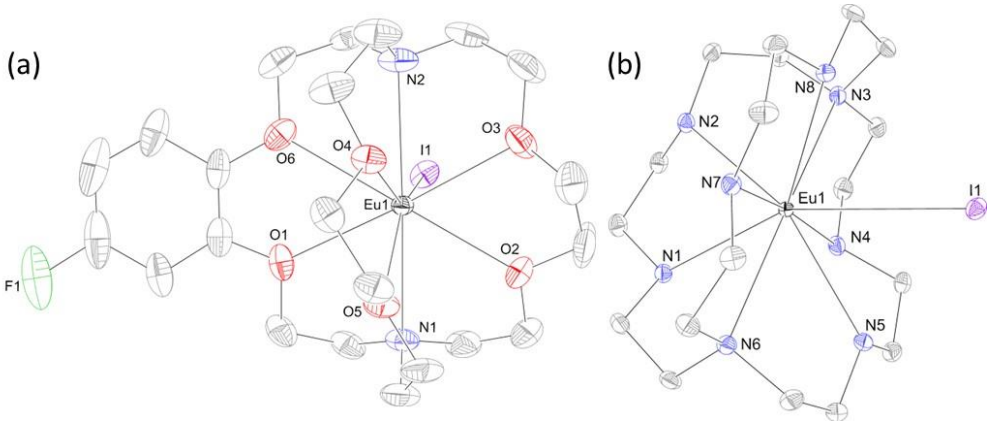

Figure 3.2. Crystal structures of (a) **3.1**-Eu^{II} and (b) **2.1**-Eu^{II}. Thermal ellipsoids are drawn at 50% probability. Hydrogen atoms, non-coordinated iodide ions, and methanol molecules are not shown for clarity.

Table 3.1. Selected bond lengths from crystallographic data

Complex	Bond	Bond length (Å)
3.1-Eu^{II}	Eu–N1	2.796
3.1-Eu^{II}	Eu–N2	2.819
3.1-Eu^{II}	Eu–I1	3.239
3.1-Eu^{II}	Eu–O1	2.742
3.1-Eu^{II}	Eu–O6	2.793
2.1-Eu^{II}	Eu–N3	2.901
2.1-Eu^{II}	Eu–N6	2.942
2.1-Eu^{II}	Eu–I1	3.630

Solution-Phase Characterization. To characterize the metal complexes in solution, Absorption and emission spectroscopy, conductivity measurements, and cyclic voltametry were used. Methanol was used as the solvent for each experiment because all of the complexes were soluble in methanol. The following sections describe the results of these characterization techniques.

Absorption Spectra. To probe the photochemical properties of Eu^{II}-containing cryptates of **1.7**, **1.17**, **3.1**, and **2.1** absorption spectra of these complexes were measured. These spectra provide insight into the nature of coordination environments including ligand field effects and strengths of metal-ligand interactions.[42,86,112,113] A series of absorption spectra (**Figure 3.3**) acquired for the four metal complexes resulting from the metalation of **1.7**, **1.17**, **3.1**, and **2.1** with EuI_2 in methanol is described in the following paragraphs.

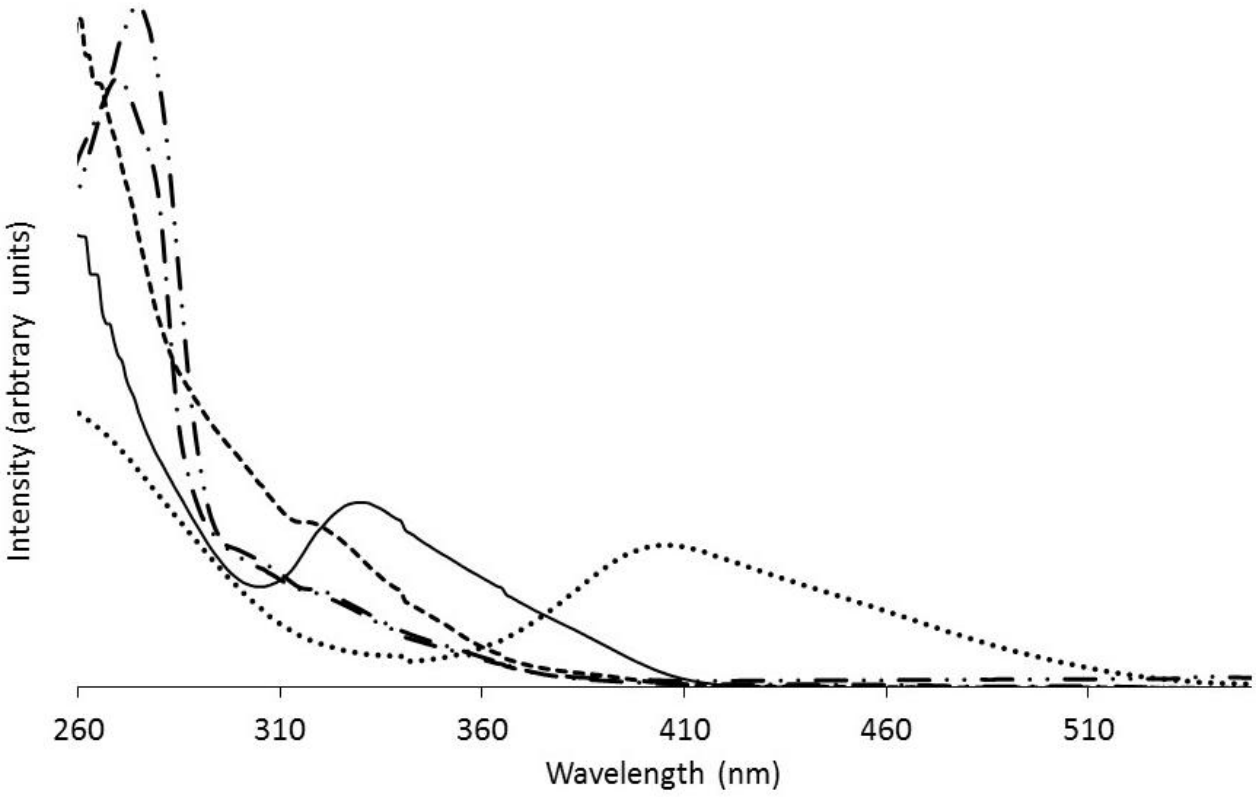

Figure 3.3. Absorption spectra of EuI_2 and Eu^{II}-containing cryptates (2.0 mM) in methanol: EuI_2 (—), **1.7**-Eu^{II} (- -), **1.17**-Eu^{II} (— · —), **3.1**-Eu^{II} (— · · —), and **2.1**-Eu^{II} (• •).

All of the absorption spectra corresponding to EuI_2 and Eu^{II}-containing cryptates displayed broad absorptions at wavelengths shorter than 300 nm, but low energy absorption peaks for complexes are distinct from uncomplexed EuI_2. In the low energy region (260–550 nm), EuI_2 displayed an absorption between 300 and 420 nm (λ_{max} = 329 nm). Complex **1.7**-Eu^{II} displayed a shoulder (~319 nm) on the high energy absorption, and **1.17**-Eu^{II} and **3.1**-Eu^{II} both displayed shoulders at ~310 nm. Complex **2.1**-Eu^{II} displayed a peak from 340 to 540 nm (λ_{max} = 404 nm). The peaks observed for EuI_2 and Eu^{II}-containing cryptates are assigned to transitions from f^7 ground state to f^6d^1 excited state based on the broadness of the peaks and their molar extinction coefficients that are on the order of 10^2–10^3 cm L mol^{-1}. These two features are consistent with reported spectra of Eu^{II}-containing complexes.[42,86,112,113] The higher energy absorption at 319 nm for **1.17**-Eu^{II} relative to 329 nm for EuI_2 is likely due to the weak ligand

field of ether-rich cryptands compared to methanol. The influence of the field strength on the excited state energy levels of Eu^{II} are shown in a schematic energy level diagram (**Figure 3.4**), where excited states of Eu^{II} is likely split into one higher energy state and one lower energy state compared to free Eu^{II} ion based on the appearance of two regions of peaks in the absorption spectra (one around 200–300 nm and other around 300–600 nm with molar extinction coefficients in the range of 10^2–10^3 cm L mol^{-1})[86,113] and the splitting energy representing the ligand field strength. The low energy absorption observed with **2.1**-Eu^{II} relative to uncomplexed EuI_2 is likely due to the strong field effect of the amine-rich cryptand compared to methanol or the ether-rich cryptands.

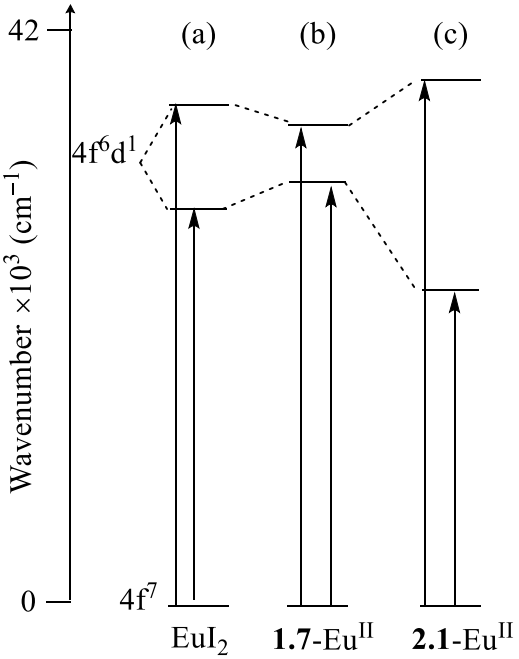

Figure 3.4. Schematic diagram of splitting of the excited state energy levels based on the maximum absorptions observed in methanol for (a) EuI_2, (b) **1.7**-Eu^{II} (c) **2.1**-Eu^{II}.

Emission Spectra. To further analyze the influence of ligand structure on the electronic structure of these metal complexes, emission spectra were recorded for **1.7**, **1.17**, **3.1**, and **2.1** with EuI_2 (**Figure 3.5**). Similar to absorption spectra, shifts in emission wavelengths and variation in emission intensities relate to the coordination environment of metal ions.[113] The

emission spectra of EuI_2 and Eu^{II}-containing cryptates **1.7**-Eu^{II}, **1.17**-Eu^{II}, and **3.1**-Eu^{II} displayed broad peaks around 400–550 nm with maximum emissions of 485, 468, 473, and 471 nm, respectively, whereas amine-rich cryptate **2.1**-Eu^{II} displayed a broad intense peak around 450–650 nm (λ_{max} = 546 nm). The intensity of the peak for **2.1**-Eu^{II} at 546 nm is ~17 times more intense than the peaks observed for other complexes at 400–550 nm. To investigate the reason for complex **2.1**-Eu^{II} to display higher intensity in emission than the Eu^{II}-containing cryptates of **1.7**, **1.17**, **3.1**, and **2.1**, the conductivity of a solution containing **2.1**-Eu^{II} were measured. Conductivity is a measure of the degree of ionization of a compound in solution indicating the strength of the interaction between the compound and the solvent. The measured value for the conductivity was 96 ± 5 S cm^2 mol^{-1}. This conductivity value indicates a 1:1 dissociation (80–115 S cm^2 mol^{-1} for 1:1 dissociation).[115] For the complex **2.1**-Eu^{II}, 1:1 dissociation is possible if one of the iodide ions remains coordinated in solution. A previous report of **2.1**-Eu^{II} with chloride counter ions demonstrated that the chloride counter ion is likely coordinated in solution and absence of coordinated solvent likely contributed to the higher emission intensity of **2.1**-Eu^{II};[113] therefore, the high intensity emission of **2.1**-Eu^{II} with iodide counter ion could also be due to the absence of coordinated solvent. Ether-rich cryptates on the other hand only minimally (~3×) increased the emission of the solvated Eu^{II} ion. The reason for the lower intensities of ether-rich cryptates compared to **2.1**-Eu^{II} is likely increased solvent interactions as evident from the conductivity data (117–130 S cm^2 mol^{-1}) that suggest that ionization is greater than 1:1. Similar conductivity values have been reported for 2:1 dissociation of metal complexes.[116]

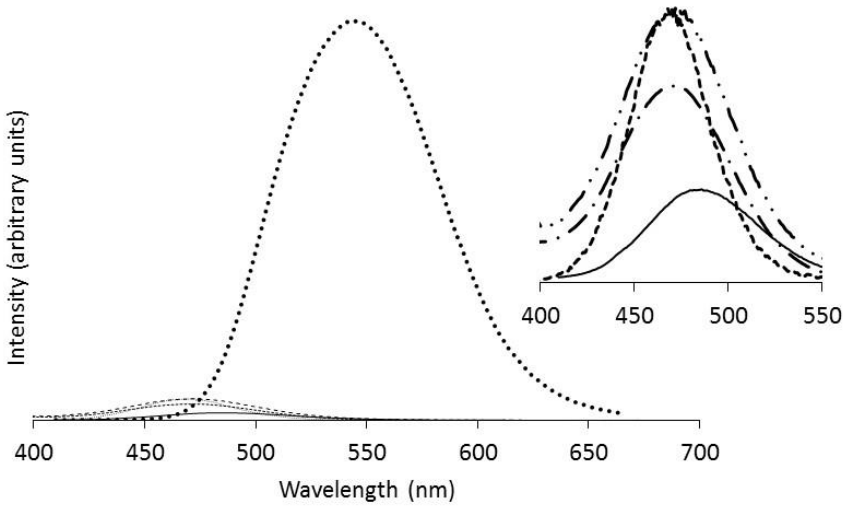

Figure 3.5. Emission spectra of solvated metal ions and complexes (2.0 mM) in methanol: EuI_2 (—), **1.7**-Eu^{II} (- -), **1.17**-Eu^{II} (— · —), **3.1**-Eu^{II} (— · · —), and **2.1**-Eu^{II} (• •).

Cyclic Voltammetry. Coordination environment not only influences photochemical properties but also redox properties.[8] For the complexes synthesized using cryptands **1.7**, **1.17**, **3.1**, and **2.1** with EuI_2, redox potentials were measured using cyclic voltammetry. Cyclic voltamograms of EuI_2 displayed a quasi-reversible peaks with an oxidation peak potential of –0.49 V and reduction peak potential of –0.80 V (**Figure 3.6**). Complex **1.7**-Eu^{II} displayed an oxidation peak at –0.27 V and reduction peak at –0.57 V. The voltamograms of **1.7**-Eu^{II} and EuI_2 displayed a quasi-reversible two step redox couple in the range of –0.10 to 0.30 V that was assigned to I^-/I_2. Peaks for cryptates **1.17**-Eu^{II}, and **3.1**-Eu^{II} could not be observed, because likely these oxidation peak potentials overlap with I^-/I_2 peaks based on the positive shifts in oxidation peaks from solvated Eu^{II} ion reported for **1.17**-Eu^{II}, and **3.1**-Eu^{II} in aqueous media.[8] Complex **2.1**-Eu^{II} displayed an oxidation peak at –0.80 V that was 0.31 V more negative than EuI_2. This observation is consistent with redox potentials observed with other strong field ligands coordinated to Ln^{II} in organic media,[117] where amine-containing ligands shift the oxidation peak more negative compared to the solvated ion. Complexes **1.7**-Eu^{II}, **1.17**-Eu^{II}, and **3.1**-Eu^{II} are all reported in aqueous media to form oxidatively stable complexes relative to the Eu^{II} solvated ion.

A reason for the stabilization is that the Eu^{II} ion in water are surrounded by more basic ligands such as water relative to ethers making electron density around Eu^{II} ion high, that makes Eu^{II} oxidation state unstable, but surrounding the ion with less basic ligands increase the stabilization of the +2 oxidation state and also macrocyclic ligands limit the interactions with the more basic solvent molecules enabling the stability of +2 oxidation state.

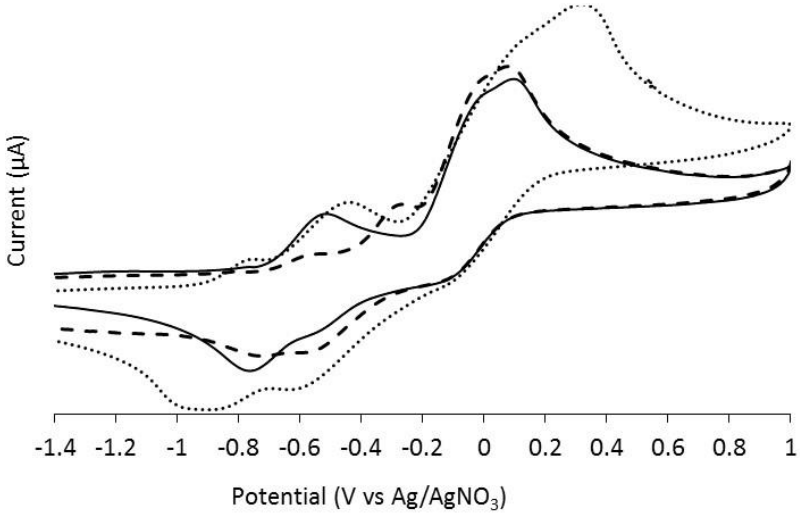

Figure 3.6. Cyclic voltammetry data for EuI_2 (—), **1.7**-Eu^{II} (- -), and **2.1**-Eu^{II} (• •)

3.4 Conclusions

Structural, photochemical, and redox properties of Eu^{II}-containing cryptates displayed strong dependency on the coordination environment of the Eu^{II} ion. Amine-rich cryptates shifted the absorption and emission peaks to lower energy relative to EuI_2 and oxidative potentials to more negative values relative to EuI_2. These shifts are in the opposite direction to the shifts imposed by ether-rich cryptates and the shift is greater with amine-rich cryptates indicating greater orbital interactions between strong-field ligands and Eu^{II} ion. Structural, photochemical, and redox properties of Eu^{II}-containing cryptates described in this chapter are in accordance with the structural, photochemical, and redox properties reported with Eu^{II}-containing complexes with strong- and weak-field coordination environments.

CHAPTER 4: INFLUENCE OF LIGAND STRUCTURE ON THE PHYSICOCHEMICAL PROPERTIES OF Yb^{II}-CONTAINING CRYPTATES

4.1 Introduction

The unique photochemical, redox, and magnetic properties of Ln^{II} ions play a vital role in applications spanning optoelectronics, sensors, reducing agents, catalysts, and imaging.[9,26,36,38,79-81,118] Because these physicochemical properties are influenced by coordination environment,[5,45,119-121] it is important to understand the influence of ligand structure on the properties of Ln^{II} ions to expand the potential uses of Ln^{II}-containing complexes. In this chapter, a series of Yb^{II}-containing cryptates and how their structural properties relate to electronic structure are described.

Among Ln^{II}-containing cryptates, there is a rich body of knowledge of the photochemical, magnetic and redox properties of Eu^{II}-containing cryptates relevant to applications including chemical reductions, luminescent materials, and magnetic resonance imaging.[6,8,42,69,71,72,86,90,96,112-114,122,123] This set of ligands has a dramatic influence on the properties of the Eu^{II} ion, and these ligands likely have similar influences on other Ln^{II} ions.[42,72,86,112,113] The Yb^{II} ion was focused on because this ion binds ligand **1.7** and because complexes of the Yb^{II} ion have properties that are useful in catalysis, chemical reductions, and luminescent materials.[81,112] However, the Yb^{II} ion is one of six Ln^{II} ions that are thought to display minimal metal-ligand orbital interactions.[5] To study the influence of ligand structure on physicochemical properties of Yb^{II}-containing complexes, a series of four cryptands with different coordinating atoms (N or O) and substituted and unsubstituted aromatic functionalities were used (**Figure 4.1**). These structural variations were chosen to allow comparisons to previous reports of Ln^{II}-containing cryptates.[6,8,42,69,71,72,86,90,96,112-114,122,123]

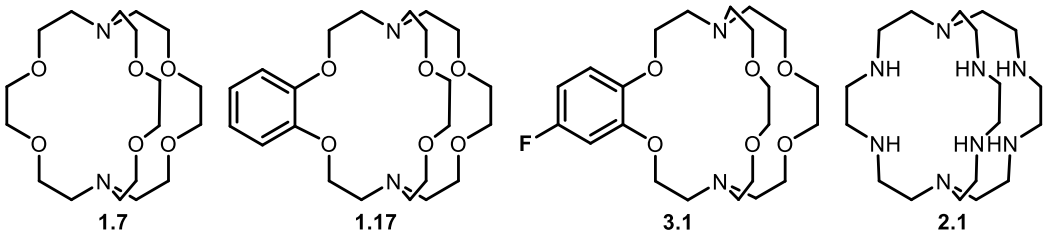

Figure 4.1. Cryptands used in this study

4.2 Experimental Procedures

Ligand synthesis, UV–vis absorbences, Molar extinction coefficients, excitation and emission spectra, molar conductivities, cyclic voltametry measurements, and X-ray crystallography were performed as described in Chapters 2 and 3. Inductively coupled plasma mass spectrometry analyses were used to determine metal concentrations and were performed with an Agilent 7700x inductively coupled plasma mass spectrometer in the Lumigen Instrument Center in the Department of Chemistry at Wayne State University. Standards of Yb were prepared by diluting commercially available standards (1000 ppm of Yb_2O_3 in aqueous nitric acid (5%), Alfa Aesar) with aqueous nitric acid (2%).

Synthesis of 1.7-Yb^{II}, 1.17-Yb^{II}, 3.1-Yb^{II}, and 2.1-Yb^{II}: To separate solutions of cryptands **1.7**, **1.17**, **3.1**, and **2.1** (0.075 mmol) in tetrahydrofuran (1.5 mL) were added solutions of YbI_2 (0.075 mmol) in tetrahydrofuran (1.5 mL), and the resulting precipitates were washed with tetrahydrofuran (3 × 1 mL) under an Ar atmosphere. Solvent was removed under reduced pressure to yield the metal complexes. **1.7-Yb^{II}**: 50.0 mg (83%) of a white powder. Anal. Calcd for $C_{18}H_{36}N_2O_6YbI_2$: C, 26.91; H, 4.52; N, 3.49. Found: C, 26.31; H, 4.51; N, 3.29; **1.17-Yb^{II}**: 45.0 mg (70%) of a white powder. Anal. Calcd for $C_{22}H_{36}N_2O_6YbI_2$: C, 31.27; H, 4.56; N, 3.17. Found: C, 31.24; H, 4.38; N, 3.21; **3.1-Yb^{II}**: 47.0 mg (77%) of a white powder. Anal. Calcd for $C_{22}H_{35}N_2O_6FYbI_2$: C, 30.39; H, 4.06; N, 3.22. Found: C, 30.44; H, 4.02; N, 3.33; **2.1-Yb^{II}**: 51.0 mg (85%) of a white powder. Anal. Calcd for $C_{18}H_{42}N_8YbI_2$: C, 27.51; H, 5.59; N, 13.51. Found:

C, 27.88; H, 5.38; N, 13.50. All values are reported as percentages. The precipitated solids (~20 mg) were used to grow crystals using slow evaporation from methanol/tetrahydrofuran (1:4, 1 mL) for X-ray analyses.

Table 4.1. Crystallographic properties of **3.1**-Yb^{II}

Chemical formula of **3.1**-Yb^{II}	$C_{21}H_{34}FI_2N_6O_3Yb$	
Formula weight	864.38	
Temperature	100(2) K	
Wavelength	0.71073 Å	
Crystal system	monoclinic	
Space group	P 1 21/n 1	
Unit cell dimensions	a = 9.5066(15) Å	α = 90°
	b = 16.758(3) Å	β = 102.695(6)°
	c = 17.788(3) Å	γ = 90°
Volume	2764.6(7) $Å^3$	
Z	4	
Density (calculated)	2.077 g/cm^3	
Absorption coefficient	5.656 mm^{-1}	
F(000)	1644	

Table 4.2. Bond lengths (Å) of **3.1**-Yb^{II}

Yb1-O4	2.501(3)	Yb1-O2	2.503(3)
Yb1-O3	2.545(3)	Yb1-O1	2.590(3)
Yb1-O5	2.690(3)	Yb1-N3	2.752(3)
Yb1-N4	2.767(3)	Yb1-O6	2.801(3)
Yb1-I1	3.1521(5)	F1-C17	1.353(6)
C7-O1	1.434(6)	C7-C8	1.514(8)
C7-H7A	0.99	C7-H7B	0.99
O2-C9	1.398(6)	O2-C8	1.412(5)
C22-N4	1.482(6)	C22-C9	1.501(8)
C22-H22A	0.99	C22-H22B	0.99
O3-C1	1.430(5)	O3-C21	1.452(5)
O4-C3	1.412(6)	O4-C2	1.437(5)
N3-C15	1.437(6)	N3-C4	1.499(6)
N3-C5	1.503(6)	N4-C20	1.467(5)
N4-C10	1.509(6)	O6-C12	1.361(5)
O6-C11	1.446(6)	O5-C13	1.369(5)
O5-C14	1.475(6)	C1-C2	1.508(6)
C1-H31	0.99	C1-H32	0.99
C2-H29	0.99	C2-H30	0.99
C3-C4	1.499(7)	C3-H27	0.99
C3-H28	0.99	C4-H25	0.99
C4-H26	0.99	C5-C6	1.522(7)
C5-H4	0.99	C5-H3	0.99
C6-O1	1.388(6)	C6-H5	0.95
C8-H24	0.99	C8-H23	0.99
C9-H21	0.99	C9-H22	0.99
C10-C11	1.469(7)	C10-H7	0.99
C10-H6	0.99	C11-H16	0.99
C11-H15	0.99	C12-C13	1.392(7)
C12-C19	1.405(6)	C13-C16	1.379(6)
C14-C15	1.504(7)	C14-H11	0.99
C14-H8	0.99	C15-H9	0.99
C15-H10	0.99	C16-C17	1.387(8)
C16-H14	0.95	C17-C18	1.380(10)
C18-C19	1.350(9)	C18-H12	0.95
C19-H13	0.95	C20-C21	1.507(7)
C20-H20	0.99	C20-H17	0.99
C21-H18	0.99	C21-H19	0.99

Table 4.3. Crystallographic properties of **2.1**-Yb^{II}

Chemical formula of **2.1**-Yb^{II}	$C_3H_6I_{0.33}N_{1.33}Yb_{0.17}$	
Formula weight	131.90	
Temperature	100(2) K	
Wavelength	0.71073 Å	
Crystal system	trigonal	
Space group	P -3 1 c	
Unit cell dimensions	a = 9.4532(6) Å	α = 90°
	b = 9.4532(6) Å	β = 90°
	c = 16.6972(11) Å	γ = 120°
Volume	1292.21(18) $Å^3$	
Z	12	
Density (calculated)	2.034 g/cm^3	
Absorption coefficient	6.028 mm^{-1}	
F(000)	752	

Table 4.4. Bond lengths (Å) of **2.1**-Yb^{II}

Yb1-N2	2.6008(10)	Yb1-N2	2.6009(10)
Yb1-N2	2.6009(10)	Yb1-N2	2.6009(10)
Yb1-N2	2.6009(10)	Yb1-N2	2.6009(10)
Yb1-N1	2.7231(17)	Yb1-N1	2.7231(17)
N1-C2	1.4777(14)	N1-C2	1.4777(14)
N1-C2	1.4777(14)	N2-C3	1.4749(16)
N2-C1	1.4764(17)	C1-C2	1.5199(19)
C1-H1A	0.99	C1-H1B	0.99
C2-H2A	0.99	C2-H2B	0.99
C3-C3	1.512(3)	C3-H3A	0.99
C3-H3B	0.99		

4.3 Results and Discussion

Solid-Phase Characterization. Crystal structures of Yb^{II}-containing cryptates of ligands **1.7**, **1.17**, **3.1**, and **2.1** (**Figure 4.2**) provide evidence of the influence of ligand environment on the structural properties of complexes, and these structural properties are often useful to explain solution properties. The Yb^{II}-containing complex **3.1**-Yb^{II} adopts a nine-coordinate eclipsed

hula-hoop geometry, and **2.1**-Yb^{II} adopts an eight-coordinate bicapped trigonal antiprism geometry.[105,124] The bond lengths of five of the Yb^{II}–O bonds in **3.1**-Yb^{II} are between 2.501 and 2.690 Å, but the Yb–O6 bond is longer than the remaining Yb^{II}–O bonds (**Table 4.2**), indicating a weaker interaction of Yb^{II} with O6 than with other oxygen atoms. The Yb^{II}–O bond lengths of **3.1**-Yb^{II} (except Yb–O6) are in a similar range (2.490–2.690 Å) as other 9-coordinate Yb^{II}-containing complexes.[125] The 8-coordinate complex **2.1**-Yb^{II} adopts the rare bicapped trigonal antiprism geometry, and complex **2.1**-Yb^{II} is, to the best of our knowledge, the first reported Yb^{II}-containing complex with a bicapped trigonal antiprism geometry. The edges that are highlighted in red (**Figure 4.2d**) of the bicapped trigonal antiprism are equal in length (4.164 Å) and the two triangular planes are parallel to each other indicating a perfect bicapped trigonal antiprism geometry. The two tertiary amines act as the two capping ligands in the bicapped trigonal antiprism. The bond lengths between Yb^{II} and the tertiary amines (2.723 Å) in **2.1**-Yb^{II} are longer than reported Yb^{II}–N bond lengths (2.588–2.691 Å) of 8-coordinate Yb^{II}-containing complexes.[126] These slightly longer Yb^{II}–N bonds could be the result of the structural restrains imposed by the six N–H bonds of the macrocyclic ligand of **2.1**-Yb^{II}. Although the Yb^{II}–N bond lengths are slightly longer in **2.1**-Yb^{II} compared to reported bond lengths, the bond lengths between Yb^{II} and the tertiary amines in **2.1**-Yb^{II} are shorter than equivalent bonds in **3.1**-Yb^{II}. This decrease in bond length is likely due to the decreased coordination number from 9 to 8.[125]

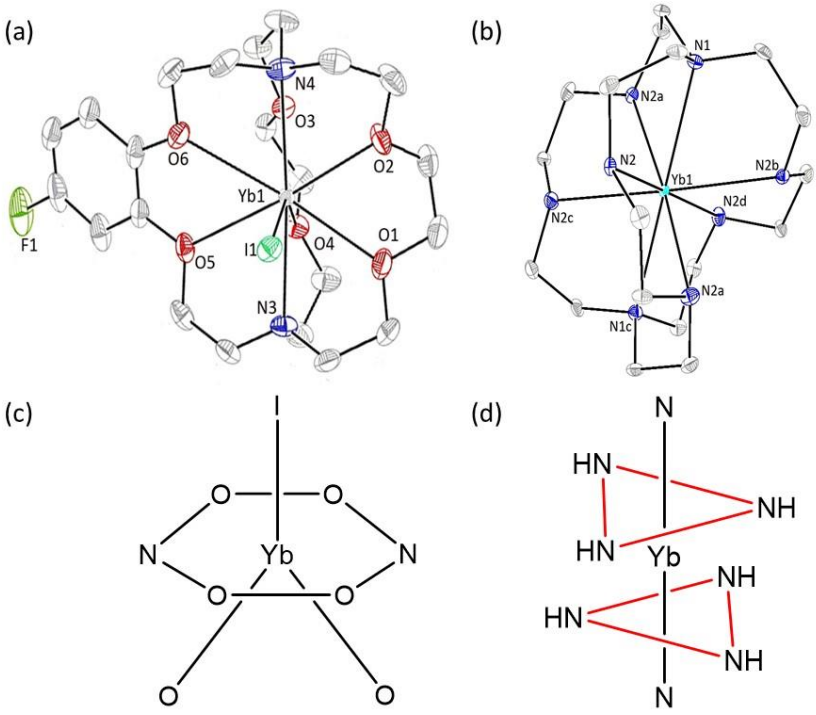

Figure 4.2. Crystal structures of (a) **3.1**-Yb^{II}, (b) **2.1**-Yb^{II}. Thermal ellipsoids are drawn at 50% probability. Hydrogen atoms, non-coordinated iodide ions, and methanol molecules are not shown for clarity. Schematic representation of (c) the eclipsed hula-hoop geometry of **3.1**-Yb^{II} and (d) the bicapped trigonal antiprism geometry of **2.1**-Yb^{II}.

A coordinated iodide was observed with **3.1**-Yb^{II} but not with **2.1**-Yb^{II}. The difference in coordination numbers of **3.1**-Yb^{II} and **2.1**-Yb^{II} is likely due to at least partially to the presence of the aromatic ring imposing rigidity to the carbon backbone and relatively low basicity to oxygen atoms O5 and O6.[8,127] Cryptand **2.1** likely binds more efficiently than **3.1** with Yb^{II} because of the eight strong Lewis base amine donors and the more flexible alkyl backbone in cryptand **2.1**. The Yb^{II}–(tertiary)N bonds are shorter in cryptate **3.1**-Yb^{II} than the Eu^{II}–(tertiary)N bonds of Eu^{II}-containing cryptates **3.1**-Eu^{II} (2.811–2.827 Å) and **2.1**-Eu^{II} (2.846–2.921 Å).[113,114] The shorter bond lengths in **3.1**-Yb^{II} are likely due to the smaller ionic radius of Yb^{II} (1.02 Å for coordination number 6) than Eu^{II} (1.17 Å for coordination number 6).[70] The exception to this trend is that the Yb–O6 distance in **3.1**-Yb^{II} is 0.039 Å longer than the equivalent Eu^{II}–O bond in **3.1**-Eu^{II}.[114] Additionally, both bonds between Yb^{II} and the two oxygen atoms bound to the

aromatic ring (Yb–O5 and Yb–O6) are considerably longer than the remaining Yb^{II}–O bonds (**Table 4.2**). These relatively long bonds near the aromatic ring are also observed with **3.1**-Eu^{II}.[114] A reason for the long metal–oxygen bonds on aromatic rings is likely the decreased Lewis basicity imparted by the electron-withdrawing aromatic rings.[127] Other metal–nitrogen and metal–oxygen bond lengths are only 0.06–0.08 Å shorter in **3.1**-Yb^{II} than in **3.1**-Eu^{II}.[114] Based on the difference in the ionic radii of Eu^{II} and Yb^{II} (~0.15 Å), the average bond lengths of **3.1**-Yb^{II} could be expected to be considerably shorter than the values reported here. The long bonds between Yb^{II} and the nitrogen and oxygen atoms are indicative of weaker interactions than those found with Eu^{II}.

Solution-Phase Characterization. To characterize the metal complexes in solution, absorption and emission spectra, conductivity, and cyclic voltametry. Methanol was used as the solvent for each experiment because all of the complexes were soluble in methanol. The following sections describe the results of these characterization techniques.

Absorption Spectra. To probe the photochemical properties of Yb^{II}-containing cryptates of **1.7**, **1.17**, **3.1**, and **2.1**, the absorption spectra of these complexes were measured. These spectra provide insight into the nature of coordination environments including ligand field effects and strengths of metal-ligand interactions.[128] A series of absorption spectra (**Figure 4.3**) acquired for the four metal complexes resulting from the metalation of **1.7**, **1.17**, **3.1**, and **2.1** with YbI_2 in methanol is described in the following paragraphs.

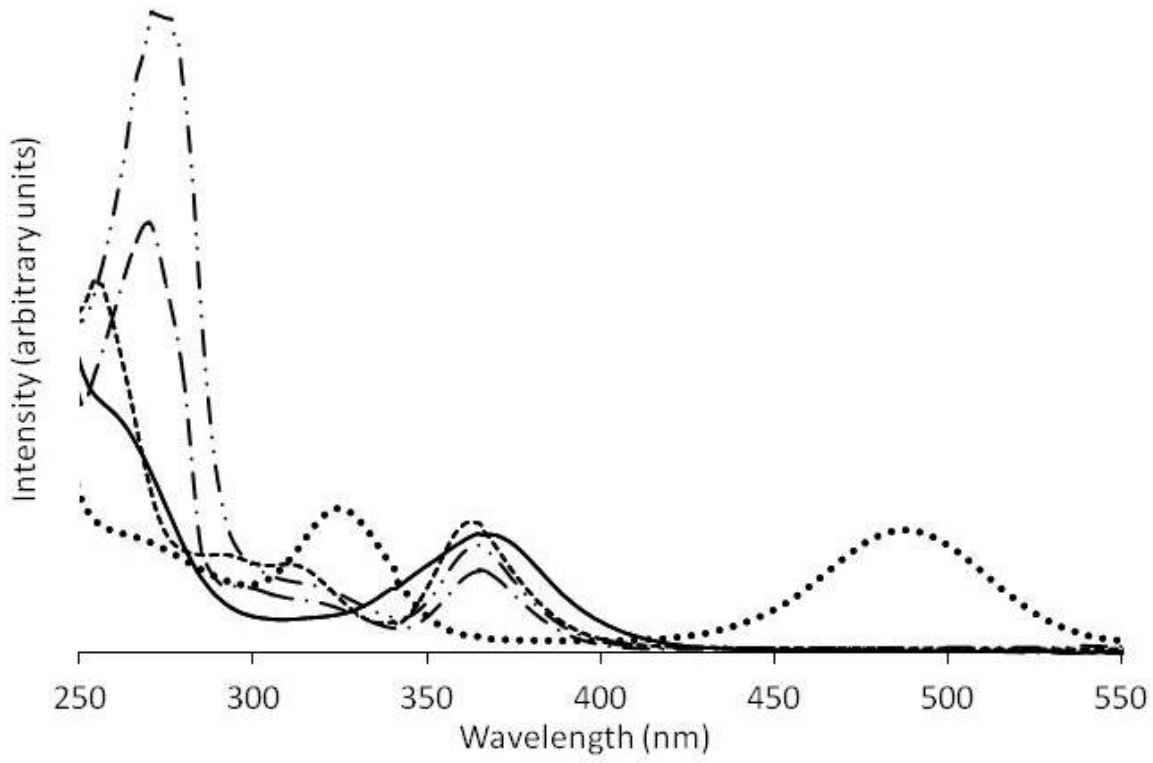

Figure 4.3. Absorption spectra of YbI_2 and Yb^{II}-containing cryptates (2.0 mM) in methanol: (a) YbI_2 (—), **1.7**-Yb^{II} (- -), **1.17**-Yb^{II} (— · —), **3.1**-Yb^{II} (— · · —), and **2.1**-Yb^{II} (• •).

Absorption spectra for YbI_2 and Yb^{II}-containing cryptates display similar trends to absorption spectra of reported Eu^{II}-containing cryptates.[42,86,113] YbI_2 and Yb^{II}-containing cryptates of ligands **1.7**, **1.17**, **3.1**, and **2.1** display intense peaks below 300 nm, and other peaks were observed between 300 and 550 nm that display different shifts based on coordination environment (**Figure 4.3**). The low energy absorption maxima for YbI_2, **1.7**-Yb^{II}, **1.17**-Yb^{II}, and **3.1**-Yb^{II} (368, 362, 365, and 364, respectively) were all within 6 nm of each other. In the case of **2.1**-Yb^{II}, two peaks were observed (**Figure 4.3**): a peak from 290 to 350 nm (λ_{max} = 323 nm) and another peak from 420 to 550 nm (λ_{max} = 485 nm). Absorptions of YbI_2 and Yb^{II}-containing complexes between 300 to 600 nm were assigned to transitions from an f^{14} ground state to an $f^{13}d^1$ excited state based on the molar extinction coefficient values measured for the lowest energy peaks (**Table 4.5**),[129] and splitting of the excited levels based on the observed absorptions are displayed schematically in **Figure 4.4**. Ether-rich cryptands that impose relatively weak

ligand field effects did not lead to higher energy absorptions as reported with similar complexes of the Eu^{II} ion,[42,86] but amine-rich cryptands that impose stronger ligand field effects led to lower energy absorptions than YbI_2, consistent with Eu^{II}-containing cryptates.[113] Based on the maximum absorption wavelengths of ether-rich Yb^{II}-containing cryptates, weak interactions with ether-rich cryptands are most likely due to the smaller size of the Yb^{II} ion relative to Eu^{II}.[70] The weak interactions of Yb^{II} with **1.7**, **1.17**, and **3.1** are supported by the Yb^{II}–N and Yb^{II}–O bond lengths of cryptate **3.1**-Yb^{II} that are only 0.06–0.08 Å shorter than the Eu^{II}–O and Eu^{II}–N bond lengths of the complexes formed with the same ligands.[114] With amine-rich cryptate **2.1**-Yb^{II}, the lowest energy absorption is shifted to longer wavelengths by 117 nm relative to YbI_2. This relatively large shift is indicative of strong metal–ligand interactions between Yb^{II} and the amines in **2.1**.

Table 4.5. Excitation and emission wavelengths and molar extinction coefficients

Metal complex	λ_{ex} (nm)	λ_{em} (nm)	Molar extinction coefficient (M^{-1} cm^{-1}) of λ_{ex}
1.7-Yb^{II}	362	471	784
1.17-Yb^{II}	365	460	552
3.1-Yb^{II}	364	460	542
2.1-Yb^{II}	485	579	808

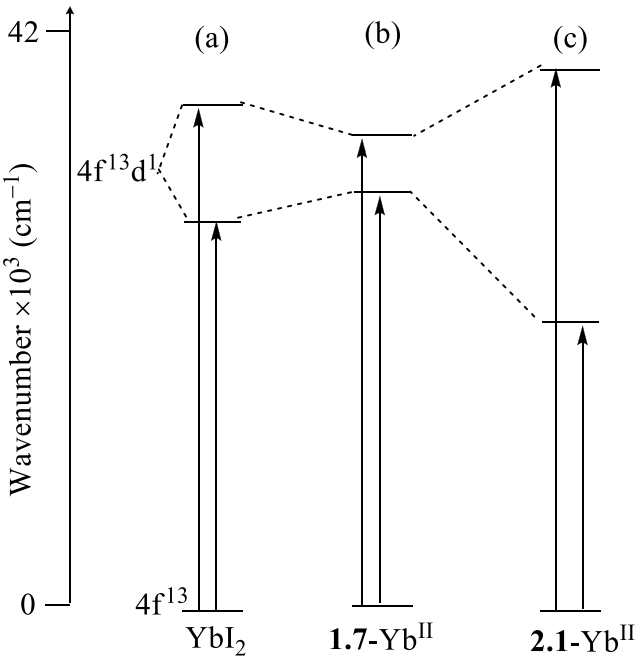

Figure 4.4. Schematic diagram of splitting of the excited state energy levels based on the maximum absorptions observed in methanol for (a) YbI_2, (b) **1.7**-Yb^{II}, and (c) **2.1**-Yb^{II}.

Two reasons likely contribute to the observed differences in absorptions. One reason for the shifts is the size match between metal ion and cryptand cavities. For example, the Yb^{II} ion (1.02 Å for coordination number 6)[70] that is smaller than the cavity in cryptand 4.1 (1.4 Å)[8] would not be expected to have strong metal-ligand interactions with this ligand because of a size mismatch. This expectation is supported by the absorption peaks of cryptates of Yb^{II} with cryptands **1.7**, **1.17**, and **3.1** that are clustered together, indicating the small Yb^{II} ion forms relatively weak bonds with cryptands **1.7**, **1.17**, and **3.1**. These weak interactions likely result from electrostatic interactions. With cryptand **2.1**, Yb^{II} displayed an absorption 100 nm away from that of the uncomplexed ion. This large shift is highly unlikely if the interactions within the complex are purely electrostatic; therefore, the second potential reason that governs the shift in absorption spectra is the presence of orbital interactions between metal and ligand.

Emission Spectra. To further analyze the influence of ligand structure on the electronics of these metal complexes, emission spectra were recorded for **1.7**, **1.17**, **3.1**, and **2.1** with YbI_2

(**Figure 4.5**). Similar to the absorption spectra, emission wavelengths and intensities relate to the coordination environment of metal ions.[80]

Emissions of Yb^{II}-containing complexes occurred in the range of 410 to 660 nm. Uncomplexed YbI_2 displayed a broad peak from 525 to 660 nm (λ_{max} = 579 nm). Cryptate **1.7**-Yb^{II} displayed a broad emission between 400 and 550 nm (λ_{max} = 471 nm) that was 3.8× more intense than the emission peak of YbI_2. Complexes of ligands **1.17** and **3.1** with Yb^{II} displayed broad emissions between 410 and 550 nm with maxima that were shifted 11 nm higher in energy relative to **1.7**-Yb^{II}. Complex **2.1**-Yb^{II} displayed a broad, low intensity peak in the same wavelength range as YbI_2. Differences in the emission spectra of YbI_2 and Yb^{II}-containing cryptates of **1.7**, **1.17**, **3.1**, and **2.1** correlate with the ligand structure. For example, complex **1.7**-Yb^{II} displayed stronger emissions than Yb^{II}-containing cryptates of **1.17** and **3.1**. We suspected that this difference could be due to either the presence of coordinated solvent or aromatic ring in **3.1** and **2.1**. To investigate these possibilities, the conductivity of solutions of Yb^{II}-containing complexes of **1.7**, **1.17**, and **3.1** (130 ± 3, 121 ± 5, and 137 ± 2 S cm^2 mol^{-1}, respectively) in methanol were measured. Conductivity is a measure of the number of ions present in a solution. By comparing the measured conductivities to reported conductivities under the similar conditions, the charge number of a compound can be determined. Molar conductivities measured for Yb^{II}-containing cryptates of **1.7**, **1.17**, and **3.1** revealed 2:1 dissociations in solution for all three complexes.[116] Therefore, interactions with solvent are likely similar in Yb^{II}-contaning complexes of **1.7**, **1.17**, and **3.1** suggesting that the lower emission intensities observed for Yb^{II}-containing cryptates of **1.17** and **3.1** are likely due to quenching by the aromatic moieties. Similar phenomena were reported for similar-type of Eu^{II}-containing complexes.[86] Another difference in emission spectra is complex **2.1**-Yb^{II} displayed a weak emission at a longer wavelength than Yb^{II}-containing cryptates of **1.7**, **1.17**, and **3.1** (**Table 4.2**). Complex **2.1**-Yb^{II}

displayed emissions at longer wavelengths relative to ether-rich cryptates of Yb^{II}. This shift is likely due to the strong-field effect of the amine-rich ligand **2.1**.[113] Cryptand **2.1** displayed bright emission with Eu^{II} ion in aqueous solution at high pH, whereas complex **2.1**-Yb^{II} only displayed weak emissions likely due to quenching from NH oscillators.[113]

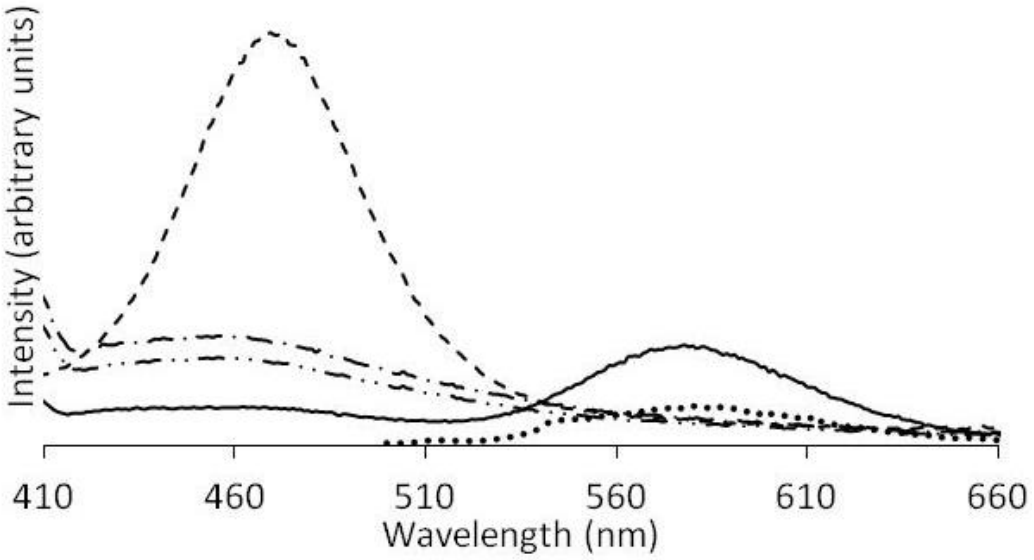

Figure 4.5. Emission spectra of solvated YbI_2 and Yb^{II}-containing complexes (2.0 mM) in methanol: YbI_2 (—), **1.7**-Yb^{II} (- -), **1.17**-Yb^{II} (— · —), **3.1**-Yb^{II} (— · · —), and **2.1**-Yb^{II} (• •).

Cyclic Voltammetry. Coordination environment not only influences photochemical properties but also redox properties.[9,8] Oxidation and reduction in a metal complex are associated with the energy difference between the highest occupied molecular orbital and the lowest unoccupied molecular orbital; therefore, a change in ligand structure that influences the energy of either of these frontier orbitals can be probed using the redox potentials of a metal complex.[120] For complexes synthesized using cryptands **1.7**, **1.17**, **3.1**, and **2.1** with YbI_2, redox potentials were measured using cyclic voltammetry.

YbI_2 displayed a half wave potential ($E_{1/2}$) at –1.39 ± 0.03 V (**Table 4.6** and **Figure 4.6**), Complexation of Yb^{II} with cryptands **1.7**, **1.17**, and **3.1** shifted the half wave potentials in the positive direction by 0.16 ± 0.07, 0.41 ± 0.05, and 0.42 ± 0.06 V, respectively, indicating

increased oxidative stability compared to the solvated ion.[8,112] In the case of complex **2.1**-Yb^{II}, the half wave potential was shifted in the negative direction by 0.13 ± 0.09 from the solvated ion indicating oxidative destabilization compared to the solvated ion.[121] Cyclic voltamograms of complexes of Yb^{II} with cryptands **1.7**, **1.17**, **3.1**, and **2.1** displayed quasi-reversible behaviors as evident from the differences observed between oxidative and reductive peak potentials.

Table 4.6. $E_{1/2}$ potentials vs $Ag/AgNO_3$

Complex	$E_{1/2}$ (V)	E_{ox}–E_{red} (V)
YbI_2	–1.39 ± 0.03	0.15
1.7-Yb^{II}	–1.23 ± 0.06	0.35
1.17-Yb^{II}	–0.98 ± 0.04	0.12
3.1-Yb^{II}	–0.97 ± 0.05	0.14
2.1-Yb^{II}	–1.52 ± 0.08	0.16

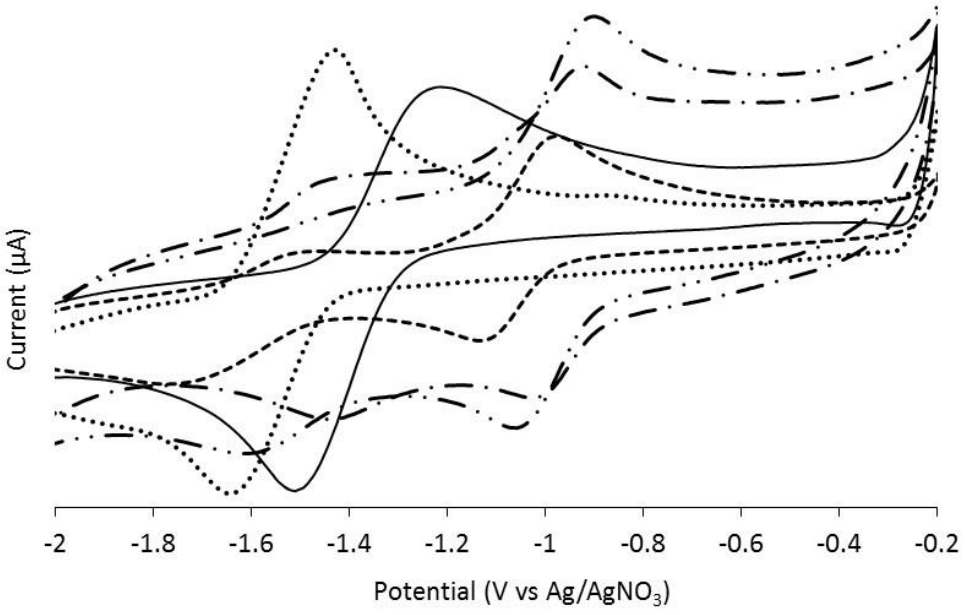

Figure 4.6. Cyclic voltamograms of YbI_2 (—), **1.7**-Yb^{II} (- -), **1.17**-Yb^{II} (— · —), **3.1**-Yb^{II} (— · · —), and **2.1**-Yb^{II} (• •) in methanol.

Based on the difference between $E_{1/2}$ potentials of the four Yb^{II}-containing cryptates, ether-rich cryptates **1.17**-Yb^{II} and **3.1**-Yb^{II} displayed higher oxidative stabilization of the +2 oxidation state of Yb relative to **1.7**-Yb^{II}. This higher oxidative stabilization imposed by the cryptands **1.17** and **3.1** relative to **1.7** is consistent with the oxidative stabilization reported with other Ln^{II} ions and cryptands **1.7**, **1.17**, and **3.1**.[72] Amine-rich cryptand **2.1**, however, displayed oxidative destabilization of the +2 oxidation state of Yb, likely due to the strong basicity of the amine-rich ligand.

Photochemical and redox properties have been discussed with respect to the structural properties of the complexes, ligand environment, and strength of the metal–ligand interactions. Although these factors contribute to the changes in properties, the differences in the properties of these complexes are also governed by changes in electronic factors. To understand the electronic properties, electronic paramagnetic resonance spectroscopy and computational analysis were used.

4.4 Conclusions

The absorption, emission, and redox properties of Yb^{II}-containing cryptates are influenced by coordination environment. Yb^{II} ions displayed greater sensitivity to the amine-rich cryptand than to ether-rich cryptands. The amine-rich Yb^{II}-containing cryptate displayed strong metal-ligand interactions that were evident from the shifts observed in absorption spectra and redox potentials, suggesting the presence of metal-ligand orbital interactions. The presence of orbital interactions involving the Yb^{II} ion are contrary to Yb^{II} being one of the six Ln^{II} ions that do not show covalent character in bonding. This study provides the basis to understand how Ln^{II} ions beyond Eu^{II} interact with different cryptand-type ligands and enables the optimization of properties of Ln^{II}-containing cryptates that are potentially useful in applications including optoelectronics, catalysis, reductions, and imaging.

CHAPTER 5: CONCLUSIONS AND FUTURE DIRECTIONS

Conclusions

Studies of the influence of coordination environment on the photochemical and redox properties and electronic structures of Ln^{II} ions are vital in developing materials that are useful as reducing agents, catalysts, optoelectronic materials, and contrast agents. Although many reports discuss the influence of ligand structure on redox and photochemical properties and electronic structures of Ln^{II} ions,[5,7,10,11] studies of the influence of cryptand-type ligand structures on Ln^{II}-ligand interactions based on a combination of solid- and solution-phase characterization have not been reported. This thesis describes research focused on understanding the interactions between Ln^{II} ions and cryptand-type ligands with respect to ligand structure and redox and photochemical properties and electronic structures of the resulting metal complexes.

A variety of data was used to characterize the influence of ligand structure on metal complexes including X-ray crystal structures, elemental analysis, absorption and emission spectra, quantum yield calculations, cyclic voltametry, and conductivity. This data suggested that photochemical and redox properties and electronic structure can be modulated by changing cryptand coordination environment. In Chapter 2, the first example of bright-yellow emitting Eu^{II}-containing cryptate in aqueous media was described with solid- and solution-phase characterization. The quantum yield of the emission was calculated to be 26%, which is the highest reported quantum yield for a Eu^{II}-containing complex in aqueous media. In Chapter 2, the yellow-emission was discussed with respect to the influence of amine-rich coordination environment and the strong-ligand field effect shifting the emission wavelength from blue that is the usual emission range for Eu^{II}-containing complexes to yellow region in the visible spectrum. This study concludes that strong field ligands shift the emissions of Eu^{II} ion to lower

wavelengths and the exclusion of coordinated water from the Eu^{II} ion results in intense luminescence.

Chapter 3 was a large expansion of the study in Chapter 2. A series of four ligands was studied with Eu^{II} ion. This study of the resulting four complexes demonstrated that strong field amine-rich ligands dramatically influence absorption, emission, redox, and electronic properties of Eu^{II} ion, and weak field ether-rich ligands influence properties minimally.

Chapter 4 described the use of the ligand series described in Chapter 3 with Yb^{II} ion to investigate the influence of ligand structure on coordinating properties of other Ln^{II} ions other than Eu^{II} ion. The trends observed in properties of Yb^{II}-containing complexes are similar to the trends observed with corresponding complexes of Eu^{II} ion, except that the amine-rich cryptand formed complex with Yb^{II} ion that displayed 8-coordinate bicapped trigonal antiprism geometry, whereas all the other Yb^{II}- and Eu^{II}-containing metal complexes formed 9-coordinate staggered or eclipsed hula-hoop geometries. Based on the changes in physicochemical properties of Both Eu^{II}- and Yb^{II}-containing cryptates suggest some degree of covalent character in Ln^{II}-cryptand interactions. Structural and electronic factors including size of the metal ion, cavity size of the cryptand, energy of the $4f^{n-1}5d^1$ state, type of the coordinating atoms determine the strength of the Ln^{II}-cryptand interactions as opposed to only the size match between the metal ion and ligand cavity.

Future Directions

As evident from the results described in this thesis in addition to the work of others, [5,7,10,11] variations in coordination environment enable tunability of the photochemical and redox properties and the electronic structure of Ln^{II} ions. To use these properties in practical applications including optoelectronic materials, sensors, catalysis, functional group reductions

and contrast agents, focus must be drawn to these individual applications, because each of these applications needs optimization of a different set of properties or combination of properties.

Optoelectronics and sensors are mainly solid-state applications. Although this thesis does not describe solid-state photochemical properties, the fundamentals that were explained through various characterization methods lay a foundation that can be used in solid-state applications as well. The Eu^{II}-containing cryptate described in Chapter 2 that emits bright yellow light has the potential to be used in the optoelectronic materials. For that use, the complex would need to be placed in the solid-state, for example by attaching to a polymer support that enables the use of the metal complex in devices. One of the limitations would be the air sensitivity. If the device is engineered to avoid air, materials synthesized with this complex could have a potential to be used in optoelectronic devices.

Another potential avenue would be to tune the ligand environment to obtain emissions at much longer wavelengths (red to near-IR), because emissions at longer wavelengths with high quantum yields are one of the demanding requirements for optical imaging in living organisms. As discussed in Chapter 3, ligands with stronger ligand fields than cryptand **2.1** including bipyridines, carboxylic acids, and phosphines could be investigated to see if modified ligand field strengths alone will push the emission to red to near-IR region.

Catalysis and reducing agents for functional group transformations will be two of the most demanding areas in which the results of this thesis could be useful. Ln^{II}-based catalysis and reducing agents are two overlapping areas. Based on the redox properties described in Chapters 3 and 4, strong field ligands generate stronger reducing agents and weak field ligands generate weak reducing agents in organic media; therefore, judicious selection of coordinating ligands will generate selective reducing agents for different functional groups. Furthermore, many attempts have been made to catalyze reduction reactions where the reducing agent is a Ln^{II}-

containing species.[25,26] One limitation to make these reduction reactions catalytic is the regeneration of the Ln^{II} species. For this purpose, large excesses of reducing agents are typically required. The addition of excess reducing agent often complicates the reaction. To address these limitations, ligand-based electron transfer processes could be developed. When the Ln^{II} ion is oxidized after the reduction of the functional group, the oxidized metal could be converted back to the +2 state through a ligand-based electron transfer, or hydrogen abstraction from the ligand, and the oxidized ligand could then be regenerated with hydrogen gas or light.

APPENDIX A

Crystallography Data for Complex 2.1-Eu^{II}

Table A1. Data collection and structure refinement for **2.1**-Eu^{II}

Theta range for data collection	1.43 to 40.81°	
Index ranges	–29<=h<=27, –28<=k<=28, –27<=l<=29	
Reflections collected	234315	
Independent reflections	14643 [R(int) = 0.0417]	
Coverage of independent reflections	96.2%	
Absorption correction	multi-scan	
Refinement method	Full-matrix least-squares on F^2	
Refinement program	SHELXL-2013 (Sheldrick, 2013)	
Function minimized	$\Sigma\, w(F_o^2 - F_c^2)^2$	
Data / restraints / parameters	14643 / 2 / 275	
Goodness-of-fit on F^2	1.244	
Δ/σ_{max}	5.787	
Final R indices	12671 data; I>2σ(I)	R1 = 0.0543, wR2 = 0.1515
	all data	R1 = 0.0650, wR2 = 0.1601
Weighting scheme	$w=1/[\sigma^2(F_o^2)+(0.1000P)^2+0.0321P]$ where $P=(F_o^2+2F_c^2)/3$	
Absolute structure parameter	0.2(0)	
Largest diff. peak and hole	8.109 and –2.358 eÅ^{-3}	
R.M.S. deviation from mean	0.237 eÅ^{-3}	

Table A2. Atomic coordinates and equivalent isotropic atomic displacement parameters (Å^2) for **2.1**-Eu^{II}

	x/a	y/b	z/c	U(eq)
Eu1	0.00821(3)	0.33330(6)	0.2554(2)	0.00872(6)
Cl01	0.7964(5)	0.2428(5)	0.5242(4)	0.0752(18)
Cl1	0.18872(18)	0.3337(4)	0.2547(3)	0.01811(18)
C31	0.9994(13)	0.2059(11)	0.4459(9)	0.024(3)
O1S	0.8861(6)	0.4629(6)	0.4838(4)	0.0080(13)
C30	0.1222(12)	0.4668(11)	0.4355(9)	0.028(3)
C22	0.0354(9)	0.2939(9)	0.0361(8)	0.018(2)
N6B	0.0838(8)	0.3617(8)	0.0978(6)	0.013(2)
C28	0.1080(14)	0.5752(14)	0.3391(10)	0.034(4)
C27	0.9420(10)	0.4981(10)	0.1970(8)	0.022(3)
C24	0.8020(9)	0.3396(9)	0.2100(6)	0.025(3)
C25	0.8032(12)	0.3329(11)	0.3034(8)	0.018(4)
N3	0.8423(7)	0.2715(8)	0.3292(7)	0.018(2)
C23	0.7802(9)	0.1703(9)	0.3091(8)	0.016(2)
C2	0.9132(9)	0.0820(8)	0.2452(8)	0.019(2)

N8	0.9145(8)	0.1394(8)	0.3139(6)	0.0142(18)
C4B	0.8229(7)	0.1143(7)	0.3457(6)	0.0124(16)
C4	0.1740(8)	0.5307(8)	0.1320(7)	0.024(2)
C5	0.9732(10)	0.1339(10)	0.3791(9)	0.028(3)
C26	0.0457(12)	0.5592(14)	0.1693(10)	0.038(4)
N7	0.9084(11)	0.1826(9)	0.1333(9)	0.052(4)
C7	0.9909(11)	0.1991(12)	0.0747(8)	0.017(3)
C29	0.1264(11)	0.4611(13)	0.0673(9)	0.032(4)
C9	0.0765(11)	0.3781(11)	0.4737(9)	0.019(3)
N5	0.1105(9)	0.5219(10)	0.1983(8)	0.025(3)
C13	0.1652(9)	0.5867(10)	0.2573(9)	0.028(3)
N1	0.0636(5)	0.4820(6)	0.3747(5)	0.0120(14)
N15	0.0539(7)	0.3044(8)	0.4120(7)	0.024(2)
N2	0.9029(9)	0.3955(8)	0.1816(6)	0.020(2)
C18	0.8637(11)	0.0874(9)	0.1697(6)	0.018(2)
C1S	0.8863(7)	0.4233(8)	0.5255(6)	0.0115(19)

$U_{(eq)}$ is defined as one third of the trace of the orthogonalized U_{ij} tensor.

Table A3. Bond lengths (Å) for **2.1**-Eu^{II}

Eu1-N15	2.773(12)	Eu1-N6B	2.796(11)
Eu1-N5	2.846(14)	Eu1-N1	2.895(8)
Eu1-N8	2.921(10)	Eu1-N7	2.958(15)
Eu1-Cl1	2.9640(10)	C31-C5	1.51(2)
C31-N15	1.510(18)	C31-H31A	0.99
C31-H31B	0.99	O1S-C1S	0.944(9)
C30-C9	1.41(2)	C30-N1	1.489(17)
C30-H30A	0.99	C30-H30B	0.99
C22-N6B	1.417(18)	C22-C7	1.49(2)
C22-H22A	0.99	C22-H22B	0.99
N6B-C29	1.504(19)	C28-N1	1.45(2)
C28-C13	1.59(2)	C28-H28A	0.99
C28-H28B	0.99	C27-N2	1.496(18)
C27-C26	1.552(18)	C27-H27A	0.99
C27-H27B	0.99	C24-N2	1.513(18)
C24-C25	1.532(8)	C24-H24A	0.99
C24-H24B	0.99	C25-N3	1.504(18)
C25-H25A	0.99	C25-H25B	0.99
N3-C23	1.490(17)	C23-C4B	1.529(13)
C23-H23A	0.99	C23-H23B	0.99
C2-N8	1.461(15)	C2-C18	1.505(17)
C2-H2A	0.99	C2-H2B	0.99
N8-C4B	1.446(15)	N8-C5	1.471(19)
C4B-H4B1	0.99	C4B-H4B2	0.99
C4-N5	1.460(17)	C4-C29	1.46(2)
C4-H4A	0.99	C4-H4B	0.99
C5-H5A	0.99	C5-H5B	0.99

C26-N5	1.55(3)	C26-H26A	0.99
C26-H26B	0.99	N7-C18	1.479(18)
N7-C7	1.570(19)	C7-H7A	0.99
C7-H7B	0.99	C29-H29A	0.99
C29-H29B	0.99	C9-N15	1.473(19)
C9-H9A	0.99	C9-H9B	0.99
N5-C13	1.384(18)	C13-H13A	0.99
C13-H13B	0.99	C18-H18A	0.99
C18-H18B	0.99	C1S-H1S1	0.98

Table A4. Bond angles (°) for **2.1**-Eu^{II}

N3-Eu1-N2	67.66(15)	N3-Eu1-N15	80.3(3)
N2-Eu1-N15	139.3(3)	N3-Eu1-N6B	139.7(4)
N2-Eu1-N6B	80.8(4)	N15-Eu1-N6B	137.96(14)
N3-Eu1-N5	119.8(4)	N2-Eu1-N5	65.3(4)
N15-Eu1-N5	115.2(3)	N6B-Eu1-N5	62.9(4)
N3-Eu1-N1	81.2(3)	N2-Eu1-N1	88.4(3)
N15-Eu1-N1	61.7(3)	N6B-Eu1-N1	123.6(3)
N5-Eu1-N1	62.4(3)	N3-Eu1-N8	63.7(3)
N2-Eu1-N8	118.2(3)	N15-Eu1-N8	63.4(3)
N6B-Eu1-N8	115.6(3)	N5-Eu1-N8	176.32(15)
N1-Eu1-N8	118.2(3)	N3-Eu1-N7	87.3(3)
N2-Eu1-N7	79.8(4)	N15-Eu1-N7	124.3(4)
N6B-Eu1-N7	62.1(3)	N5-Eu1-N7	118.0(4)
N1-Eu1-N7	166.0(2)	N8-Eu1-N7	62.5(3)
N3-Eu1-Cl1	146.3(3)	N2-Eu1-Cl1	146.0(3)
N15-Eu1-Cl1	69.4(2)	N6B-Eu1-Cl1	68.6(3)
N5-Eu1-Cl1	87.2(3)	N1-Eu1-Cl1	96.27(18)
N8-Eu1-Cl1	89.1(2)	N7-Eu1-Cl1	97.7(3)
C5-C31-N15	111.2(11)	C5-C31-H31A	108.4
N15-C31-H31A	108.9	C5-C31-H31B	109.7
N15-C31-H31B	110.7	H31A-C31-H31B	108.0
C9-C30-N1	114.5(13)	C9-C30-H30A	108.8
N1-C30-H30A	109.0	C9-C30-H30B	108.6
N1-C30-H30B	108.0	H30A-C30-H30B	107.7
N6B-C22-C7	108.1(11)	N6B-C22-H22A	110.3
C7-C22-H22A	110.1	N6B-C22-H22B	110.2
C7-C22-H22B	109.7	H22A-C22-H22B	108.4
C22-N6B-C29	113.1(11)	C22-N6B-Eu1	119.7(8)
C29-N6B-Eu1	114.4(9)	N1-C28-C13	114.8(15)
N1-C28-H28A	109.2	C13-C28-H28A	109.9
N1-C28-H28B	107.3	C13-C28-H28B	107.4
H28A-C28-H28B	107.9	N2-C27-C26	113.2(13)
N2-C27-H27A	109.0	C26-C27-H27A	107.4
N2-C27-H27B	110.1	C26-C27-H27B	109.2

H27A-C27-H27B	107.7	N2-C24-C25	107.4(14)
N2-C24-H24A	108.5	C25-C24-H24A	109.4
N2-C24-H24B	110.7	C25-C24-H24B	112.2
H24A-C24-H24B	108.4	N3-C25-C24	110.7(12)
N3-C25-H25A	111.0	C24-C25-H25A	109.5
N3-C25-H25B	109.4	C24-C25-H25B	107.8
H25A-C25-H25B	108.2	C23-N3-C25	113.8(11)
C23-N3-Eu1	108.9(8)	C25-N3-Eu1	108.4(8)
N3-C23-C4B	108.7(10)	N3-C23-H23A	110.1
C4B-C23-H23A	111.0	N3-C23-H23B	109.0
C4B-C23-H23B	109.7	H23A-C23-H23B	108.3
N8-C2-C18	115.1(10)	N8-C2-H2A	107.0
C18-C2-H2A	107.4	N8-C2-H2B	110.0
C18-C2-H2B	109.6	H2A-C2-H2B	107.3
C4B-N8-C2	114.6(10)	C4B-N8-C5	110.1(9)
C2-N8-C5	108.3(10)	C4B-N8-Eu1	109.6(6)
C2-N8-Eu1	106.5(6)	C5-N8-Eu1	107.5(8)
N8-C4B-C23	114.4(9)	N8-C4B-H4B1	110.0
C23-C4B-H4B1	109.7	N8-C4B-H4B2	107.0
C23-C4B-H4B2	107.8	H4B1-C4B-H4B2	107.6
N5-C4-C29	112.4(11)	N5-C4-H4A	107.8
C29-C4-H4A	108.9	N5-C4-H4B	110.9
C29-C4-H4B	108.7	H4A-C4-H4B	108.0
N8-C5-C31	114.4(12)	N8-C5-H5A	109.8
C31-C5-H5A	108.7	N8-C5-H5B	107.3
C31-C5-H5B	108.9	H5A-C5-H5B	107.4
N5-C26-C27	113.9(14)	N5-C26-H26A	106.8
C27-C26-H26A	107.2	N5-C26-H26B	111.1
C27-C26-H26B	110.0	H26A-C26-H26B	107.6
C18-N7-C7	110.9(12)	C18-N7-Eu1	112.9(9)
C7-N7-Eu1	101.4(9)	C22-C7-N7	111.6(12)
C22-C7-H7A	108.8	N7-C7-H7A	109.2
C22-C7-H7B	109.3	N7-C7-H7B	109.9
H7A-C7-H7B	107.9	C4-C29-N6B	112.7(11)
C4-C29-H29A	110.3	N6B-C29-H29A	109.7
C4-C29-H29B	108.5	N6B-C29-H29B	107.6
H29A-C29-H29B	107.8	C30-C9-N15	109.4(13)
C30-C9-H9A	109.7	N15-C9-H9A	109.5
C30-C9-H9B	110.3	N15-C9-H9B	109.7
H9A-C9-H9B	108.3	C13-N5-C4	106.4(11)
C13-N5-C26	102.7(13)	C4-N5-C26	109.5(12)
C13-N5-Eu1	114.4(9)	C4-N5-Eu1	110.8(9)
C26-N5-Eu1	112.6(9)	N5-C13-C28	112.1(12)
N5-C13-H13A	111.1	C28-C13-H13A	110.6
N5-C13-H13B	107.1	C28-C13-H13B	107.7
H13A-C13-H13B	108.1	C28-N1-C30	114.8(12)
C28-N1-Eu1	113.6(8)	C30-N1-Eu1	105.2(7)

C9-N15-C31	113.6(11)	C9-N15-Eu1	118.0(9)
C31-N15-Eu1	117.1(8)	C27-N2-C24	110.8(11)
C27-N2-Eu1	111.0(9)	C24-N2-Eu1	110.5(8)
N7-C18-C2	113.3(12)	N7-C18-H18A	108.6
C2-C18-H18A	107.9	N7-C18-H18B	109.6
C2-C18-H18B	109.9	H18A-C18-H18B	107.5
O1S-C1S-H1S1	109.5	O1S-C1S-H1S2	109.4
H1S1-C1S-H1S2	109.5	O1S-C1S-H1S3	109.5
H1S1-C1S-H1S3	109.5	H1S2-C1S-H1S3	109.5

Table A5. Anisotropic atomic displacement parameters ($Å^2$) for **2.1**-Eu^{II}

	U_{11}	U_{22}	U_{33}	U_{23}	U_{13}	U_{12}
Eu1	0.0085(3)	0.01013(8)	0.00802(10)	0.00019(13)	0.0001(6)	0.0051(3)
Cl01	0.082(4)	0.085(5)	0.071(3)	0.034(3)	0.028(3)	0.051(4)
Cl1	0.0118(11)	0.0245(4)	0.0203(4)	0.0016(8)	0.0029(14)	0.0107(11)
C31	0.034(8)	0.022(6)	0.023(5)	0.008(5)	0.014(5)	0.020(6)
O1S	0.008(3)	0.008(4)	0.008(3)	0.000(3)	0.000(3)	0.004(3)
C30	0.028(7)	0.026(6)	0.031(6)	-0.013(5)	-0.001(5)	0.015(5)
C22	0.022(4)	0.019(4)	0.020(4)	0.001(3)	-0.001(3)	0.015(3)
N6B	0.010(4)	0.013(5)	0.009(4)	-0.001(3)	0.001(3)	0.001(3)
C27	0.029(7)	0.023(6)	0.021(5)	-0.001(4)	0.006(5)	0.018(6)
C24	0.018(4)	0.036(7)	0.016(5)	-0.006(3)	0.006(3)	0.010(4)
C25	0.023(8)	0.018(8)	0.022(7)	0.007(5)	0.011(5)	0.016(7)
N3	0.011(4)	0.016(4)	0.028(5)	0.006(3)	0.007(3)	0.007(3)
C23	0.008(4)	0.015(6)	0.020(5)	0.006(4)	0.001(4)	0.003(4)
C2	0.020(5)	0.009(4)	0.027(6)	-0.003(3)	0.002(3)	0.006(3)
N8	0.016(5)	0.014(4)	0.014(4)	0.005(3)	0.001(3)	0.009(4)
C4B	0.011(3)	0.011(3)	0.013(3)	0.0025(19)	0.0023(19)	0.003(2)
C4	0.015(4)	0.018(5)	0.029(5)	-0.009(4)	0.011(3)	0.002(4)
C5	0.031(6)	0.020(6)	0.033(6)	0.008(5)	0.024(5)	0.012(5)
N7	0.081(9)	0.011(5)	0.054(8)	0.007(5)	0.046(6)	0.017(5)
C7	0.020(7)	0.023(8)	0.015(5)	-0.003(5)	0.003(5)	0.015(6)
C29	0.015(5)	0.061(9)	0.021(5)	0.026(5)	0.008(4)	0.020(6)
C9	0.027(7)	0.023(5)	0.015(5)	-0.001(4)	-0.005(4)	0.020(5)
N5	0.020(5)	0.022(6)	0.037(6)	-0.017(5)	-0.016(4)	0.012(5)
C13	0.016(5)	0.022(5)	0.032(5)	0.016(5)	-0.007(5)	-0.002(4)
N1	0.008(3)	0.013(3)	0.013(3)	-0.005(3)	0.000(2)	0.004(3)
N15	0.009(3)	0.034(5)	0.024(4)	-0.003(3)	0.001(3)	0.006(3)
N2	0.021(5)	0.018(5)	0.016(4)	-0.005(3)	0.007(4)	0.006(4)
C18	0.026(4)	0.009(3)	0.015(3)	-0.002(2)	0.003(2)	0.006(3)
C1S	0.009(3)	0.010(5)	0.014(4)	-0.002(4)	0.002(3)	0.004(4)

Table A6. Hydrogen atomic coordinates and isotropic atomic displacement parameters ($Å^2$) for **2.1**-Eu^{II}

	x/a	y/b	z/c	U(eq)
H31A	1.0378	0.1968	0.4875	0.029
H31B	0.9416	0.1971	0.4729	0.029
H30A	1.1791	0.4746	0.4075	0.033
H30B	1.1430	0.5159	0.4781	0.033
H22A	1.0797	0.2987	-0.0072	0.021
H22B	0.9867	0.3045	0.0109	0.021
H28A	1.1513	0.6206	0.3800	0.04
H28B	1.0589	0.5916	0.3273	0.04
H27A	0.9377	0.5080	0.2562	0.026
H27B	0.9031	0.5191	0.1676	0.026
H24A	0.7710	0.2760	0.1854	0.03
H24B	0.7670	0.3714	0.1932	0.03
H25A	0.8421	0.3965	0.3268	0.022
H25B	0.7385	0.3066	0.3248	0.022
H23A	0.7747	0.1617	0.2490	0.019
H23B	0.7167	0.1476	0.3319	0.019
H2A	0.8825	0.0156	0.2632	0.023
H2B	0.9788	0.1013	0.2305	0.023
H4B1	0.8278	0.1238	0.4058	0.015
H4B2	0.7796	0.0467	0.3353	0.015
H4A	1.2257	0.5231	0.1547	0.029
H4B	1.2020	0.5945	0.1082	0.029
H5A	1.0316	0.1415	0.3543	0.034
H5B	0.9393	0.0705	0.4039	0.034
H26A	1.0476	0.5628	0.1087	0.046
H26B	1.0704	0.6238	0.1905	0.046
H7A	1.0389	0.1927	0.1062	0.021
H7B	0.9665	0.1505	0.0314	0.021
H29A	1.1722	0.4713	0.0235	0.038
H29B	1.0764	0.4703	0.0433	0.038
H9A	1.0181	0.3680	0.5003	0.022
H9B	1.1177	0.3751	0.5164	0.022
H13A	1.1894	0.6509	0.2354	0.034
H13B	1.2198	0.5789	0.2700	0.034
H18A	0.8626	0.0429	0.1284	0.022
H18B	0.7978	0.0677	0.1838	0.022
H1S1	0.9443	0.4204	0.5222	0.017
H1S2	0.8321	0.3601	0.5186	0.017
H1S3	0.8827	0.4482	0.5790	0.017

Crystallographic Data for Complex 3.1-Eu^{II}

Table A7. Sample and crystal data for **3.1**-Eu^{II}

Chemical formula	$C_{22}H_{34}EuFI_2N_2O_6$	
Formula weight	847.27	
Temperature	100(2) K	
Wavelength	0.71073 Å	
Crystal system	monoclinic	
Space group	P 1 21/n 1	
Unit cell dimensions	a = 9.5571(5) Å	α = 90°
	b = 16.7769(9) Å	β = 102.917(3)°
	c = 18.0111(9) Å	γ = 90°
Volume	2814.8(3) $Å^3$	
Z	4	
Density (calculated)	1.999 g/cm^3	
Absorption coefficient	4.465 mm^{-1}	
F(000)	1624	

Table A8. Data collection and structure refinement for **3.1**-Eu^{II}

Theta range for data collection	1.68 to 33.11°	
Index ranges	–14<=h<=14, –25<=k<=25, –27<=l<=27	
Reflections collected	118124	
Independent reflections	10673 [R(int) = 0.0242]	
Coverage of independent reflections	99.7%	
Absorption correction	multi-scan	
Refinement method	Full-matrix least-squares on F^2	
Refinement program	SHELXL-2014/7 (Sheldrick, 2014)	
Function minimized	$\Sigma\, w(F_o^2 - F_c^2)^2$	
Data / restraints / parameters	10673 / 0 / 307	
Goodness-of-fit on F^2	1.083	
Δ/σ_{max}	0.002	
Final R indices	9700 data; I>2σ(I)	R1 = 0.0501, wR2 = 0.1230
	all data	R1 = 0.0555, wR2 = 0.1272
Weighting scheme	$w=1/[\sigma^2(F_o^2)+(0.0485P)^2+26.0150P]$ where $P=(F_o^2+2F_c^2)/3$	
Largest diff. peak and hole	4.670 and –4.298 $eÅ^{-3}$	
R.M.S. deviation from mean	0.221 $eÅ^{-3}$	

Table A9. Atomic coordinates and equivalent isotropic atomic displacement parameters ($Å^2$) for **3.1**-Eu^{II}

	x/a	y/b	z/c	U(eq)
Eu1	0.19489(2)	0.77218(2)	0.08026(2)	0.01805(5)
I1	0.88075(4)	0.80644(2)	0.97280(2)	0.03310(8)
I3	0.68863(5)	0.97766(2)	0.24008(2)	0.04147(11)
F1	0.3877(7)	0.3848(3)	0.9610(4)	0.084(2)
O1	0.2352(5)	0.6539(3)	0.9820(2)	0.0366(9)
O2	0.2504(6)	0.9234(3)	0.0604(3)	0.0444(10)
O3	0.1443(5)	0.8811(3)	0.1757(3)	0.0425(10)
O4	0.3550(4)	0.7121(3)	0.2072(2)	0.0296(7)
O5	0.4705(4)	0.7676(3)	0.0919(2)	0.0347(8)
O6	0.1045(5)	0.6144(3)	0.0858(2)	0.0372(9)
N1	0.3022(6)	0.8164(3)	0.9540(3)	0.0371(10)
N2	0.0546(5)	0.7235(4)	0.1947(3)	0.0376(11)
C1	0.2904(8)	0.6750(4)	0.9151(3)	0.0426(14)
C2	0.2483(7)	0.7596(4)	0.8942(3)	0.0413(13)
C3	0.2348(9)	0.8946(4)	0.9312(4)	0.0497(17)
C4	0.2725(10)	0.9565(4)	0.9920(5)	0.056(2)
C5	0.2509(12)	0.9812(4)	0.1190(5)	0.063(2)
C6	0.2499(11)	0.9395(5)	0.1914(5)	0.064(2)
C7	0.0764(9)	0.8628(5)	0.2372(4)	0.0547(19)
C8	0.9790(7)	0.7940(5)	0.2143(4)	0.0497(17)
C9	0.1523(7)	0.6897(5)	0.2627(3)	0.0489(17)
C10	0.2889(6)	0.6548(5)	0.2475(3)	0.0426(15)
C11	0.4907(5)	0.6825(4)	0.1980(3)	0.0347(11)
C12	0.5629(5)	0.7479(4)	0.1630(3)	0.0377(12)
C13	0.5295(7)	0.8294(5)	0.0530(4)	0.0468(16)
C14	0.4618(7)	0.8223(5)	0.9700(4)	0.0476(16)
C15	0.9462(6)	0.6635(4)	0.1570(4)	0.0373(12)
C16	0.0093(7)	0.5902(4)	0.1319(4)	0.0435(15)
C17	0.1742(6)	0.5545(3)	0.0544(3)	0.0350(12)
C18	0.1709(9)	0.4734(4)	0.0787(4)	0.0517(19)
C19	0.2397(11)	0.4175(4)	0.0494(5)	0.066(3)
C20	0.3166(10)	0.4405(4)	0.9943(5)	0.064(3)
C21	0.3192(8)	0.5191(4)	0.9686(4)	0.0472(16)
C22	0.2453(7)	0.5757(3)	0.0008(3)	0.0370(12)

$U_{(eq)}$ is defined as one third of the trace of the orthogonalized U_{ij} tensor.

Table A10. Bond lengths of **3.1**-Eu^{II}

Eu1-O5	2.596(4)	Eu1-O3	2.627(4)
Eu1-O2	2.633(4)	Eu1-O4	2.650(4)
Eu1-O1	2.742(4)	Eu1-O6	2.793(4)
Eu1-N1	2.796(4)	Eu1-N2	2.819(5)
Eu1-I1	3.2392(4)	F1-C20	1.371(10)

O1-C22	1.353(7)	O1-C1	1.463(8)
O2-C4	1.410(9)	O2-C5	1.432(9)
O3-C6	1.389(10)	O3-C7	1.435(8)
O4-C11	1.433(6)	O4-C10	1.434(7)
O5-C12	1.423(7)	O5-C13	1.436(8)
O6-C17	1.393(7)	O6-C16	1.422(8)
N1-C2	1.444(9)	N1-C3	1.478(9)
N1-C14	1.491(8)	N2-C8	1.470(9)
N2-C9	1.478(8)	N2-C15	1.495(8)
C1-C2	1.500(10)	C1-H1	0.99
C1-H34	0.99	C2-H32	0.99
C2-H33	0.99	C3-C4	1.493(12)
C3-H31	0.99	C3-H2	0.99
C4-H29	0.99	C4-H30	0.99
C5-C6	1.483(13)	C5-H3	0.99
C5-H28	0.99	C6-H6A	0.99
C6-H6B	0.99	C7-C8	1.483(12)
C7-H26	0.99	C7-H4	0.99
C8-H25	0.99	C8-H24	0.99
C9-C10	1.510(10)	C9-H15	0.99
C9-H16	0.99	C10-H14	0.99
C10-H13	0.99	C11-C12	1.508(9)
C11-H12	0.99	C11-H11	0.99
C12-H10	0.99	C12-H9	0.99
C13-C14	1.495(10)	C13-H8	0.99
C13-H7	0.99	C14-H5	0.99
C14-H6	0.99	C15-C16	1.484(10)
C15-H23	0.99	C15-H22	0.99
C16-H21	0.99	C16-H20	0.99
C17-C22	1.347(10)	C17-C18	1.432(9)
C18-C19	1.321(13)	C18-H19	0.95
C19-C20	1.413(15)	C19-H18	0.95
C20-C21	1.400(11)	C21-C22	1.386(9)
C21-H17	0.95		

Table A11. Bond angles (°) for **3.1-Eu^{II}**

O5-Eu1-O3	107.43(14)	O4-Eu1-O6	74.49(12)	C3-C4-H30	110.1
O3-Eu1-O2	59.38(16)	O5-Eu1-N1	61.56(15)	O2-C5-C6	109.3(6)
O3-Eu1-O4	81.65(15)	O2-Eu1-N1	60.79(16)	C6-C5-H3	109.8
O5-Eu1-O1	75.20(13)	O1-Eu1-N1	62.43(16)	C6-C5-H28	109.8
O2-Eu1-O1	123.22(15)	O5-Eu1-N2	124.88(13)	O3-C6-C5	107.5(7)
O5-Eu1-O6	106.58(14)	O2-Eu1-N2	121.45(17)	C5-C6-H6A	110.2
O2-Eu1-O6	172.51(15)	O1-Eu1-N2	114.86(16)	C5-C6-H6B	110.2
O1-Eu1-O6	55.00(14)	N1-Eu1-N2	172.94(15)	O3-C7-C8	108.4(5)
O3-Eu1-N1	120.15(17)	O3-Eu1-I1	89.19(11)	C8-C7-H26	110.0

O4-Eu1-N1	123.85(14)	O4-Eu1-I1	149.59(8)	C8-C7-H4	110.0
O6-Eu1-N1	116.94(15)	O6-Eu1-I1	86.37(9)	N2-C8-C7	112.4(6)
O3-Eu1-N2	62.35(17)	N2-Eu1-I1	87.69(10)	C7-C8-H25	109.1
O4-Eu1-N2	62.35(12)	C22-O1-Eu1	123.6(4)	C7-C8-H24	109.1
O6-Eu1-N2	59.87(16)	C4-O2-C5	113.6(5)	N2-C9-C10	114.2(5)
O5-Eu1-I1	147.31(9)	C5-O2-Eu1	121.3(4)	C10-C9-H15	108.7
O2-Eu1-I1	86.32(12)	C6-O3-Eu1	113.1(4)	C10-C9-H16	108.7
O1-Eu1-I1	89.31(9)	C11-O4-C10	109.8(5)	O4-C10-C9	109.2(6)
N1-Eu1-I1	85.78(11)	C10-O4-Eu1	117.2(3)	C9-C10-H14	109.8
C22-O1-C1	114.9(5)	C12-O5-Eu1	119.6(3)	C9-C10-H13	109.8
C1-O1-Eu1	119.0(4)	C17-O6-C16	117.2(5)	O4-C11-C12	107.8(5)
C4-O2-Eu1	124.9(4)	C16-O6-Eu1	122.3(4)	C12-C11-H12	110.1
C6-O3-C7	115.3(6)	C2-N1-C14	111.5(5)	C12-C11-H11	110.1
C7-O3-Eu1	122.5(4)	C2-N1-Eu1	107.3(4)	O5-C12-C11	107.2(4)
C11-O4-Eu1	113.3(3)	C14-N1-Eu1	113.9(4)	C11-C12-H10	110.3
C12-O5-C13	112.0(5)	C8-N2-C15	108.8(5)	C11-C12-H9	110.3
C13-O5-Eu1	116.2(4)	C8-N2-Eu1	106.4(4)	O5-C13-C14	107.4(5)
C17-O6-Eu1	119.3(4)	C15-N2-Eu1	104.9(3)	C14-C13-H8	110.2
C2-N1-C3	108.5(5)	O1-C1-H1	110.1	C14-C13-H7	110.2
C3-N1-C14	111.0(6)	O1-C1-H34	110.1	N1-C14-C13	113.3(5)
C3-N1-Eu1	104.2(3)	H1-C1-H34	108.4	C13-C14-H5	108.9
C8-N2-C9	111.3(6)	N1-C2-H32	108.7	C13-C14-H6	108.9
C9-N2-C15	111.3(5)	N1-C2-H33	108.7	C16-C15-N2	114.1(5)
C9-N2-Eu1	113.7(3)	H32-C2-H33	107.6	N2-C15-H23	108.7
O1-C1-C2	108.0(5)	N1-C3-H31	108.9	N2-C15-H22	108.7
C2-C1-H1	110.1	N1-C3-H2	108.9	O6-C16-C15	107.3(5)
C2-C1-H34	110.1	H31-C3-H2	107.7	C15-C16-H21	110.3
N1-C2-C1	114.0(5)	O2-C4-H29	110.1	C15-C16-H20	110.3
C1-C2-H32	108.7	O2-C4-H30	110.1	C22-C17-O6	117.6(5)
O5-Eu1-O2	78.92(15)	C1-C2-H33	108.7	H29-C4-H30	108.4
O5-Eu1-O4	62.57(12)	N1-C3-C4	113.3(6)	O2-C5-H3	109.8
O2-Eu1-O4	112.86(15)	C4-C3-H31	108.9	O2-C5-H28	109.8
O3-Eu1-O1	176.89(14)	C4-C3-H2	108.9	H3-C5-H28	108.3
O4-Eu1-O1	98.32(12)	O2-C4-C3	107.9(5)	O3-C6-H6A	110.2
O3-Eu1-O6	122.17(15)	C3-C4-H29	110.1	O3-C6-H6B	110.2
H6A-C6-H6B	108.5	O4-C11-H12	110.1	C16-C15-H22	108.7
O3-C7-H26	110.0	O4-C11-H11	110.1	H23-C15-H22	107.6
O3-C7-H4	110.0	H12-C11-H11	108.5	O6-C16-H21	110.3
H26-C7-H4	108.4	O5-C12-H10	110.3	O6-C16-H20	110.3
N2-C8-H25	109.1	O5-C12-H9	110.3	C18-C19-C20	118.1(7)
N2-C8-H24	109.1	H10-C12-H9	108.5	C20-C19-H18	121.0
H25-C8-H24	107.9	O5-C13-H8	110.2	F1-C20-C19	120.5(8)
N2-C9-H15	108.7	O5-C13-H7	110.2	O6-C17-C18	121.1(7)
N2-C9-H16	108.7	H8-C13-H7	108.5	C19-C18-H19	119.9
H15-C9-H16	107.6	N1-C14-H5	108.9	C21-C20-C19	122.7(8)
O4-C10-H14	109.8	N1-C14-H6	108.9	C22-C21-H17	121.4
O4-C10-H13	109.8	H5-C14-H6	107.7	C17-C22-O1	114.6(5)

H14-C10-H13	108.3	C16-C15-H23	108.7	O1-C22-C21	125.1(7)
				C22-C21-C20	117.3(8)

Table A12. Hydrogen atomic coordinates and isotropic atomic displacement parameters ($Å^2$) for **3.1**-Eu^{II}

	x/a	**y/b**	**z/c**	**U(eq)**
H1	0.2493	0.6391	-0.1279	0.051
H34	0.3962	0.6696	-0.0734	0.051
H32	0.2842	0.7744	-0.1514	0.05
H33	0.1422	0.7631	-0.1195	0.05
H31	0.1292	0.8879	-0.0822	0.06
H2	0.2652	0.9134	-0.1148	0.06
H29	0.3741	0.9727	-0.0018	0.067
H30	0.2112	1.0042	-0.0219	0.067
H3	0.1653	1.0158	0.1046	0.076
H28	0.3376	1.0151	0.1253	0.076
H6A	0.3447	0.9149	0.2123	0.077
H6B	0.2288	0.9776	0.2294	0.077
H26	0.0213	0.9095	0.2484	0.066
H4	0.1499	0.8495	0.2836	0.066
H25	-0.0675	0.7804	0.2565	0.06
H24	-0.0974	0.8093	0.1697	0.06
H15	0.1006	0.6475	0.2842	0.059
H16	0.1778	0.7321	0.3016	0.059
H14	0.3554	0.6409	0.2963	0.051
H13	0.2668	0.6056	0.2168	0.051
H12	0.4764	0.6350	0.1645	0.042
H11	0.5511	0.6669	0.2481	0.042
H10	0.5787	0.7951	0.1968	0.045
H9	0.6570	0.7295	0.1553	0.045
H8	0.6350	0.8233	0.0616	0.056
H7	0.5086	0.8824	0.0722	0.056
H5	0.4887	0.8693	-0.0569	0.057
H6	0.5003	0.7743	-0.0505	0.057
H23	-0.1140	0.6484	0.1929	0.045
H22	-0.1173	0.6886	0.1121	0.045
H21	0.0621	0.5599	0.1767	0.052
H20	-0.0673	0.5557	0.1024	0.052
H19	0.1190	0.4597	0.1162	0.062
H18	0.2375	0.3635	0.0648	0.079
H17	0.3697	0.5331	-0.0693	0.057

Crystallographic Data for Complex 2.1-Eu^{II}

Table A13. Sample and crystal data for **2.1**-Eu^{II}

Chemical formula	$C_{18}H_{48}EuI_2N_8$	
Formula weight	782.40	
Temperature	100(2) K	
Wavelength	0.71073 Å	
Crystal system	orthorhombic	
Space group	P c a 21	
Unit cell dimensions	a = 15.770(2) Å	α = 90°
	b = 12.1249(19) Å	β = 90°
	c = 13.749(2) Å	γ = 90°
Volume	2628.9(7) $Å^3$	
Z	4	
Density (calculated)	1.977 g/cm^3	
Absorption coefficient	4.755 mm^{-1}	
F(000)	1524	

Table A14. Data collection and structure refinement for **2.1**-Eu^{II}

Theta range for data collection	1.68 to 36.32°	
Index ranges	–26<=h<=26, –20<=k<=20, –22<=l<=22	
Reflections collected	128327	
Independent reflections	12756 [R(int) = 0.0389]	
Coverage of independent reflections	100.0%	
Absorption correction	multi-scan	
Refinement method	Full-matrix least-squares on F^2	
Refinement program	SHELXL-2014/7 (Sheldrick, 2014)	
Function minimized	$\Sigma\, w(F_o^2 - F_c^2)^2$	
Data / restraints / parameters	12756 / 1 / 286	
Goodness-of-fit on F^2	1.049	
Δ/σ_{max}	0.002	
Final R indices	12570 data; I>2σ(I)	R1 = 0.0179, wR2 = 0.0468
	all data	R1 = 0.0183, wR2 = 0.0470
Weighting scheme	$w=1/[\sigma^2(F_o^2)+(0.0257P)^2+1.3737P]$ where $P=(F_o^2+2F_c^2)/3$	
Absolute structure parameter	0.3(0)	
Largest diff. peak and hole	1.097 and -1.073 $eÅ^{-3}$	
R.M.S. deviation from mean	0.111 $eÅ^{-3}$	

Table A15. Atomic coordinates and equivalent isotropic atomic displacement parameters ($Å^2$) for **2.1**-Eu^{II}

	x/a	y/b	z/c	U(eq)
Eu1	0.00309(2)	0.24345(2)	0.61737(2)	0.00845(2)
I1	0.92671(2)	0.96163(2)	0.63355(2)	0.01469(3)
I11E	0.13695(2)	0.47318(2)	0.87646(2)	0.01402(3)
N1	0.98395(13)	0.46965(16)	0.60229(16)	0.0123(3)
N2	0.14618(12)	0.36598(17)	0.61460(17)	0.0125(3)
N3	0.14242(13)	0.15472(19)	0.50401(17)	0.0134(3)
N4	0.98494(18)	0.25247(19)	0.4164(2)	0.0139(4)
N5	0.84020(13)	0.20867(19)	0.54095(16)	0.0134(3)
N6	0.85731(12)	0.34539(18)	0.71613(16)	0.0124(3)
N7	0.00145(13)	0.2352(2)	0.8165(2)	0.0129(4)
N8	0.11298(13)	0.09785(18)	0.70691(17)	0.0138(3)
C1	0.06310(17)	0.5323(2)	0.5886(2)	0.0160(4)
C2	0.13134(16)	0.4580(2)	0.5472(2)	0.0143(4)
C3	0.22398(14)	0.3036(2)	0.59433(18)	0.0150(4)
C4	0.21643(15)	0.2301(2)	0.50485(19)	0.0152(4)
C5	0.11431(16)	0.1375(2)	0.40242(19)	0.0169(4)
C6	0.06396(17)	0.2343(2)	0.3619(2)	0.0171(4)
C7	0.91833(16)	0.1718(2)	0.3901(2)	0.0164(4)
C8	0.83428(16)	0.2048(2)	0.43453(19)	0.0160(4)
C9	0.76640(16)	0.2611(2)	0.5861(2)	0.0162(4)
C10	0.78055(15)	0.2799(2)	0.6941(2)	0.0165(4)
C11	0.87169(16)	0.3455(2)	0.82260(19)	0.0151(4)
C12	0.91594(16)	0.2419(2)	0.8582(2)	0.0152(4)
C13	0.04984(16)	0.1455(2)	0.8623(2)	0.0181(4)
C14	0.13198(16)	0.1238(2)	0.8084(2)	0.0163(4)
C15	0.18431(16)	0.0497(2)	0.6536(2)	0.0178(5)
C16	0.16500(17)	0.0465(2)	0.5453(2)	0.0174(4)
C17	0.84581(16)	0.4603(2)	0.6828(2)	0.0152(4)
C18	0.92847(16)	0.5226(2)	0.6744(2)	0.0150(4)

$U_{(eq)}$ is defined as one third of the trace of the orthogonalized U_{ij} tensor.

Table A16. Bond lengths (Å) for **2.1**-Eu^{II}

Eu1-N2	2.7020(19)	Eu1-N7	2.740(3)
Eu1-N8	2.763(2)	Eu1-N1	2.767(2)
Eu1-N4	2.780(3)	Eu1-N5	2.807(2)
Eu1-N3	2.901(2)	Eu1-N6	2.942(2)
Eu1-I1	3.6299(5)	N1-C18	1.471(3)
N1-C1	1.473(3)	N1-H1N	0.74(5)
N2-C3	1.468(3)	N2-C2	1.468(3)
N2-H2N	0.77(4)	N3-C16	1.473(4)
N3-C5	1.480(3)	N3-C4	1.483(3)
N4-C6	1.471(4)	N4-C7	1.480(4)

N4-H4N	0.86(4)	N5-C9	1.464(3)
N5-C8	1.467(3)	N5-H5N	0.75(4)
N6-C17	1.478(3)	N6-C10	1.480(3)
N6-C11	1.481(3)	N7-C12	1.468(3)
N7-C13	1.470(4)	N7-H7N	0.95(4)
N8-C14	1.461(4)	N8-C15	1.464(3)
N8-H8M	0.77(4)	C1-C2	1.515(4)
C1-H47	0.99	C1-H46	0.99
C2-H44	0.99	C2-H45	0.99
C3-C4	1.524(4)	C3-H42	0.99
C3-H41	0.99	C4-H39	0.99
C4-H40	0.99	C5-C6	1.522(4)
C5-H38	0.99	C5-H37	0.99
C6-H36	0.99	C6-H35	0.99
C7-C8	1.514(4)	C7-H33	0.99
C7-H32	0.99	C8-H30	0.99
C8-H31	0.99	C9-C10	1.519(4)
C9-H27	0.99	C9-H26	0.99
C10-H25	0.99	C10-H24	0.99
C11-C12	1.518(4)	C11-H18	0.99
C11-H19	0.99	C12-H17	0.99
C12-H16	0.99	C13-C14	1.516(4)
C13-H15	0.99	C13-H14	0.99
C14-H12	0.99	C14-H13	0.99
C15-C16	1.521(4)	C15-H10	0.99
C15-H9	0.99	C16-H8	0.99
C16-H7	0.99	C17-C18	1.511(4)
C17-H22	0.99	C17-H23	0.99
C18-H20	0.99	C18-H21	0.99

Table A17. Bond angles (°) for **2.1**-Eu^{II}

N2-Eu1-N7	92.41(7)	N2-Eu1-N8	80.43(6)
N7-Eu1-N8	62.45(7)	N2-Eu1-N1	62.94(6)
N7-Eu1-N1	96.32(7)	N8-Eu1-N1	137.31(6)
N2-Eu1-N4	92.89(7)	N7-Eu1-N4	173.55(8)
N8-Eu1-N4	122.17(7)	N1-Eu1-N4	82.84(7)
N2-Eu1-N5	147.30(7)	N7-Eu1-N5	111.10(6)
N8-Eu1-N5	130.14(7)	N1-Eu1-N5	91.21(6)
N4-Eu1-N5	62.59(7)	N2-Eu1-N3	64.13(6)
N7-Eu1-N3	122.04(7)	N8-Eu1-N3	61.79(7)
N1-Eu1-N3	114.20(6)	N4-Eu1-N3	63.80(7)
N5-Eu1-N3	115.87(6)	N2-Eu1-N6	115.35(6)
N7-Eu1-N6	63.05(6)	N8-Eu1-N6	123.56(6)
N1-Eu1-N6	62.16(6)	N4-Eu1-N6	111.21(7)
N5-Eu1-N6	61.37(6)	N3-Eu1-N6	174.64(6)

N2-Eu1-I1	142.71(4)	N7-Eu1-I1	84.34(5)
N8-Eu1-I1	65.13(5)	N1-Eu1-I1	154.35(4)
N4-Eu1-I1	93.66(5)	N5-Eu1-I1	65.03(5)
N3-Eu1-I1	86.28(4)	N6-Eu1-I1	96.20(4)
C18-N1-C1	111.4(2)	C18-N1-Eu1	116.57(15)
C1-N1-Eu1	115.35(15)	C18-N1-H1N	113.(4)
C1-N1-H1N	103.(4)	Eu1-N1-H1N	96.(3)
C3-N2-C2	113.9(2)	C3-N2-Eu1	114.69(14)
C2-N2-Eu1	107.06(14)	C3-N2-H2N	108.(3)
C2-N2-H2N	109.(3)	Eu1-N2-H2N	104.(3)
C16-N3-C5	108.1(2)	C16-N3-C4	110.9(2)
C5-N3-C4	109.3(2)	C16-N3-Eu1	107.85(15)
C5-N3-Eu1	109.42(14)	C4-N3-Eu1	111.31(15)
C6-N4-C7	112.2(2)	C6-N4-Eu1	114.41(18)
C7-N4-Eu1	106.88(18)	C6-N4-H4N	105.(3)
C7-N4-H4N	113.(3)	Eu1-N4-H4N	105.(3)
C9-N5-C8	112.7(2)	C9-N5-Eu1	120.23(16)
C8-N5-Eu1	115.88(15)	C9-N5-H5N	105.(3)
C8-N5-H5N	109.(3)	Eu1-N5-H5N	90.(3)
C17-N6-C10	110.0(2)	C17-N6-C11	108.9(2)
C10-N6-C11	109.2(2)	C17-N6-Eu1	110.41(14)
C10-N6-Eu1	108.61(15)	C11-N6-Eu1	109.69(13)
C12-N7-C13	110.5(2)	C12-N7-Eu1	113.39(17)
C13-N7-Eu1	116.75(19)	C12-N7-H7N	108.(2)
C13-N7-H7N	105.(2)	Eu1-N7-H7N	101.(2)
C14-N8-C15	114.0(2)	C14-N8-Eu1	114.61(16)
C15-N8-Eu1	120.92(17)	C14-N8-H8M	116.(4)
C15-N8-H8M	101.(3)	Eu1-N8-H8M	86.(3)
N1-C1-C2	110.1(2)	N1-C1-H47	109.6
C2-C1-H47	109.6	N1-C1-H46	109.6
C2-C1-H46	109.6	H47-C1-H46	108.2
N2-C2-C1	109.2(2)	N2-C2-H44	109.8
C1-C2-H44	109.8	N2-C2-H45	109.8
C1-C2-H45	109.8	H44-C2-H45	108.3
N2-C3-C4	112.9(2)	N2-C3-H42	109.0
C4-C3-H42	109.0	N2-C3-H41	109.0
C4-C3-H41	109.0	H42-C3-H41	107.8
N3-C4-C3	115.4(2)	N3-C4-H39	108.4
C3-C4-H39	108.4	N3-C4-H40	108.4
C3-C4-H40	108.4	H39-C4-H40	107.5
N3-C5-C6	113.1(2)	N3-C5-H38	109.0
C6-C5-H38	109.0	N3-C5-H37	109.0
C6-C5-H37	109.0	H38-C5-H37	107.8
N4-C6-C5	111.8(2)	N4-C6-H36	109.3
C5-C6-H36	109.3	N4-C6-H35	109.3
C5-C6-H35	109.3	H36-C6-H35	107.9
N4-C7-C8	110.4(2)	N4-C7-H33	109.6

C8-C7-H33	109.6	N4-C7-H32	109.6
C8-C7-H32	109.6	H33-C7-H32	108.1
N5-C8-C7	110.8(2)	N5-C8-H30	109.5
C7-C8-H30	109.5	N5-C8-H31	109.5
C7-C8-H31	109.5	H30-C8-H31	108.1
N5-C9-C10	111.2(2)	N5-C9-H27	109.4
C10-C9-H27	109.4	N5-C9-H26	109.4
C10-C9-H26	109.4	H27-C9-H26	108.0
N6-C10-C9	113.6(2)	N6-C10-H25	108.8
C9-C10-H25	108.8	N6-C10-H24	108.8
C9-C10-H24	108.8	H25-C10-H24	107.7
N6-C11-C12	112.9(2)	N6-C11-H18	109.0
C12-C11-H18	109.0	N6-C11-H19	109.0
C12-C11-H19	109.0	H18-C11-H19	107.8
N7-C12-C11	110.0(2)	N7-C12-H17	109.7
C11-C12-H17	109.7	N7-C12-H16	109.7
C11-C12-H16	109.7	H17-C12-H16	108.2
N7-C13-C14	111.3(2)	N7-C13-H15	109.4
C14-C13-H15	109.4	N7-C13-H14	109.4
C14-C13-H14	109.4	H15-C13-H14	108.0
N8-C14-C13	109.2(2)	N8-C14-H12	109.8
C13-C14-H12	109.8	N8-C14-H13	109.8
C13-C14-H13	109.8	H12-C14-H13	108.3
N8-C15-C16	110.3(2)	N8-C15-H10	109.6
C16-C15-H10	109.6	N8-C15-H9	109.6
C16-C15-H9	109.6	H10-C15-H9	108.1
N3-C16-C15	113.7(2)	N3-C16-H8	108.8
C15-C16-H8	108.8	N3-C16-H7	108.8
C15-C16-H7	108.8	H8-C16-H7	107.7
N6-C17-C18	112.9(2)	N6-C17-H22	109.0
C18-C17-H22	109.0	N6-C17-H23	109.0
C18-C17-H23	109.0	H22-C17-H23	107.8
N1-C18-C17	110.2(2)	N1-C18-H20	109.6
C17-C18-H20	109.6	N1-C18-H21	109.6
C17-C18-H21	109.6	H20-C18-H21	108.1

Table A18. Anisotropic atomic displacement parameters ($Å^2$) for **2.1**-Eu^{II}

	U_{11}	U_{22}	U_{33}	U_{23}	U_{13}	U_{12}
Eu1	0.00801(4)	0.00806(4)	0.00929(4)	-0.00004(4)	-0.00052(3)	0.00009(3)
I1	0.01424(5)	0.01397(6)	0.01586(7)	0.00310(5)	-0.00265(5)	-0.00271(4)
I11E	0.01631(6)	0.01265(6)	0.01310(6)	-0.00228(5)	0.00059(5)	-0.00149(5)
N1	0.0130(7)	0.0111(8)	0.0127(9)	-0.0003(6)	-0.0008(6)	-0.0003(6)
N2	0.0128(6)	0.0123(8)	0.0124(8)	-0.0021(7)	0.0019(6)	-0.0012(5)
N3	0.0124(7)	0.0122(9)	0.0157(8)	-0.0029(7)	0.0006(6)	-0.0006(6)
N4	0.0163(8)	0.0125(10)	0.0128(10)	-0.0025(7)	-0.0009(9)	0.0006(7)

N5	0.0131(8)	0.0111(9)	0.0159(8)	0.0005(7)	-0.0029(6)	0.0020(6)
N6	0.0115(7)	0.0117(8)	0.0141(8)	0.0005(7)	-0.0002(6)	0.0003(6)
N7	0.0144(10)	0.0108(9)	0.0135(11)	0.0018(8)	-0.0012(6)	-0.0011(6)
N8	0.0107(7)	0.0118(9)	0.0187(9)	0.0000(7)	-0.0025(6)	0.0005(6)
C1	0.0186(10)	0.0119(10)	0.0176(11)	0.0008(8)	0.0022(8)	-0.0030(7)
C2	0.0150(9)	0.0133(10)	0.0147(10)	0.0005(8)	0.0023(7)	-0.0041(7)
C3	0.0115(8)	0.0158(10)	0.0177(10)	-0.0034(8)	-0.0004(7)	-0.0015(7)
C4	0.0125(9)	0.0159(10)	0.0172(10)	-0.0038(8)	0.0031(7)	-0.0018(8)
C5	0.0165(9)	0.0172(11)	0.0169(10)	-0.0077(9)	0.0005(8)	0.0012(8)
C6	0.0199(10)	0.0188(11)	0.0127(10)	-0.0031(9)	0.0012(8)	-0.0012(8)
C7	0.0180(9)	0.0153(10)	0.0158(10)	-0.0046(8)	-0.0024(7)	-0.0014(8)
C8	0.0160(9)	0.0152(11)	0.0169(10)	-0.0007(8)	-0.0051(8)	0.0000(8)
C9	0.0126(9)	0.0160(11)	0.0200(11)	-0.0016(8)	-0.0024(8)	0.0021(7)
C10	0.0116(8)	0.0186(11)	0.0191(11)	0.0003(9)	0.0016(8)	-0.0014(8)
C11	0.0162(9)	0.0159(11)	0.0132(9)	0.0003(8)	0.0018(7)	0.0023(8)
C12	0.0152(9)	0.0181(11)	0.0123(10)	0.0025(8)	0.0022(8)	-0.0005(7)
C13	0.0183(9)	0.0206(11)	0.0154(10)	0.0068(9)	-0.0017(8)	0.0030(8)
C14	0.0144(9)	0.0169(11)	0.0176(10)	0.0027(9)	-0.0045(8)	0.0014(8)
C15	0.0133(9)	0.0137(10)	0.0264(13)	0.0005(9)	-0.0002(8)	0.0052(8)
C16	0.0155(10)	0.0122(10)	0.0244(12)	-0.0026(9)	0.0019(9)	0.0034(8)
C17	0.0127(8)	0.0118(10)	0.0209(11)	0.0011(8)	0.0008(8)	0.0036(7)
C18	0.0164(10)	0.0118(10)	0.0170(11)	-0.0018(8)	0.0008(8)	0.0025(7)

Table A19. Hydrogen atomic coordinates and isotropic atomic displacement parameters ($Å^2$) for **2.1**-Eu^{II}

	x/a	**y/b**	**z/c**	**U(eq)**
H47	0.0821	0.5627	0.6518	0.019
H46	0.0529	0.5947	0.5437	0.019
H44	0.1133	0.4292	0.4831	0.017
H45	0.1844	0.5003	0.5381	0.017
H42	0.2378	0.2573	0.6515	0.018
H41	0.2713	0.3561	0.5846	0.018
H39	0.2134	0.2778	0.4465	0.018
H40	0.2687	0.1853	0.4995	0.018
H38	0.0788	0.0702	0.3994	0.02
H37	0.1647	0.1251	0.3609	0.02
H36	0.0992	0.3018	0.3649	0.021
H35	0.0502	0.2199	0.2928	0.021
H33	-0.0654	0.0977	0.4137	0.02
H32	-0.0873	0.1683	0.3184	0.02
H30	-0.1826	0.2782	0.4096	0.019
H31	-0.2099	0.1511	0.4152	0.019
H27	-0.2841	0.2137	0.5767	0.019
H26	-0.2447	0.3327	0.5539	0.019
H25	-0.2695	0.3182	0.7213	0.02

H24	-0.2148	0.2074	0.7268	0.02
H2N	0.149(2)	0.388(3)	0.667(3)	0.011(8)
H8M	0.078(3)	0.054(4)	0.699(3)	0.019(10)
H18	-0.1836	0.3526	0.8562	0.018
H19	-0.0935	0.4105	0.8401	0.018
H17	-0.0803	0.2432	0.9301	0.018
H16	-0.1173	0.1762	0.8389	0.018
H4N	-0.029(3)	0.319(3)	0.404(3)	0.014(9)
H15	0.0151	0.0775	0.8628	0.022
H14	0.0627	0.1654	0.9306	0.022
H5N	-0.160(3)	0.151(4)	0.560(3)	0.016(9)
H1N	-0.034(3)	0.469(3)	0.553(4)	0.017(10)
H12	0.1689	0.1897	0.8117	0.02
H13	0.1624	0.0613	0.8389	0.02
H10	0.1951	-0.0260	0.6775	0.021
H9	0.2360	0.0942	0.6652	0.021
H8	0.2153	0.0176	0.5104	0.021
H7	0.1176	-0.0054	0.5339	0.021
H22	-0.1918	0.4994	0.7290	0.018
H23	-0.1826	0.4597	0.6185	0.018
H20	-0.0830	0.5997	0.6547	0.018
H21	-0.0428	0.5241	0.7385	0.018
H7N	0.031(2)	0.301(3)	0.833(3)	0.012(8)

Crystallographic Data for Complex 3.1-Yb^{II}

Table A20. Data collection and structure refinement for **3.1**-Yb^{II}

Theta range for data collection	1.69 to 38.14°	
Index ranges	–15<=h<=16, –28<=k<=29, –30<=l<=27	
Reflections collected	173703	
Independent reflections	15108 [R(int) = 0.0411]	
Coverage of independent reflections	99.4%	
Absorption correction	multi-scan	
Refinement method	Full-matrix least-squares on F^2	
Refinement program	SHELXL-2014/7 (Sheldrick, 2014)	
Function minimized	$\Sigma\, w(F_o^2 - F_c^2)^2$	
Data / restraints / parameters	15108 / 0 / 307	
Goodness-of-fit on F^2	1.338	
Δ/σ_{max}	0.004	
Final R indices	13332 data; I>2σ(I)	R1 = 0.0425, wR2 = 0.1612
	all data	R1 = 0.0498, wR2 = 0.1667
Weighting scheme	$w=1/[\sigma^2(F_o^2)+(0.1000P)^2]$ where $P=(F_o^2+2F_c^2)/3$	
Largest diff. peak and hole	3.986 and –3.775 $eÅ^{-3}$	
R.M.S. deviation from mean	0.218 $eÅ^{-3}$	

Table A21. Atomic coordinates and equivalent isotropic atomic displacement parameters ($Å^2$) for **3.1**-Yb^{II}

	x/a	y/b	z/c	U(eq)
Yb1	0.80749(2)	0.77331(2)	0.91936(2)	0.01482(5)
I1	0.11739(2)	0.80500(2)	0.02212(2)	0.02559(6)
I3	0.31126(3)	0.97614(2)	0.76061(2)	0.02983(7)
F1	0.6122(4)	0.3853(2)	0.0347(3)	0.0668(12)
C7	0.7590(8)	0.9810(3)	0.8836(3)	0.0474(12)
O2	0.8389(4)	0.8742(2)	0.82059(19)	0.0349(7)
C22	0.0268(5)	0.8002(3)	0.7901(3)	0.0360(9)
O3	0.6530(3)	0.71302(16)	0.79746(16)	0.0243(5)
O4	0.5412(3)	0.77325(17)	0.91051(18)	0.0293(6)
N3	0.7111(4)	0.8166(2)	0.0486(2)	0.0308(7)
N4	0.9508(4)	0.7273(2)	0.8068(2)	0.0286(7)
O6	0.9007(3)	0.61532(17)	0.91346(17)	0.0295(5)
O5	0.7653(3)	0.65563(16)	0.01489(17)	0.0306(6)
C1	0.5180(4)	0.6817(2)	0.8069(2)	0.0281(7)
C2	0.4445(4)	0.7482(3)	0.8406(3)	0.0346(8)
C3	0.4824(5)	0.8337(4)	0.9496(3)	0.0402(10)
C4	0.5508(5)	0.8270(3)	0.0337(3)	0.0406(10)
C5	0.7844(6)	0.8946(3)	0.0737(3)	0.0370(9)
C6	0.7488(7)	0.9583(3)	0.0115(3)	0.0457(12)
O1	0.7604(4)	0.92256(18)	0.9427(2)	0.0367(7)
C8	0.7374(6)	0.9370(3)	0.8077(3)	0.0387(9)
C9	0.9294(6)	0.8709(4)	0.7685(3)	0.0447(12)
C10	0.0617(4)	0.6663(3)	0.8431(3)	0.0330(8)
C11	0.9978(5)	0.5924(3)	0.8651(3)	0.0341(9)
C12	0.8314(5)	0.5547(2)	0.9412(3)	0.0327(8)
C13	0.7545(5)	0.5763(2)	0.9962(2)	0.0307(8)
C14	0.7124(5)	0.6754(3)	0.0846(3)	0.0357(9)
C15	0.7633(5)	0.7587(3)	0.1078(2)	0.0320(8)
C16	0.6787(6)	0.5197(3)	0.0274(3)	0.0430(12)
C17	0.6847(6)	0.4412(3)	0.0035(3)	0.0486(14)
C18	0.7604(6)	0.4189(3)	0.9490(3)	0.0453(13)
C19	0.8352(7)	0.4744(3)	0.9190(3)	0.0437(12)
C20	0.8537(5)	0.6954(4)	0.7377(2)	0.0390(10)
C21	0.7179(4)	0.6579(3)	0.7520(2)	0.0328(8)

$U_{(eq)}$ is defined as one third of the trace of the orthogonalized U_{ij} tensor.

Table A22. Bond angles (°) for **3.1**-Yb^{II}

O4-Yb1-O2	103.37(10)	O4-Yb1-O3	63.89(10)
O2-Yb1-O3	78.79(11)	O4-Yb1-O1	78.60(11)
O2-Yb1-O1	60.77(11)	O3-Yb1-O1	115.60(11)
O4-Yb1-O5	75.53(10)	O2-Yb1-O5	174.80(11)
O3-Yb1-O5	96.25(9)	O1-Yb1-O5	123.48(10)
O4-Yb1-N3	62.27(11)	O2-Yb1-N3	121.42(12)
O3-Yb1-N3	125.48(10)	O1-Yb1-N3	60.71(11)
O5-Yb1-N3	62.76(11)	O4-Yb1-N4	127.35(10)
O2-Yb1-N4	61.75(11)	O3-Yb1-N4	63.69(9)
O1-Yb1-N4	120.98(11)	O5-Yb1-N4	114.73(11)
N3-Yb1-N4	170.01(11)	O4-Yb1-O6	108.74(9)
O2-Yb1-O6	121.64(10)	O3-Yb1-O6	73.79(9)
O1-Yb1-O6	170.35(11)	O5-Yb1-O6	54.77(10)
N3-Yb1-O6	116.51(11)	N4-Yb1-O6	59.97(10)
O4-Yb1-I1	147.19(7)	O2-Yb1-I1	93.03(8)
O3-Yb1-I1	148.38(6)	O1-Yb1-I1	85.23(9)
O5-Yb1-I1	90.42(6)	N3-Yb1-I1	84.92(8)
N4-Yb1-I1	85.44(7)	O6-Yb1-I1	85.30(6)
O1-C7-C8	107.4(4)	O1-C7-H7A	110.2
C8-C7-H7A	110.2	O1-C7-H7B	110.2
C8-C7-H7B	110.2	H7A-C7-H7B	108.5
C9-O2-C8	114.8(4)	C9-O2-Yb1	128.7(3)
C8-O2-Yb1	115.8(3)	N4-C22-C9	113.7(4)
N4-C22-H22A	108.8	C9-C22-H22A	108.8
N4-C22-H22B	108.8	C9-C22-H22B	108.8
H22A-C22-H22B	107.7	C1-O3-C21	109.5(3)
C1-O3-Yb1	114.2(2)	C21-O3-Yb1	119.4(2)
C3-O4-C2	112.9(3)	C3-O4-Yb1	118.2(3)
C2-O4-Yb1	120.0(2)	C15-N3-C4	112.5(4)
C15-N3-C5	107.9(4)	C4-N3-C5	109.7(4)
C15-N3-Yb1	108.0(3)	C4-N3-Yb1	113.3(3)
C5-N3-Yb1	105.1(2)	C20-N4-C22	112.1(4)
C20-N4-C10	111.3(4)	C22-N4-C10	108.6(3)
C20-N4-Yb1	112.9(2)	C22-N4-Yb1	104.7(2)
C10-N4-Yb1	106.8(3)	C12-O6-C11	116.2(3)
C12-O6-Yb1	120.6(3)	C11-O6-Yb1	121.5(2)
C13-O5-C14	113.6(3)	C13-O5-Yb1	124.9(3)
C14-O5-Yb1	119.5(2)	O3-C1-C2	106.4(3)
O3-C1-H31	110.5	C2-C1-H31	110.5
O3-C1-H32	110.5	C2-C1-H32	110.5
H31-C1-H32	108.6	O4-C2-C1	107.2(3)
O4-C2-H29	110.3	C1-C2-H29	110.3
O4-C2-H30	110.3	C1-C2-H30	110.3
H29-C2-H30	108.5	O4-C3-C4	107.8(4)
O4-C3-H27	110.1	C4-C3-H27	110.1

O4-C3-H28	110.1	C4-C3-H28	110.1
H27-C3-H28	108.5	C3-C4-N3	112.7(3)
C3-C4-H25	109.0	N3-C4-H25	109.0
C3-C4-H26	109.0	N3-C4-H26	109.0
H25-C4-H26	107.8	N3-C5-C6	112.4(4)
N3-C5-H4	109.1	C6-C5-H4	109.1
N3-C5-H3	109.1	C6-C5-H3	109.1
H4-C5-H3	107.9	O1-C6-C5	106.9(3)
O1-C6-H5	126.6	C5-C6-H5	126.6
C6-O1-C7	111.2(4)	C6-O1-Yb1	127.5(3)
C7-O1-Yb1	121.1(3)	O2-C8-C7	105.3(4)
O2-C8-H24	110.7	C7-C8-H24	110.7
O2-C8-H23	110.7	C7-C8-H23	110.7
H24-C8-H23	108.8	O2-C9-C22	107.2(4)
O2-C9-H21	110.3	C22-C9-H21	110.3
O2-C9-H22	110.3	C22-C9-H22	110.3
H21-C9-H22	108.5	C11-C10-N4	113.2(3)
C11-C10-H7	108.9	N4-C10-H7	108.9
C11-C10-H6	108.9	N4-C10-H6	108.9
H7-C10-H6	107.8	O6-C11-C10	106.9(3)
O6-C11-H16	110.3	C10-C11-H16	110.3
O6-C11-H15	110.3	C10-C11-H15	110.3
H16-C11-H15	108.6	O6-C12-C13	115.6(3)
O6-C12-C19	124.6(5)	C13-C12-C19	119.7(5)
O5-C13-C16	126.1(5)	O5-C13-C12	113.5(4)
C16-C13-C12	120.4(4)	O5-C14-C15	106.9(3)
O5-C14-H11	110.3	C15-C14-H11	110.3
O5-C14-H8	110.3	C15-C14-H8	110.3
H11-C14-H8	108.6	N3-C15-C14	112.8(4)
N3-C15-H9	109.0	C14-C15-H9	109.0
N3-C15-H10	109.0	C14-C15-H10	109.0
H9-C15-H10	107.8	C13-C16-C17	117.9(6)
C13-C16-H14	121.0	C17-C16-H14	121.0
F1-C17-C18	119.4(5)	F1-C17-C16	118.2(6)
C18-C17-C16	122.4(5)	C19-C18-C17	119.5(4)
C19-C18-H12	120.3	C17-C18-H12	120.3
C18-C19-C12	120.0(5)	C18-C19-H13	120.0
C12-C19-H13	120.0	N4-C20-C21	114.5(4)
N4-C20-H20	108.6	C21-C20-H20	108.6
N4-C20-H17	108.6	C21-C20-H17	108.6
H20-C20-H17	107.6	O3-C21-C20	108.3(4)
O3-C21-H18	110.0	C20-C21-H18	110.0
O3-C21-H19	110.0	C20-C21-H19	110.0
H18-C21-H19	108.4		

Table A23. Anisotropic atomic displacement parameters ($Å^2$) for **3.1**-Yb^{II}

	U_{11}	U_{22}	U_{33}	U_{23}	U_{13}	U_{12}
Yb1	0.01471(7)	0.01587(7)	0.01452(7)	0.00087(3)	0.00459(4)	0.00067(3)
I1	0.02249(10)	0.02612(11)	0.02550(11)	-0.00594(7)	-0.00051(8)	-0.00148(7)
I3	0.04293(14)	0.02658(11)	0.02388(11)	-0.00465(7)	0.01581(10)	-0.00701(9)
F1	0.061(2)	0.0331(16)	0.092(3)	0.0189(17)	-0.014(2)	-0.0217(14)
C7	0.069(4)	0.0225(17)	0.047(3)	0.0037(17)	0.007(3)	0.0041(19)
O2	0.0354(15)	0.0354(15)	0.0391(16)	0.0187(13)	0.0192(13)	0.0096(12)
C22	0.0249(16)	0.053(3)	0.034(2)	-0.0042(18)	0.0159(15)	-0.0035(17)
O3	0.0187(10)	0.0271(11)	0.0261(12)	-0.0054(9)	0.0028(9)	-0.0049(9)
O4	0.0182(11)	0.0417(16)	0.0290(13)	0.0000(10)	0.0075(10)	0.0044(9)
N3	0.0310(15)	0.0394(18)	0.0256(14)	-0.0063(12)	0.0136(12)	-0.0022(13)
N4	0.0195(12)	0.0403(18)	0.0270(15)	-0.0122(12)	0.0072(11)	-0.0040(11)
O6	0.0306(13)	0.0243(11)	0.0298(13)	-0.0052(10)	-0.0018(10)	0.0058(10)
O5	0.0353(14)	0.0215(11)	0.0313(13)	0.0062(9)	-0.0008(11)	-0.0069(10)
C1	0.0187(13)	0.0275(15)	0.0347(17)	-0.0012(13)	-0.0016(12)	-0.0056(11)
C2	0.0148(14)	0.051(2)	0.0358(19)	0.0053(19)	0.0002(13)	-0.0023(16)
C3	0.0260(17)	0.057(3)	0.040(2)	-0.005(2)	0.0140(16)	0.0084(18)
C4	0.039(2)	0.054(3)	0.036(2)	0.001(2)	0.0212(18)	0.006(2)
C5	0.050(3)	0.0317(19)	0.0337(19)	-0.0110(15)	0.0196(19)	-0.0025(17)
C6	0.073(4)	0.0235(17)	0.047(3)	-0.0055(17)	0.026(3)	0.009(2)
O1	0.0456(18)	0.0206(12)	0.0461(18)	0.0027(11)	0.0148(14)	0.0045(12)
C8	0.041(2)	0.0324(19)	0.042(2)	0.0133(17)	0.0063(18)	0.0076(17)
C9	0.045(3)	0.057(3)	0.038(2)	0.018(2)	0.022(2)	0.004(2)
C10	0.0185(13)	0.0325(18)	0.049(2)	-0.0191(17)	0.0096(14)	0.0001(12)
C11	0.0295(17)	0.0281(17)	0.040(2)	-0.0134(15)	-0.0031(15)	0.0061(14)
C12	0.0309(17)	0.0196(14)	0.0376(19)	0.0028(13)	-0.0141(15)	-0.0009(12)
C13	0.0324(17)	0.0210(14)	0.0305(17)	0.0020(12)	-0.0104(14)	-0.0034(12)
C14	0.0349(19)	0.042(2)	0.0300(18)	0.0130(16)	0.0068(15)	-0.0083(17)
C15	0.036(2)	0.040(2)	0.0209(15)	0.0051(14)	0.0086(14)	-0.0044(17)
C16	0.040(2)	0.0302(19)	0.048(3)	0.0121(17)	-0.013(2)	-0.0141(17)
C17	0.055(3)	0.0285(19)	0.048(3)	0.0139(18)	-0.020(2)	-0.0147(19)
C18	0.060(3)	0.0242(17)	0.037(2)	-0.0050(15)	-0.021(2)	0.0077(18)
C19	0.061(3)	0.0271(18)	0.030(2)	-0.0047(14)	-0.018(2)	0.0073(19)
C20	0.0279(18)	0.067(3)	0.0212(16)	-0.0101(18)	0.0028(14)	0.0005(19)
C21	0.0267(16)	0.045(2)	0.0226(14)	-0.0101(15)	-0.0027(13)	-0.0033(15)

Table A24. Hydrogen atomic coordinates and isotropic atomic displacement parameters ($Å^2$) for **3.1**-Yb^{II}

	x/a	y/b	z/c	U(eq)
H7A	0.8513	1.0106	0.8936	0.057
H7B	0.6796	1.0195	0.8824	0.057
H22A	1.0754	0.7887	0.7475	0.043
H22B	1.1022	0.8140	0.8362	0.043
H31	0.5335	0.6352	0.8420	0.034
H32	0.4584	0.6647	0.7565	0.034
H29	0.4234	0.7933	0.8039	0.041
H30	0.3526	0.7291	0.8517	0.041
H27	0.3767	0.8271	0.9413	0.048
H28	0.5025	0.8869	0.9300	0.048
H25	0.5083	0.7810	1.0556	0.049
H26	0.5287	0.8757	1.0604	0.049
H4	0.8900	0.8862	1.0872	0.044
H3	0.7542	0.9135	1.1205	0.044
H5	0.7236	1.0123	1.0184	0.055
H24	0.6380	0.9157	0.7924	0.046
H23	0.7549	0.9728	0.7665	0.046
H21	0.9870	0.9205	0.7713	0.054
H22	0.8717	0.8650	0.7152	0.054
H7	1.1227	0.6531	0.8063	0.04
H6	1.1248	0.6898	0.8895	0.04
H16	0.9446	0.5641	0.8186	0.041
H15	1.0740	0.5566	0.8935	0.041
H11	0.7514	0.6373	1.1265	0.043
H8	0.6058	0.6729	1.0736	0.043
H9	0.7304	0.7737	1.1549	0.038
H10	0.8700	0.7595	1.1202	0.038
H14	0.6240	0.5340	1.0641	0.052
H12	0.7599	0.3649	0.9327	0.054
H13	0.8905	0.4592	0.8829	0.052
H20	0.9066	0.6550	0.7141	0.047
H17	0.8266	0.7393	0.7000	0.047
H18	0.6500	0.6469	0.7023	0.039
H19	0.7409	0.6069	0.7800	0.039

Crystallographic Data for Complex 2.1-Yb^{II}

Table A25. Data collection and structure refinement for **2.1**-Yb^{II}

Theta range for data collection	2.44 to 41.77°	
Index ranges	–16<=h<=17, -15<=k<=17, –29<=l<=29	
Reflections collected	78655	
Independent reflections	2901 [R(int) = 0.0369]	
Coverage of independent reflections	97.1%	
Absorption correction	multi-scan	
Refinement method	Full-matrix least-squares on F^2	
Refinement program	SHELXL-2014/7 (Sheldrick, 2014)	
Function minimized	$\Sigma\, w(F_o^2 - F_c^2)^2$	
Data / restraints / parameters	2901 / 0 / 46	
Goodness-of-fit on F^2	1.333	
Final R indices	2826 data; I>2σ(I)	R1 = 0.0186, wR2 = 0.0491
	all data	R1 = 0.0196, wR2 = 0.0494
Weighting scheme	$w=1/[\sigma^2(F_o^2)+(0.0158P)^2+1.2296P]$ where $P=(F_o^2+2F_c^2)/3$	
Absolute structure parameter	0.0(0)	
Largest diff. peak and hole	1.177 and –4.070 eÅ^{-3}	
R.M.S. deviation from mean	0.158 eÅ^{-3}	

Table A26. Atomic coordinates and equivalent isotropic atomic displacement parameters (Å^2) for **2.1**-Yb^{II}

	x/a	y/b	z/c	U(eq)
Yb1	0.6667	0.3333	0.75	0.00551(3)
I2	0.0	0.0	0.5	0.01573(4)
I3	0.3333	0.6667	0.75	0.02148(5)
N1	0.6667	0.3333	0.58691(10)	0.0104(2)
N2	0.68171(12)	0.59483(12)	0.69056(6)	0.01052(14)
C1	0.63554(16)	0.57894(16)	0.60518(8)	0.01351(19)
C2	0.71345(16)	0.49856(15)	0.55762(7)	0.01285(18)
C3	0.84579(16)	0.73492(14)	0.70641(8)	0.01275(18)

Table A27. Bond angles (°) for **2.1**-Yb^{II}

N2-Yb1-N2	174.57(5)	N2-Yb1-N2	106.35(3)
N2-Yb1-N2	69.20(5)	N2-Yb1-N2	69.20(5)
N2-Yb1-N2	106.35(3)	N2-Yb1-N2	78.25(5)
N2-Yb1-N2	106.35(3)	N2-Yb1-N2	78.25(5)
N2-Yb1-N2	106.35(3)	N2-Yb1-N2	174.57(4)
N2-Yb1-N2	78.25(5)	N2-Yb1-N2	106.35(3)
N2-Yb1-N2	174.57(5)	N2-Yb1-N2	106.35(3)
N2-Yb1-N2	69.20(5)	N2-Yb1-N1	112.43(2)

N2-Yb1-N1	67.57(2)	N2-Yb1-N1	112.43(2)
N2-Yb1-N1	67.57(2)	N2-Yb1-N1	112.43(2)
N2-Yb1-N1	67.57(2)	N2-Yb1-N1	67.57(2)
N2-Yb1-N1	112.43(2)	N2-Yb1-N1	67.57(2)
N2-Yb1-N1	112.43(2)	N2-Yb1-N1	67.57(2)
N2-Yb1-N1	112.43(2)	N1-Yb1-N1	180.0
C2-N1-C2	109.61(8)	C2-N1-C2	109.61(8)
C2-N1-C2	109.61(8)	C2-N1-Yb1	109.33(8)
C2-N1-Yb1	109.33(8)	C2-N1-Yb1	109.33(8)
C3-N2-C1	112.91(10)	C3-N2-Yb1	108.55(7)
C1-N2-Yb1	113.51(7)	N2-C1-C2	111.28(10)
N2-C1-H1A	109.4	C2-C1-H1A	109.4
N2-C1-H1B	109.4	C2-C1-H1B	109.4
H1A-C1-H1B	108.0	N1-C2-C1	113.06(10)
N1-C2-H2A	109.0	C1-C2-H2A	109.0
N1-C2-H2B	109.0	C1-C2-H2B	109.0
H2A-C2-H2B	107.8	N2-C3-C3	109.63(9)
N2-C3-H3A	109.7	C3-C3-H3A	109.7
N2-C3-H3B	109.7	C3-C3-H3B	109.7
H3A-C3-H3B	108.2		

Table A28. Anisotropic atomic displacement parameters ($Å^2$) for **2.1**-Yb^{II}

	U_{11}	U_{22}	U_{33}	U_{23}	U_{13}	U_{12}
Yb1	0.00498(3)	0.00498(3)	0.00658(4)	0	0	0.00249(2)
I2	0.01829(6)	0.01829(6)	0.01062(8)	0	0	0.00914(3)
I3	0.00909(5)	0.00909(5)	0.04625(15)	0	0	0.00455(2)
N1	0.0115(4)	0.0115(4)	0.0080(6)	0	0	0.00577(19)
N2	0.0103(3)	0.0090(3)	0.0123(4)	0.0008(3)	-0.0001(3)	0.0049(3)
C1	0.0152(5)	0.0135(4)	0.0136(4)	0.0024(3)	-0.0030(4)	0.0086(4)
C2	0.0162(5)	0.0136(4)	0.0086(4)	0.0031(3)	0.0004(3)	0.0073(4)
C3	0.0146(4)	0.0073(4)	0.0131(4)	0.0013(3)	0.0005(3)	0.0030(3)

Table A29. Hydrogen atomic coordinates and isotropic atomic displacement parameters ($Å^2$) for **2.1**-Yb^{II}

	x/a	y/b	z/c	U(eq)
H1A	0.6708	0.6885	0.5827	0.016
H1B	0.5152	0.5128	0.6003	0.016
H2A	0.6809	0.4912	0.5007	0.015
H2B	0.8337	0.5683	0.5604	0.015
H3A	0.8476	0.8380	0.6935	0.015
H3B	0.9272	0.7275	0.6720	0.015

APPENDIX B

PERMISSION/LICENSE AGREEMENT FOR COPYRIGHTED MATERIALS

Title:	Metal–Organic Framework Luminescence in the Yellow Gap by Codoping of the Homoleptic Imidazolate ∞3[Ba(Im)2] with Divalent Europium
Author:	Jens-Christoph Rybak, Michael Hailmann, Philipp R. Matthes, et al
Publication:	Journal of the American Chemical Society
Publisher:	American Chemical Society
Date:	May 1, 2013
Copyright © 2013, American Chemical Society	

Logged in as:
Akhila Kuda
Account #:
3000732972

LOGOUT

PERMISSION/LICENSE IS GRANTED FOR YOUR ORDER AT NO CHARGE

This type of permission/license, instead of the standard Terms & Conditions, is sent to you because no fee is being charged for your order. Please note the following:

- Permission is granted for your request in both print and electronic formats, and translations.
- If figures and/or tables were requested, they may be adapted or used in part.
- Please print this page for your records and send a copy of it to your publisher/graduate school.
- Appropriate credit for the requested material should be given as follows: "Reprinted (adapted) with permission from (COMPLETE REFERENCE CITATION). Copyright (YEAR) American Chemical Society." Insert appropriate information in place of the capitalized words.
- One-time permission is granted only for the use specified in your request. No additional uses are granted (such as derivative works or other editions). For any other uses, please submit a new request.

If credit is given to another source for the material you requested, permission must be obtained from that source.

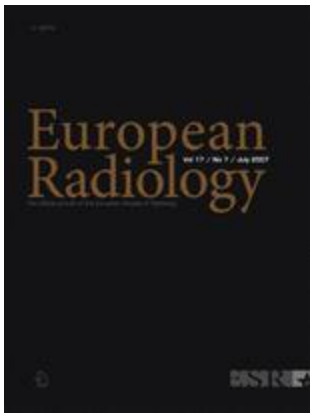

Title: Imaging of adult astrocytic brain tumours with 7 T MRI: preliminary results
Author: Christoph Moenninghoff
Publication: European Radiology
Publisher: Springer
Date: Jan 1, 2009

Order Completed

Thank you very much for your order.
This is a License Agreement between Akhila W Kuda-weadgedara ("You") and Springer ("Springer"). The license consists of your order details, the terms and conditions provided by Springer, and the payment terms and conditions.Get the printable license.

License Number	3700370438734
License date	Sep 01, 2015
Licensed content publisher	Springer
Licensed content publication	European Radiology
Licensed content title	Imaging of adult astrocytic brain tumours with 7 T MRI: preliminary results
Licensed content author	Christoph Moenninghoff
Licensed content date	Jan 1, 2009
Volume number	20
Issue number	3
Type of Use	Thesis/Dissertation
Portion	Figures
Author of this Springer article	No
Original figure numbers	Figure 2
Title of your thesis / dissertation	LNII-CONTAINING CRYPTATES: SYNTHESIS, PROPERTIES, AND APPLICATIONS
Expected completion date	Oct 2015
Estimated size(pages)	200
Total	0.00 USD

Title: Aqueous EuII-Containing Complex with Bright Yellow Luminescence
Author: Akhila N. W. Kuda-Wedagedara, Chengcheng Wang, Philip D. Martin, et al
Publication: Journal of the American Chemical Society
Publisher: American Chemical Society
Date: Apr 1, 2015

PERMISSION/LICENSE IS GRANTED FOR YOUR ORDER AT NO CHARGE

This type of permission/license, instead of the standard Terms & Conditions, is sent to you because no fee is being charged for your order. Please note the following:

- Permission is granted for your request in both print and electronic formats, and translations.
- If figures and/or tables were requested, they may be adapted or used in part.
- Please print this page for your records and send a copy of it to your publisher/graduate school.
- Appropriate credit for the requested material should be given as follows: "Reprinted (adapted) with permission from (COMPLETE REFERENCE CITATION). Copyright (YEAR) American Chemical Society." Insert appropriate information in place of the capitalized words.
- One-time permission is granted only for the use specified in your request. No additional uses are granted (such as derivative works or other editions). For any other uses, please submit a new request.

REFERENCES

(1) Shinoda, S.; Nishioka, M.; Tsukube, H. *J. Alloys Compd.* **2009,** *488*, 603.

(2) Garcia, J.; Allen, M. J. *Eur. J. Inorg. Chem.* **2012,** *2012*, 4550.

(3) Bulgakov, R. G.; Eliseeva, S. M.; Galimov, D. I. *RSC. Adv.* **2015,** *5*, 52132.

(4) Ramanantoanina, H.; Cimpoesu, F.; Gottel, C.; Sahnoun, M.; Herden, B.; Suta, M.; Wickleder, C.; Urland, W.; Daul, C. *Inorg. Chem., ASAP*.

(5) Fieser, M. E.; MacDonald, M. R.; Krull, B. T.; Bates, J. E.; Ziller, J. W.; Furche, F.; Evans, W. J. *J. Am. Chem. Soc.* **2015,** *137*, 369.

(6) Garcia, J.; Kuda-Wedagedara, A. N. W.; Allen, M. J. *Eur. J. Inorg. Chem.* **2012,** *2012*, 2135.

(7) Evans, W. J.; Allen, N. T.; Ziller, J. W. *J. Am. Chem. Soc.* **2000,** *122*, 11749.

(8) Gamage, N. D. H.; Mei, Y.; Garcia, J.; Allen, M. J. *Angew. Chem., Int Ed.* **2010,** *49*, 8923.

(9) Chciuk, T. V.; Flowers, I., R. A. *J. Am. Chem. Soc.* **2015,** *137*, 11526.

(10) Girard, P.; Namy, J. L.; Kagan, H. B. *J. Am. Chem. Soc.* **1980,** *102*, 2693.

(11) Szostak, M.; Procter, D. J. *Angew. Chem., Int Ed.* **2012,** *51*, 37.

(12) Namy, J. L.; Girard, P.; Kagan, H. B. *Nouv. J. Chim.* **1977**, *1*, 5.

(13) Inanaga, J.; Ishikawa, M.; Yamaguchi, M. *Chem. Lett.* **1987,** 1485.

(14) Dahlén, A.; Hilmersson, G.; Knettle, B. W.; Flowers, I., R. A. *J. Org. Chem.* **2003**, *68*, 4870.

(15) Yasuko, K.; Kudo, Y. *Yuki Gosei Kagaku kyokaishi* **1994,** *52*, 285.

(16) Inanaga, J.; Handa, Y.; Tabuchi, T.; Otsubo, K.; Yamaguchi, M.; Hanamoto, T. *Tetrahedron Lett.* **1991,** *32*, 6557.

(17) Prasad, E.; Flowers, I., R. A. *J. Am. Chem. Soc.* **2002,** *124*, 6895.

(18) Szostak, M.; Spain, M.; Eberhart, A. J.; Procter, D. J. *J. Am. Chem. Soc.* **2013**.

(19) Choquette, K. A.; Sadasivam, D. V.; Flowers, I., R. A. *J. Am. Chem. Soc.* **2011,** *133*, 10655.

(20) Prasad, E.; Flowers, I., R. A. *J. Am. Chem. Soc.* **2005,** *127*, 18093.

(21) Dahlén, A.; Hilmersson, G. *Tetrahedron Lett.* **2002,** *43*, 7197.

(22) Szostak, M.; Sautier, B.; Spain, M.; Procter, D. *J. Org. Lett.* **2014,** *16*, 1092.

(23) Amiel-Levy, M.; Hoz, S. *Chem. Eur. J.* **2010,** *16*, 805.

(24) Ogawa, A.; Sumino, Y.; Nanke, T.; Ohya, S.; Sonoda, N.; Hirao, T. *J. Am. Chem. Soc.* **1997,** *119*, 2745.

(25) Sun, L.; Sahloul, K.; Mellah, M. *ACS Catal.* **2013,** *3*, 2568.

(26) Sun, L.; Mellah, M. *Organometallics* **2014,** *33*, 4625.

(27) Nomura, R.; Matsuno, T.; Endo, T. *J. Am. Chem. Soc.* **1996,** *118*, 11666.

(28) Corey, E. J.; Z., G. Z. *Tetrahedron Lett.* **1997,** *38*, 2045.

(29) Orsini, F.; Lucci, E. M. *Tetrahedron Lett.* **2005,** *46*, 1909.

(30) Lee, C. C.; Hu, Y.; Ribbe, M. W. *Angew. Chem., Int Ed.* **2015,** *127*, 1235.

(31) Wang, S.; Zhou, S. S., E.; Xie, M.; Zhang, K.; Cheng, L.; Feng, Y.; Mao, L. H., Z. *Organometallics* **2003,** *22*, 3546.

(32) Schmid, M.; Guillaume, S. M.; W., R. P. *Organometallics* **2014,** *33*, 5392.

(33) Basalov, I. V.; Rosca, S. C.; Lyubov, D. M.; Selikhov, A. N.; Georgy, K. F.; Sarazin, Y.; Carpentier, J. F.; Trifonov, A. A. *Inorg. Chem.* **2014,** *53*, 1654.

(34) Dorenbos, P. *J. Phys. Condens. Matter* **2003,** *15*, 575.

(35) Ju, G.; Hu, Y.; Chen, L.; Wang, X.; Mu, Z. *Optical Materials* **2014,** *36*, 1920.

(36) Rybak, J.-C.; Hailmann, M.; Matthes, P. R.; Zurawski, A.; Nitsch, J.; Steffen, A.; Heck, J. G.; Feldmann, C.; Götzendörfer, S.; Meinhardt, J.; Sextl, G.; Kohlmann, H.; Sedlmaier, S. J.; Schnick, W.; Müller-Buschbaum, K. *J. Am. Chem. Soc.* **2013,** *135*, 6896.

(37) Wang, Y.; Brik, M. G.; Dorenbos, P.; Huang, Y.; Tao, Y.; Liang, H. *J. Phys. Chem. C* **2014,** *118*, 7002.

(38) Kunkel, N.; Kohlmann, H.; Sayede, A.; Springborg, M. *Inorg. Chem.* **2011,** *50*, 5873.

(39) Zhang, Z.; ten Kate, O. M.; Delsing, A. C. A.; Stevens, M. J. H.; Zhao, J.; Notten, P. H. L.; Dorenbos, P.; Hintzen, H. T. *J. Mater. Chem.* **2012,** *22*, 23871.

(40) Xie, J.; Hirosaki, N.; Mitomo, M.; Uheda, K.; Suehiro, T.; Xu, X.; Yamamoto, Y.; Sekiguchi, T. *J. Phys. Chem. B* **2005,** *109*, 9490.

(41) Jiang, J.; Higashiyama, N.; Machida, K.-I.; Adachi, G.-Y. *Coord. Chem. Rev.* **1998,** *170*, 1.

(42) Sabbatini, N.; Ciano, M.; Dellonte, S.; Bonazzi, A.; Bolletta, F.; Balzani, V. *J. Phys. Chem.* **1984,** *88*, 1534.

(43) Teprovich, J., J. A.; Prasad, E.; Flowers, I., R. A. *Angew. Chem., Int Ed.* **2007,** *46*, 1148.

(44) Cotton, F. A.; Faut, O. D.; Goodgame, D. M. L.; Holm, R. H. *J. Am. Chem. Soc.* **1961,** *83*, 1780.

(45) Meihaus, K. R.; Fieser, M. E.; Corbey, J. F.; Evans, W. J.; Long, J. R. *J. Am. Chem. Soc.* **2015,** *137*, 9855.

(46) Zucchi, G.; Thuéry, P.; Riviére, E.; Ephritikhine, M. *Chem. Commun.* **2010,** *46*, 9143.

(47) Duyn, J. H. *NeuroImage* **2012,** *62*, 1241.

(48) Moser, E.; Stahlberg, F.; Ladd, M. E.; Trattnig, S. *NMR Biomed.* **2012,** *25*, 695.

(49) Kraff, O.; Fischer, A.; Nagel, A. M.; Mönninghoff, C.; Ladd, M. E. *J. Magn. Reson. Imaging* **2014,** DOI: 10.1002/jmri.24573

(50) Moser, E. *World J. Radiol.* **2010,** *2*, 37.

(51) Kollia, K.; Maderwald, S.; Putzki, N.; Schlamann, M.; Theysohn, J. M.; Kraff, O.; Ladd, M. E.; Frosting, M.; Wanke, I. *Am. J. Neuroradiol.* **2009,** *30*, 699.

(52) Beisteiner, R.; Robinson, S.; Wurnig, M.; Hilbert, M.; Merksa, K.; Rath, J.; Höllninger, I.; Kilinger, N.; Marosi, C.; Trattnig, S.; Geiβler, A. *NeuroImage* **2011,** *57*, 1015.

(53) Moenninghoff, C.; Maderwald, S.; Theysohn, J. M.; Kraff, O.; Ladd, M. E.; Hindy, N. E.; van de Nes, J.; Frosting, M.; Wanke, I. *Eur. Radiol.* **2010,** *20*, 704.

(54) van der Kolk, A. G.; Hendrikse, J.; Zwanenburg, J. J. M.; Visser, F.; Luijten, P. R. *Eur. J. Radiol.* **2013,** *82*, 708.

(55) Li, D.; Zheng, J.; Weinmann, H.-J. *Radiology* **2001**, *218*, 670.

(56) Huang, S.; Liu, C.; Dai, G.; Kim, Y. R.; Rosen, B. R. *NeuroImage* **2009**, *46*, 589.

(57) Villaraza, A. J. L.; Bumb, A.; Brechbiel, M. W. *Chem. Rev.* **2010**, *110*, 2921.

(58) Tu, C.; Osborne, E. A.; Louie, Y. *Ann. Biomed. Eng.* **2011**, *39*, 1335.

(59) Helm, L. *Future Med. Chem.* **2010**, *2*, 385.

(60) Hagberg, G. E.; Sheffler, K. *Contrast Media Mol. Imaging* **2013**, *8*, 456.

(61) Richardson, O. C.; Scott, M. L. J.; Tanner, S. F.; Waterton, J. C.; Buckley, D. L. *Magn. Reson. Med.* **2012,** *68*, 1234.

(62) Rosenberg, J. T.; Kogot, J. M.; Ridel, C.; Strouse, G. F.; Grant, S. C. *Proc. Intl. Soc. Magn. Reson. Med.* **2009,** *17*, 921.

(63) Xue, S.; Qiao, J.; Pu, F.; Cameron, M.; Yang, J. *J. Nanobiotechnol.* **2013,** *5*, 163.

(64) Terreno, E.; Castelli, D. D.; Viale, A. A., S. *Chem. Rev.* **2010,** *110*, 3019.

(65) Heffern, M. C.; Matosziuk, L. M.; Meade, T. J. *Chem. Rev.* **2014,** *114*, 4496.

(66) Hsieh, V.; Jasanoff, A. *ACS Chem. Neurosci.* **2012,** *3*, 593.

(67) Rohrer, M.; Bauer, H.; Mintorovitch, J.; Requardt, M.; Weinmann, H.-J. *Invest. Radiol.* **2005,** *40*, 715.

(68) Noebauer-Huhmann, I. M.; Szomolanyi, P.; Juras, V.; Kraff, O.; Ladd, M. E.; Trattnig, S. *Invest. Radiol.* **2010,** *45*, 554.

(69) Garcia, J.; Allen, M. J. *Inorg. Chim. Acta* **2012,** *393*, 324.

(70) Greenwood, N. N.; Earnshaw, A. *Chemistry of the Elements*; 2nd Ed. ed., 2005.

(71) Burai, L.; Scopelliti, R.; Tóth, É. *Chem. Commun.,* **2002,** 2366.

(72) Gál, M.; Kielar, F.; Sokolová, R.; Ramešová, S.; Kolivoška, V. *Eur. J. Inorg. Chem.* **2013,** 3217.

(73) Butler, S. J.; Lamarque, L.; Pal, R.; Parker, D. *Chem. Sci.* **2014,** *5*, 1750.

(74) Jun, S.; Lee, J.; Jang, E. *ACS Nano* **2013,** *7*, 1472.

(75) Dong, Y.; Pang, H.; Yang, H. B.; Guo, C.; Shao, J.; Chi, Y.; Li, C. M.; Yu, T. *Angew. Chem. Int. Ed.* **2013,** *52*, 7800.

(76) Goedhart, J.; von Stetten, D.; Noirclerc-Savoye, M.; Lelimousin, M.; Joosen, L.; Hink, M. A.; van Weeren, L.; Gadella, T. W. J., Jr.; Royant, A. *Nat. Commun.* **2012,** *3*, 751.

(77) de Bettencourt-Dias, A.; Barber, P. S.; Bauer, S. *J. Am. Chem. Soc.* **2012,** *134*, 6987.

(78) Panada, S. K.; Hickey, S. G.; Waurisch, C.; Eychmüller, A. *J. Mater. Chem.* **2011,** *21*, 11550.

(79) Maldiney, T.; Richard, C.; Seguin, J.; Wattier, N.; Bessodes, M.; Scherman, D. *ACS Nano* **2011**, *5*, 854.

(80) Zhao, Y.; Rabouw, F. T.; van Puffelen, T.; van Walree, C. A.; Gamelin, D. R.; de Mello Donegá, C.; Meijerink, A. *J. Am. Chem. Soc.* **2014**, *136*, 16533.

(81) Marks, S.; Heck, J. G.; Habicht, M. H.; Oña-Burgos, P.; Feldmann, C.; Roesky, P. W. *J. Am. Chem. Soc.* **2012**, *134*, 16983.

(82) Maldiney, T.; Lecointre, A.; Viana, B.; Bessière, A.; Bessodes, M.; Gourier, D.; Richard, C.; Scherman, D. *J. Am. Chem. Soc.* **2011**, *133*, 11810.

(83) Harder, S.; Naglav, D.; Ruspic, C.; Wickleder, C.; Adlung, M.; Hermes, W.; Eul, M.; Pöttgen, R.; Rego, D. B.; Poineau, F.; Czerwinski, K. R.; Herber, R. H.; Nowik, I. *Chem. Eur. J.* **2013**, *19*, 12272.

(84) Bachmann, V.; Jüstel, T.; Meijerink, A.; Ronda, C.; Schmidt, P. J. J. L.; Shipley, C. P.; Capecchi, S.; Salata, O. V.; Etchells, M.; Dobson, P. J.; Christou, V. *Adv. Mater.* **1999,** *11*, 533.

(85) Adachi, G.-Y.; Fujkawa, H.; Tomokiyo, K.; Sorita, K.; Kawata, K.; Shiokawa, J. *Inorg. Chim. Acta* **1986,** *113*, 87.

(86) Higashiyama, N.; Takemura, K.; Kimura, K.; Adachi, G.-Y. *Inorg. Chim. Acta* **1992,** *194*, 201.

(87) Wang, C.; Xu, L.; Li, X.; Lin, Q. *Chem. Phys. Chem.* **2012,** *13*, 3765.

(88) Redko, M. Y.; Huang, R.; Dye, J. L.; Jackson, J. E. *Synthesis* **2006,** *5*, 759.

(89) Smith, P. H.; Barr, M. E.; Brainard, J. R.; Ford, D. K.; Freiser, H.; Muralidharan, S.; Reilly, S. D.; Ryan, R. R.; Silks, I., L. A.; Yu, W.-h. *J. Org. Chem.* **1993,** *58*, 7939.

(90) Garcia, J.; Neelavalli, J.; Haacke, E. M.; Allen, M. J. *Chem. Commun.* **2011,** *47*, 12858.

(91) Würth, C.; Grabolle, M.; Pauli, J.; Spieles, M.; Resch-Genger, U. *Anal. Chem.* **2011,** *83*, 3431.

(92) Brouwer, A. M. *Pure Appl. Chem.* **2011,** *83*, 2213.

(93) Magde, D.; Wong, R.; Seybold, P. G. *Photochem. Photobiol.* **2002,** *75*, 327.

(94) Weast, R. C. *CRC Handbook of Chemistry and Physics*; CRC PRESS, Inc.: Boca Raton, FL, 1980.

(95) Hübschle, C. B.; Sheldrick, G. M.; Dittrich, B. *J. Appl. Crystallogr.* **2011,** *44*, 1281.

(96) Ekanger, L. A.; Ali, M. M.; Allen, M. J. *Chem. Commun.* **2014,** *50*, 14835.

(97) Baker, A. T. *J. Chem. Educ.* **1998,** *75*, 98.

(98) Supkowski, R. M.; Horrocks, W. D., Jr. *Inorg. Chim. Acta* **2002,** *340*, 44.

(99) Beeby, A.; Parker, D.; Williams, J. A. G. *J. Chem. Soc., Perkin Trans. 2* **1996,** 1565.

(100) Dissanayake, P.; Mei, Y.; Allen, M. J. *ACS Catal.* **2011,** *1*, 1203.

(101) Dissanayake, P.; Allen, M. J. *J. Am. Chem. Soc.* **2009,** *131*, 6342.

(102) Moore, J. D.; Lord, R. L.; Cisneros, G. A.; Allen, M. J. *J. Am. Chem. Soc.* **2012,** *134*, 17372.

(103) Horrocks, W. D., Jr.; Sudnick, D. R. *J. Am. Chem. Soc.* **1979,** *101*, 334.

(104) Creaser, I. I.; Geue, R. J.; Harrowfield, J. M.; Herlt, A. J.; Sargeson, A. M.; Snow, M. R.; Springborg, J. *J. Am. Chem. Soc.* **1982,** *104*, 6015.

(105) Ruiz-Martínez, A.; Casanova, D. A., S. *Chem. Eur. J.* **2008,** *14*, 1291.

(106) Renny, S. J.; Tomasevich, L. L.; Tallmadge, E. H.; Collum, D. B. *Angew. Chem. Int. Ed.* **2013,** *52*, 11998.

(107) Cossy, C.; Helm, L.; Merbach, A. E. *Inorg. Chem.* **1988,** *27*, 1973.

(108) Urbanczyk-Pearson, L. M.; Femia, F. J.; Smith, J.; Parigi, G.; Duimstra, J. A.; Eckermann, A. L.; Luchinat, C.; Meade, T. *J. Inorg. Chem.* **2008,** *47*, 56.

(109) Girolami, G. S.; Rauchfuss, T. B.; Angelici, R. *Synthesis and technique in inorganic chemistry: a laboratory manual; University Science Books*; University Science Books: Sausalito, CA, 1999.

(110) Parr, R. G.; Pearson, R. G. *J. Am. Chem. Soc.* **1983,** *105*, 7512.

(111) Pearson, R. G. *J. Am. Chem. Soc.* **1963,** *85*, 3533.

(112) Yee, E. L.; Gansow, O. A.; Weaver, M. J. *J. Am. Chem. Soc.* **1980,** *102*, 2278.

(113) Kuda-Wedagedara, A. N. W.; Wang, C.; Martin, P. D.; Allen, M. J. *J. Am. Chem. Soc.* **2015,** *137*, 4960.

(114) Ekanger, L. A.; Polin, L. A.; Shen, Y.; Haacke, E. M.; Martin, P. D.; Allen, M. J. *Angew. Chem. Int. Ed.* **2015,** *in press*.

(115) Geary, W. *Coord. Chem. Rev.* **1971,** *7*, 81.

(116) Shah, P. A.; Shah, J. V.; Sanyal, M.; Shrivastav, P. S. *Int. J. Pharm. Pharm. Sci.* **2015,** *6*, 105.

(117) Shabangi, M.; Flowers, I., R. A. *Tetrahedron Lett.* **1997,** *38*, 1137.

(118) Regueiro-Figueroa, M.; Barriada, J. L.; Pallier, A.; Esteban-Gómez, D.; de Blas, A.; Rodríguez-Blas, T.; Tóth, É.; Platas-Iglesias, C. *Inorg. Chem.* **2015,** *54*, 4940.

(119) Zitz, R.; Hlina, J.; Gatterer, K.; Marschner, C.; Szilvási, T.; Baumgartner, J. *Inorg. Chem.* **2015,** *54*, 7065.

(120) Maity, S.; Choquette, K. A.; Flowers, I., R. A.; Prasad, E. *J. Phys. Chem. A* **2012,** *116*, 2154.

(121) Labouille, S.; Clavaguréra, N., F. *Organometallics* **2013,** *32*, 1265.

(122) Seibig, S.; Tóth, É.; Merbach, A. E. *J. Am. Chem. Soc.* **2000,** *122*, 5822.

(123) Reda, T.; Barker, C. D.; Hirst, J. *Biochemistry* **2008,** *47*, 8885.

(124) Burdett, J. K.; Hoffmann, R.; Fay, R. C. *Inorg. Chem.* **1978,** *17*, 2553.

(125) White III, J. P.; Deng, H.; Boyd, E. P.; Gallucci, J.; Shore, S. G. *Inorg. Chem.* **1994,** *33*, 1685.

(126) Starynowicz, P.; Gatner, K. Z. *Anorg. Allg. Chem.* **2003,** *629*, 722.

(127) Cox, B. G.; Truong, N. V.; Garcia-Rosas, J.; Schneider, H. *J. Phys. Chem.* **1984,** *88*, 996.

(128) Chopade, P. R.; Davis, T. A.; Prasad, E.; Flowers II, R. A. *Org. Lett.* **2004,** *16*, 2685.

(129) Edgar, A.; Varoy, C. R.; Koughia, C.; Tonchev, D.; Belev, G.; Okada, G.; Kasap, S. O.; Von Seggern, H.; Rayan, M. *Optical Materials* **2009,** *31*, 1459.

ABSTRACT

LN^{II}-CONTAINING CRYPTATES: SYNTHESIS AND PROPERTIES

by

AKHILA N. W. KUDA-WEDAGEDARA

May 2016

Advisor: Dr. Matthew J. Allen

Major: Chemistry

Degree: Doctor of Philosophy

Research projects described in this dissertation are focused on studying the physicochemical properties, including the photochemical, redox, and magnetic properties, of Ln^{II}-containing cryptates and how ligand structure influences metal–ligand interactions that in turn influence physicochemical properties. The results of these studies enable tailoring of the coordination properties of metal complexes that are important in applications including luminescent materials, chemical reductions, catalysis, and imaging.

A Eu^{II}-containing cryptate **2.1**-Eu^{II} synthesized with an amine-rich ligand displayed bright yellow luminescence in aqueous solution with a quantum yield of 26% that is so far the highest quantum yield reported for Eu^{II} in aqueous solution. The bright luminescence of the complex **2.1** was likely a result of the absence of coordinated water molecules based on solid- and solution-phase characterization. Additionally, the X-ray crystal structure revealed a rare 9-coordination staggered hula-hoop geometry.

Investigation of coordination chemistry of the Eu^{II} ion with ether-rich and amine-rich cryptates synthesized with ligands **1.7**, **1.17**, **3.1**, and **2.1** revealed that field strength of ligands influence the physicochemical properties where strong-field ligands shift the absorption and

emission spectra toward lower energy and the oxidation potentials to more negative potentials relative to weak-field ligands. X-ray crystal structures of **3.1**-Eu^{II} and **2.1**-Eu^{II} displayed eclipsed and staggered hula-hoop geometries.

The use of the ligand series **1.7**, **1.17**, **3.1**, and **2.1** with the Yb^{II} ion displayed similar shifts in absorption spectra and oxidation peak potentials. X-ray crystal structures of **3.1**-Yb^{II} and **2.1**-Yb^{II} revealed 9-coordinate eclipsed hula-hoop and 8-coordinate bicapped trigonal antiprism geometries, respectively.

Investigation of influence of coordination environment of structurally varied cryptand-type ligands on the physicochemical properties of Ln^{II} ions revealed that ligand-field strength, the strength of the metal-ligand interactions, and the size match between metal ions and cryptand cavities are important parameters in selecting ligands for these metal ions. Furthermore, optimization of these parameters could result in increased metal-ligand orbital interactions leading to dramatic changes in physicochemical properties of Ln^{II}-containing cryptates that are potentially useful in luminescence, redox, and synthetic applications.

AUTOBIOGRAPHICAL STATEMENT

AKHILA N.W. KUDA-WEDAGEDARA

Education

2010–2015 Ph.D., Inorganic Chemistry, Wayne State University, Detroit, MI
Dissertation Title: Ln^{II}-Containing Cryptates: Synthesis and Properties
Advisor: Dr. Matthew J. Allen

2003–2007 Grad. Chem. (First Class Hons.), Chemistry, Institute of Chemistry, Colombo, Sri Lanka

Research Skills

Air- and moisture-free (Schlenk line) synthetic techniques; Multi-step organic and inorganic syntheses; Chromatography; NMR, EPR, Fluorescence, UV–Vis and IR spectroscopies; Electrochemistry; LC-MS; ICP-MS; Handling and maintaining analytical instrumentation and glove boxes

Research and Teaching Experience

2014–2015 Graduate Research Assistant, Wayne State University, Detroit, MI
2010–2014 Graduate Teaching Assistant, Wayne State University, Detroit, MI
2008–2009 Teaching Assistant, Department of Chemistry, Open University, Colombo, Sri Lanka

Publications

Kuda-Wedagedara, A. N. W.; Wang, C.; Philip, M. D.; Allen, M. J. Aqueous Eu^{II}-containing complex that displays yellow luminescence. *J. Am. Chem. Soc.* **2015,** *137*, 4960–4963.

Kuda-Wedagedara, A. N. W.; Allen, M. J. Enhancing Magnetic Resonance Imaging with Contrast Agents for Ultra-High Field Strengths. *Analyst* **2014**, *139*, 4401–4410.

Garcia, J.; **Kuda-Wedagedara, A. N. W.**; Allen, M. J. Physical Properties of Eu (II)-Containing Cryptates as Contrast Agents for Ultra-High Field Magnetic Resonance Imaging. *Eur. J. Inorg. Chem.* **2012,** *2012*, 2135–2140.

Kuda-Wedagedara, A. N. W.; Kim, D.; Bailey, M.; Martin, P. D.; Keith, J.; Allen, M. J. Influence of Ligand Structure on the Physicochemical Properties of Yb^{II}-Containing Cryptates *in preparation*

Awards

2015 Esther and Stanley Kirschner Graduate Award for the Best Graduate Student in Inorganic Chemistry, Wayne State University

2007 Award for the Best Performance in Analytical Chemistry, Institute of Chemistry, Colombo, Sri Lanka

2007 Award for the Best Performance in Environmental Chemistry, Institute of Chemistry, Colombo, Sri Lanka

2005 Merit Award for the Top Performance in Basic Principles of Chemistry, Institute of Chemistry, Colombo, Sri Lanka